UiT
THE ARCTIC
UNIVERSITY
OF NORWAY

Faculty of Science & Technology.

Department of Geology.

Faulting and the relationship to fluid migration and shallow gas accumulation in the Hammerfest Basin, SW Barents Sea

—

Anders Edvardsen

Master thesis in Geology, GEO-3900
May 2015

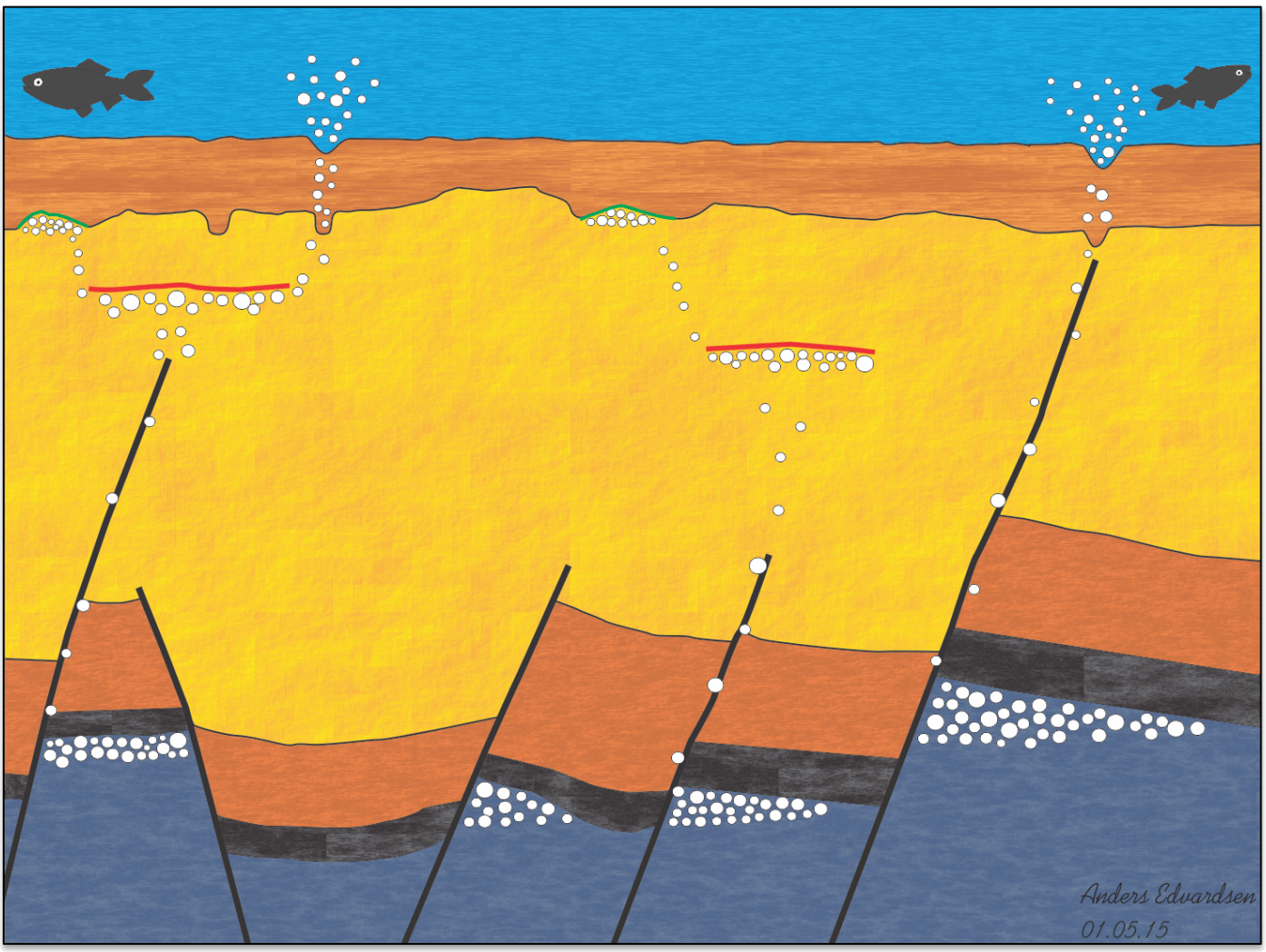

UNIVERSITY OF TROMSØ

Abstract

This thesis has focused its efforts to identify and map faults and their relationships to shallow gas accumulations and fluid flow features. The area of this investigation lies in the hydrocarbon-prone Hammerfest Basin in the southwestern Barents Sea, above the Base Cretaceous. Nine 3D seismic datasets were used in this study, aiming to improve the knowledge of the timing of the tectonic activity and the relations and the controlling mechanisms for fluid migration and accumulation.

Based on their vertical extent two fault groups exists: deep-seated and shallow faults. Deep-seated tectonic faults are further subdivided into three groups, F1, F2 and F3, based on the formation they terminate in. F1 terminates at the URU, F2 within the Torsk Formation and F3 in Cretaceous strata. Initiation of these faults occurred in the Kimmerian tectonic phase in Middle – Late Jurassic, where the E – W and NE – SW striking F2 and F3 faults experienced a small reactivation in the Barremian and Aptian. Multiple reactivations of the N – S striking F2 faults through the Cretaceous period occurred in response to thermal subsidence of the Tromsø Basin. Tectonic readjustments related to the opening of the Norwegian-Greenland Sea reactivated F2 faults and initiated the shallow faults. Faulting of the URU suggests tectonic adjustments after the onset of the Plio-Pleistocene glaciations.

Fluid migration of thermogenic gas from deeper reservoirs is evidenced by seven gas chimneys located above deep-seated faults that represents excellent migration pathways for gas from deeper levels. High amplitude anomalies within the Torsk Formation most likely represents accumulations of free gas below a sealing layer of gas hydrates. The URU occasionally acts as an impermeable barrier and amplitude anomalies located along the unconformity probably represent free gas accumulations.

Pockmarks on the seabed and the URU indicate at least two major events of fluid flow release, where variations in the stability conditions of the GHSZ have allowed free gas to burst upwards and create circular to sub-circular depressions. Pockmark formation could be an ongoing process if the hydrate layer is currently decomposing.

Acknowledgement

5 år er fullført og studietiden utgår.
Heldigvis ingen skippertak gjenstår.
Lange dager og mye slit,
med gode vennskap jeg kom meg hit.

Studiene har gitt en erfaring brei,
mange skal takkes på den lange vei.
Venner og kolleger har gitt store gleder,
da kan jeg starte med hovedveileder.

Professor Jürgen takkes med glede,
en takk for at du var til stede.
Du rettet stil og viste vei,
uten deg, stakkar meg!

Stefan Buenz, takk for hjelp og støtte,
veiledning jeg fikk i både spann og bøtte.
Petrel og seismikk det er det du kan,
lærte meg alt om geologi under vann.

Ingrid, Kristin, Mamma og Pappa,
prat med dere fikk meg avslappa!
Med fylling av kjøleskap dere bidro godt,
helgeturer hjem, det var flott!

En stor takk til kjære Elise,
på kontoret jeg kunne sjokolade spise.
Dine morsomme stunt og sprell du gjør,
glede og lykke rundt deg du strør!

Underholdning har jeg på kontoret fått.
Espen fikk faktisk ex.phil bestått!!
Andre og Adrian, kaffe og punsj,
hjelpen kommer rett etter lunsj ;-)

Kristian, Eivind, Tore og resten,
Gleder meg til reunionsfesten!
Godt humør og lystige lag,
med dere jeg følte velbehag!

Bendik, Andreas og resten av gjengen
Frank skal overta dobbeltsengen!
Latter, humor, måloppnåelse,
hva med fagforståelse?

Etter mye skriving min hjerne er mørnet,
heldigvis, ferien er rett rundt hjørnet!
Harstad og jobb det blir det neste,
men Tromsø skal jeg uansett gjeste!

Anders Edvardsen

01.05.2015

Content

1 Introduction

1.1 Objectives

The objectives of this master thesis are to identify and map faults and their relationships to shallow gas accumulations and fluid flow features, above the Base Cretaceous, within the Hammerfest Basin in the southwestern Barents Sea (Fig. 1.1). The aim is to improve the knowledge of the timing of tectonic activity and the relations and the controlling mechanisms for fluid migration and accumulation. Previous studies in the southwestern Barents Sea (e.g. Andreassen et al., 2007a; Chand et al., 2012; Ostanin et al., 2013; Rajan et al., 2013; Vadakkepuliyambatta et al., 2013) has suggested that fluid flow is abundant and widespread and often related to faults and fault structures in the subsurface connecting deep with shallow reservoirs. This study will be carried out using nine 3D seismic surveys located inside and along the margins of the Hammerfest Basin where interpretations also concentrate on the distribution of the upper regional unconformity (URU) and deeper stratigraphic horizons. A selection of seismic attributes will be used to map and visualize the vertical and lateral distribution of fault structures and fluid flow features.

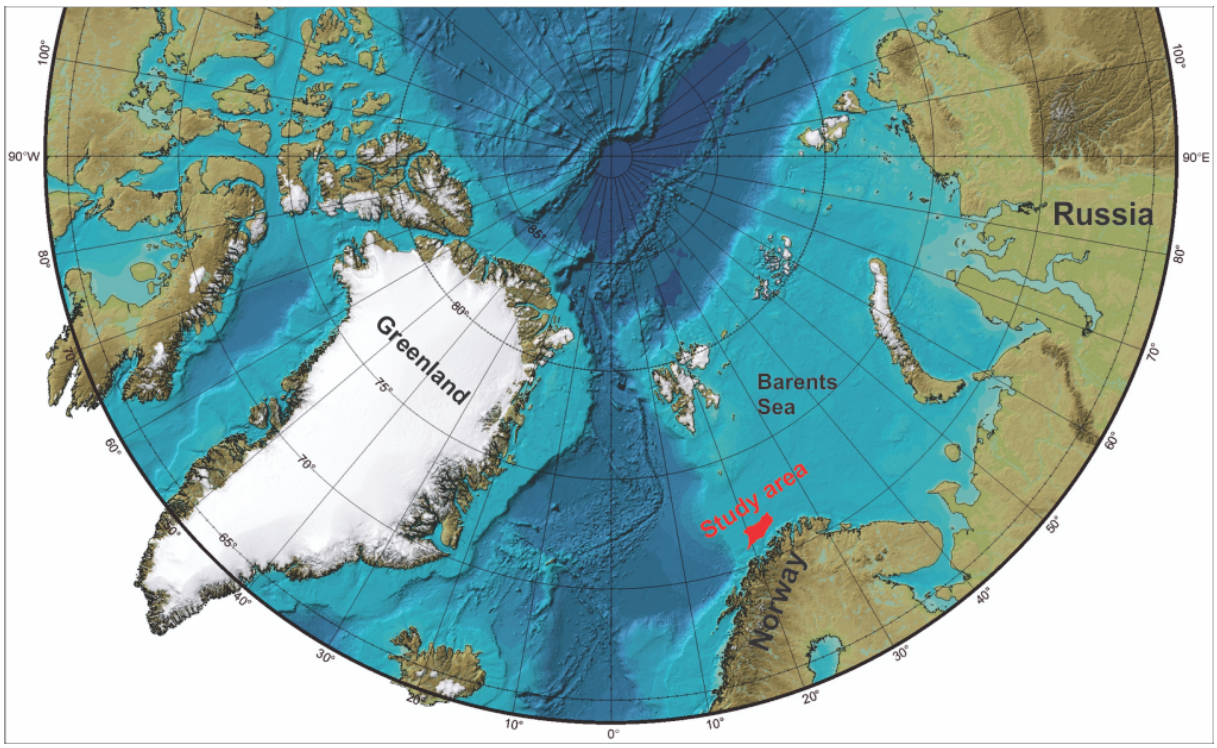

Fig. 1.1: Bathymetry map of the Arctic seabed and the surroundings. The location of the study area, the Hammerfest Basin in the southwestern Barents Sea, is indicated in red. Figure modified from Jakobsson et al. (2012).

1.2 Introduction to faults

Faults and fractures are structures formed by compressional and tensional forces in the Earth's crust, and are known to act as prominent migration pathways for fluids that allow them to flow from deep sources to shallower stratigraphic traps (Fossen and Gabrielsen, 2005; Ligtenberg, 2005).

1.2.1 Fault initiation and reactivation

Fracturing and faulting of rocks take place when the effective stress overcomes the strength of the rock. The Mohr stress diagram is useful to display the stresses acting on a plane of a given orientation where values of normal stress (σ_n) and shear stress (σ_s) components are plotted on the horizontal and vertical axis respectively (Fig. 1.2) (Twiss and Moores, 2007). A Mohr circle is defined by plotting the maximum (σ_1) and minimum (σ_3) principal stresses along the horizontal axis, where the centre of the circle is drawn in $(\sigma_1 - \sigma_3)/2$), and visualizes the stress field along a plane of interest in two dimensions. The diameter of the circle ($\sigma_1 - \sigma_3$) is called the differential stress, the difference between maximum and minimum principal stresses, and is decisive whether the rock fractures or not (Fossen and Gabrielsen, 2005).

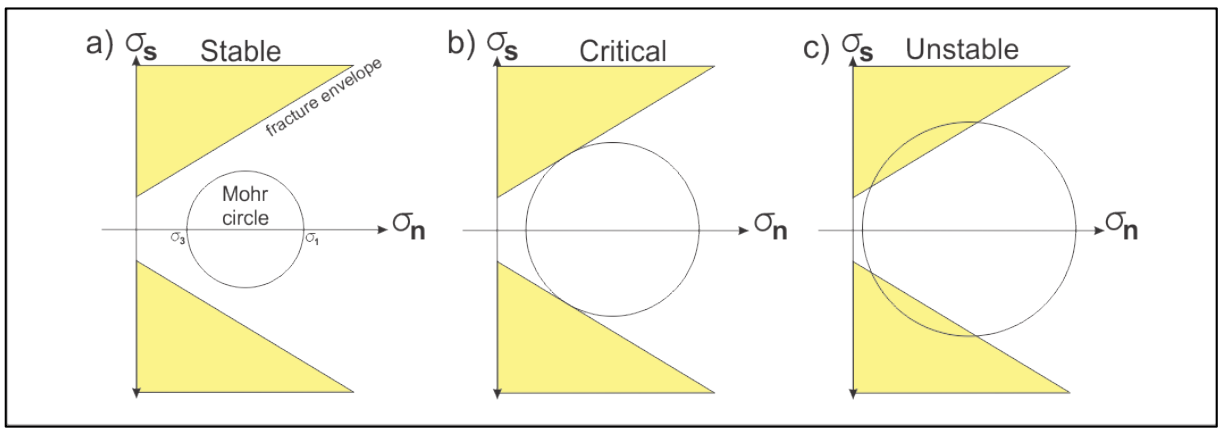

*Fig. 1.2: Failure envelope and Mohr circle in Mohr stress diagram. Showing **a)** stable, **b)** critical and **c)** unstable states of stress. Figure is modified from Fossen and Gabrielsen (2005).*

A failure envelope separates stable from unstable states of stress. When a Mohr circle crosses the envelope and represent an unstable state of stress, the rock cannot withstand the stresses and failure is initiated (Fig. 1.2c) (Twiss and Moores, 2007). For porous rocks the fracture envelope is based on the Coulombs fracture criterion that is given in Equation 1.1 and is used for brittle failure (Fossen and Gabrielsen, 2005).

$$\sigma_s = C + (tan\phi) * \sigma_n \quad \text{(Equation 1.1)}$$

The cohesion (C) is the resistance to shear fracture on a plane experiencing no normal stress and is the point where the fracture envelope crosses the σ_s – axis, and ϕ is the angle of internal friction which is the slope angle of the same envelope (Twiss and Moores, 2007). An increase in pore pressure could initiate failure in a rock that normally would be stable, as the reduction in effective stress will shift the Mohr circle to the left along the σ_n – axis by the same amount as the pore pressure without reducing the diameter of the circle (Fossen and Gabrielsen, 2005; Twiss and Moores, 2007), and drive the circle into the fracture envelope (Davis et al., 2011).

Reactivation of faults often occur as it requires much less energy than initiating new ones (Fossen and Gabrielsen, 2005). Once a fracture has developed the fracture plane, holding no cohesion, act as a zone of weakness, hence new stress will be accommodated by frictional sliding on the already existing fracture plane (Fig. 1.3) (Twiss and Moores, 2007). Reactivation of a fault would require lower differential stress than initiation of a new one would (Fossen and Gabrielsen, 2005).

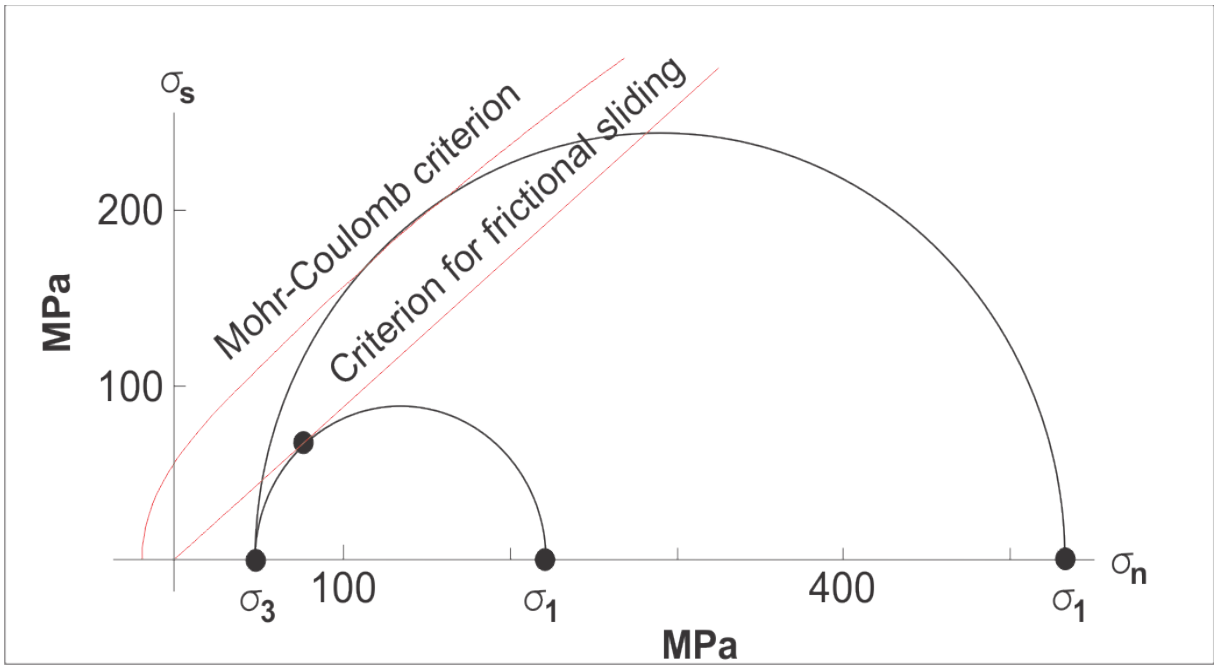

Fig. 1.3: Mohr stress diagram showing that stress will be accommodated by sliding on already existing fracture planes rather than initiation of new fractures. Figure modified from Fossen and Gabrielsen (2005).

1.2.2 Types of faults

A fault is a surface or narrow zone in the Earth`s crust where one side has moved relative to the other, parallel to the surface or zone. The fault can be vertical, horizontal or inclined, and is classified into high-angle fault or low-angle fault whether the dip of the fault is more or less than 45°. Based on the slip, which is the net distance and direction that the hanging wall has moved relative to the footwall, faults are divided into three categories, dip-slip, strike-slip and oblique slip (Fig. 1.4). The relative movement, or shear sense, along faults further subdivide them into normal, reverse and strike-slip (Fig. 1.4) (Twiss and Moores, 2007).

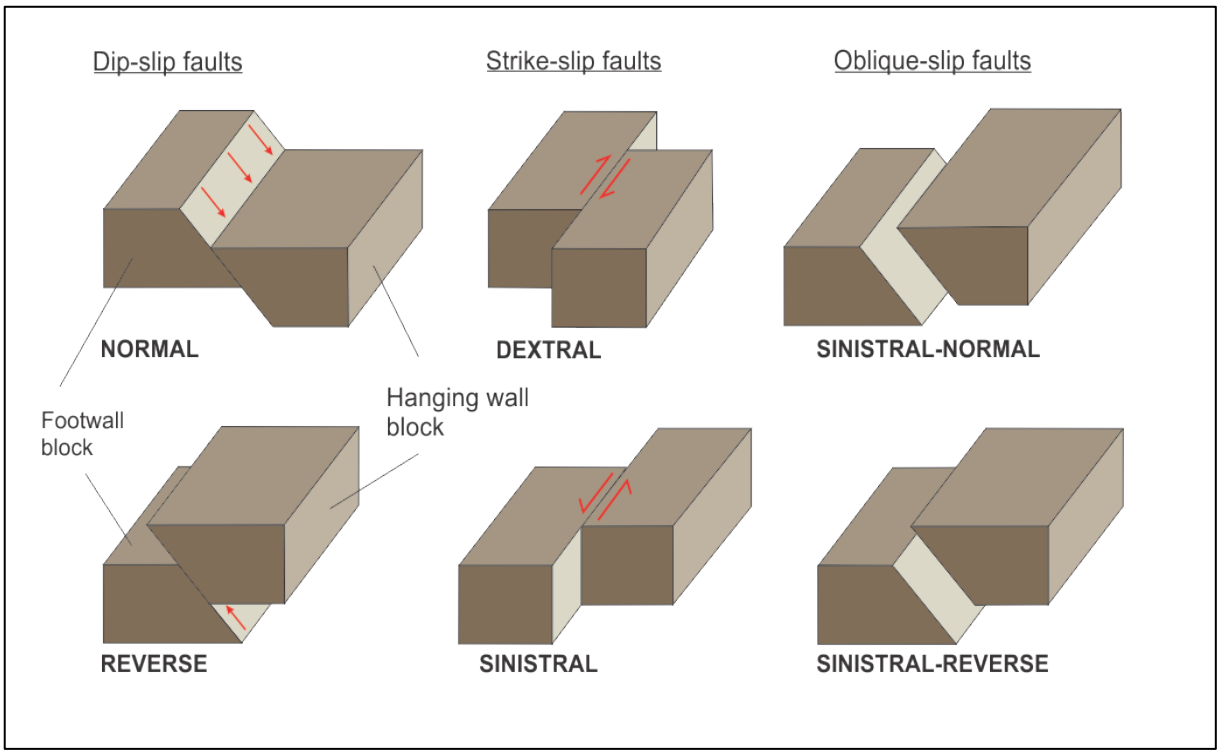

Fig. 1.4: Overview of the different classes (dip-slip, strike-slip and oblique-slip) of faults, showing the characteristic displacement for each of the classes. Figure is modified from Twiss and Moores (2007).

Normal faults are dip-slip faults that form in an extensional tectonic regime when the hanging wall moves down relative to the footwall to accommodate the lengthening of the lithospheric crust. The displacement is usually parallel to the dip of the fault surface, but may deviate if the strike of the fault changes. Normal faults usually have dips of about 60°, but can also be virtually vertical or horizontal (Twiss and Moores, 2007; DiPietro, 2013).

Normal faults commonly occur in systems of many associated faults. Faults are termed synthetic if the small-scale faults are parallel to the main faults and have same sense of shear. Antithetic faults are in the conjugate orientation with the main faults (Fig. 1.5) (Twiss and Moores, 2007). Horst-and-graben structures are characterized with alternating uplifted (horst) and down-dropped (graben) fault blocks (Fig. 1.5). While grabens are bounded by two conjugate faults dipping toward the down-dropped block, half-grabens are only bounded at one side by a normal fault. Horst is the uplifted fault block and is bounded by two conjugate normal faults dipping away from the block. The formation of horst-and-graben structures provides good accommodation space for sediments to accumulate, and by studying the faults and deposits the periods of rifting can easily be deduced (Twiss and Moores, 2007).

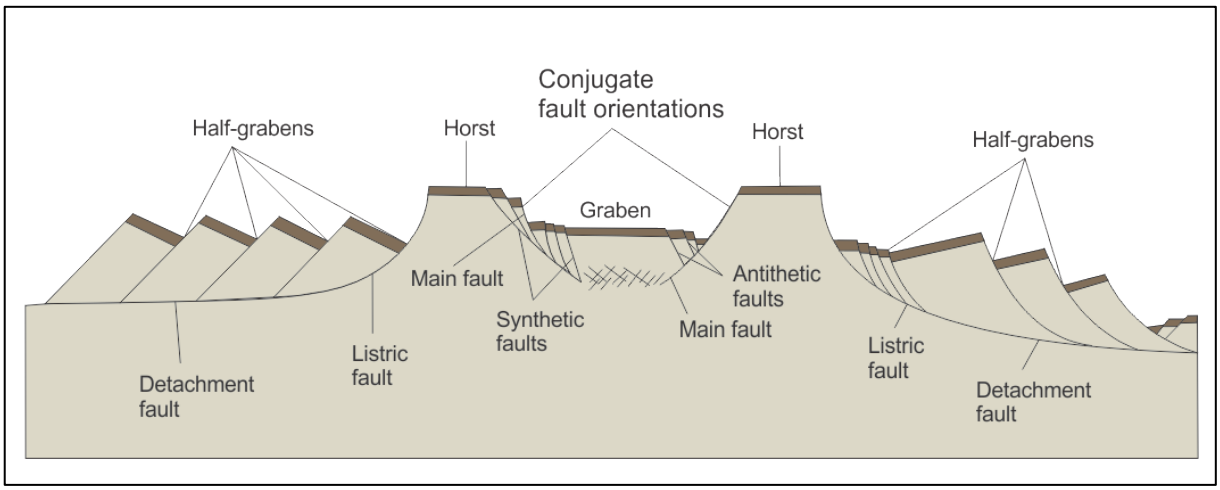

Fig. 1.5: Overview of normal faults showing that main faults occur with associated subsidiary faults. Figure from Twiss and Moores (2007).

Many faults are steep at the surface and flatten with depth. Such faults are termed listric normal faults (Fig. 1.5) and can turn into or merge with a horizontal fault, or detachment, at depth (Twiss and Moores, 2007; DiPietro, 2013). Fault blocks bounded by listric faults tend to tilt backwards as they slide down the fault surface with associated deformation in the hanging wall (DiPietro, 2013).

Reverse and thrust faults are the opposite of normal faults, but still dip-slip, and occur in areas of compression. The hanging wall is moved up relative to the footwall where older rocks are emplaced on top of younger rocks. The dip of the faults are greater than 45° for reverse faults and lower than 45° for thrust faults (Fossen and Gabrielsen, 2005; Twiss and Moores, 2007; DiPietro, 2013). Thrust faults develop a characteristic ramp-flat geometry where the fault surface cuts through the stratigraphy and the dip

alternates between sub-horizontal and 45° (Fig. 1.6) (DiPietro, 2013). The flats usually develops in low-competence layers, while the ramps in competent layers (Twiss and Moores, 2007).

If a compressional tectonic regime takes place along an old rifted continental margin, the original normal faults are likely to be reactivated as reverse faults as the strain is realized along pre-existing zones of weakness (Twiss and Moores, 2007; Kearey et al., 2009).

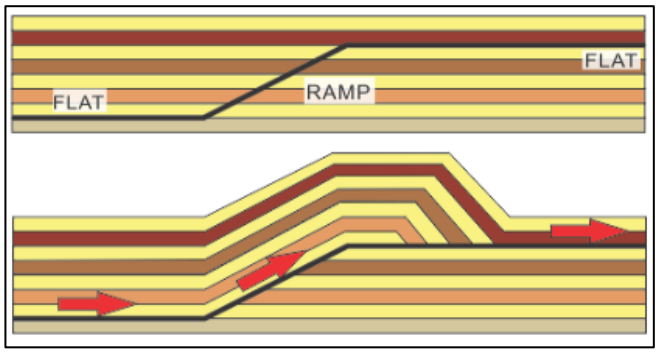

Fig. 1.6: Thrust fault where the hanging wall has moved up relative to the footwall. Development of the characteristic ramp-flat geometry. Figure modified from Fossen and Gabrielsen (2005).

Strike-slip faults have a complex architecture and consist of numerous segments of various length (Aydin and Berryman, 2010). The faults are vertical and are termed right-lateral (dextral) or left-lateral (sinistral) based on the relative movement of the fault blocks (Fig. 1.4) (Twiss and Moores, 2007).

The segmentation of strike-slip faults results in the formation of bends and step-overs where one segment terminates in proximity to another sub-parallel segment. Motion is transferred across the intervening gap and leads to zones of contraction and extension, producing restraining and releasing bends and step-overs (Fig. 1.7) (Twiss and Moores, 2007). Strike-slip motion combined with extension and contraction is known as transtension and transpression respectively (Kearey et al., 2009). Movement along faults with bends and step-overs commonly results in the formation of strike-slip duplexes. Strike-slip duplexes are lens-shaped zones of horizontally stacked horses between segments of the main fault (Fig. 1.8) (Twiss and Moores, 2007; Kearey et al., 2009).

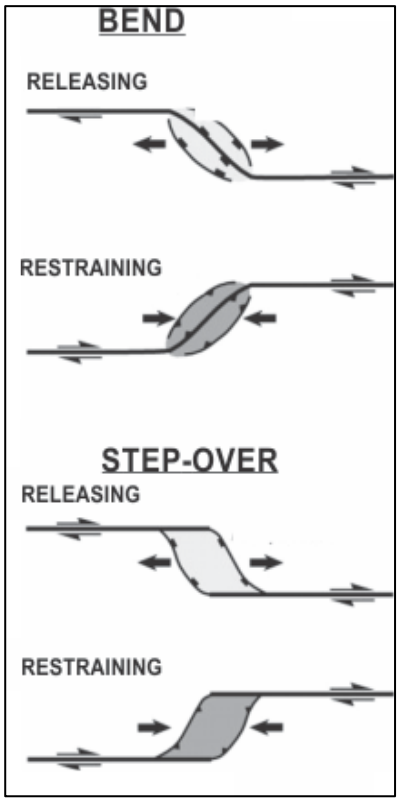

Fig. 1.7: Map view of releasing and restraining bends and step-overs. Figure modified from Kearey et al. (2009).

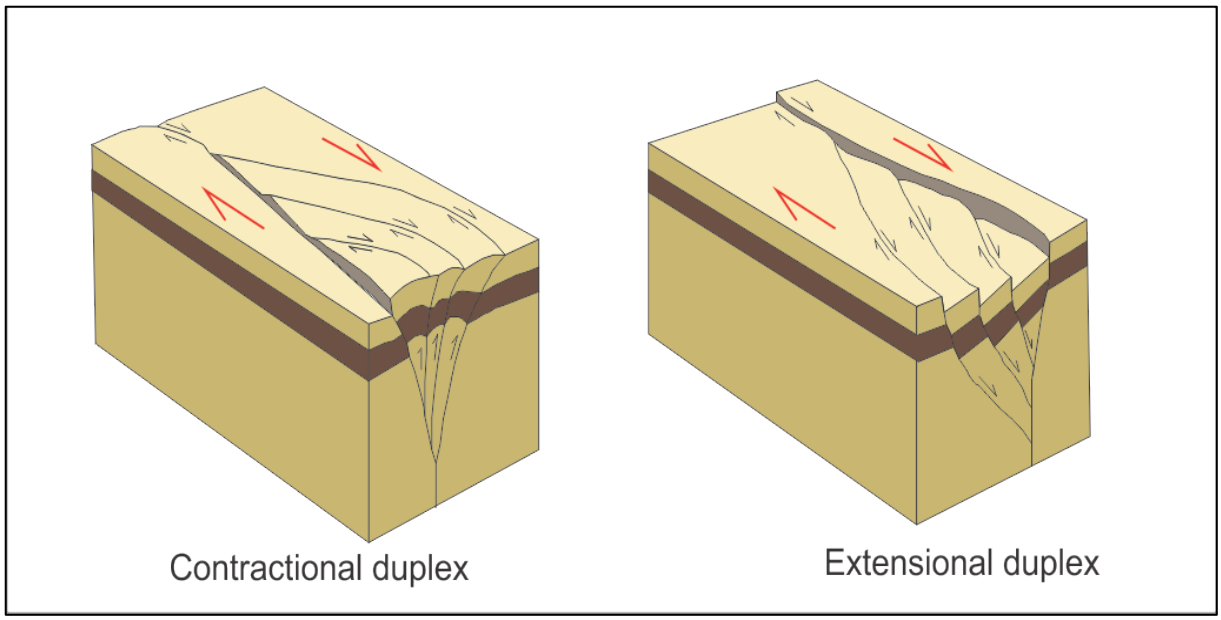

Fig. 1.8: Formation of contractional and extensional duplexes developed from restraining and releasing bends on a dextral strike-slip fault. Figure is modified from Twiss and Moores (2007).

1.3 Dynamics of fluid migration

Fluids exist within pore spaces and fractures in sediments and rocks, and generally occur in gaseous and/or liquid phases (Guzzetta and Cinquegrana, 1987). Fluid migration is the movement of these fluids through rocks holding sufficient porosity and permeability, and is a natural, although complex, process that is driven by pressure and temperature gradients in the subsurface (Selley, 1997; Berndt, 2005).

Darcy`s law (Equation 1.2) expresses that the flow of fluids through a permeable medium occur in response to a hydraulic potential field, where the amount of fluids flowing is determined by the rock properties and the difference in pore-water pressure on both sides of the flow (Bjørlykke, 1993; Berndt, 2005). The equation, only valid when the medium is filled with only one fluid phase and no chemical reaction occur between the fluid and the medium (Selley, 1997), states that fluid flow favours a short migration pathway with high permeability and high pressure difference, and that a fluid of low viscosity flows better than one of high viscosity. Darcy`s law are not valid if the fractures are too big compared to the area of interest (Fisher et al., 2003; Berndt, 2005).

$$Q = \frac{k\,(P_1 - P_2)\,A}{\mu\,L} \qquad \text{(Equation 1.2)}$$

Q = Fluid flux (m^3/s) *K = Permeability (m^2)* *A = Area (m^2)*

*μ = Viscosity of the fluid (Pa*s)* *L = Migration length (m)*

$\nabla P = P_1 - P_2$ = Pressure difference (Pa)

Sediments on continental margins loses porosity and permeability due to compactional processes when they get buried deeper and are subjected to increasing load of the overburden (Guzzetta and Cinquegrana, 1987; Berndt, 2005). Compaction highly depends on lithology and diagenetic processes, where the pore pressure will equal the hydrostatic pressure if the fluids are allowed to dissipate during the compaction (Berndt, 2005). Hydrostatic pressure (Equation 1.3) is the pressure imposed by a continuous column of fluid at rest, and fluid pressures exceeding that of the hydrostatic at a specific depth are commonly termed overpressures (Osborne and Swarbrick, 1997; Selley, 1997).

$$P = pgh + P_a \qquad \text{(Equation 1.3)}$$

P = pore pressure (Bar) *g = gravitational constant (9.81 m/s^2)*

h = height of fluid column (m) *p = density of pore water (kg/m^3)*

P_a = atmospheric pressure (1 Bar)

Overpressures can be generated by several mechanisms (Osborne and Swarbrick, 1997), such as differential compaction and sedimentation, or by generation of biogenic and thermogenic gas (Osborne and Swarbrick, 1997; Swarbrick et al., 2002; Berndt, 2005), where the permeability of the overlying and surrounding rocks is not sufficient to equalize the generation of fluid pressure (Berndt, 2005). High overpressure could fracture rocks (Berndt) and allow fluids to migrate both laterally and occasionally downward (e.g. Bonham, 1980; Bjørlykke, 1993), before the fluid pressure eventually becomes hydrostatic (Berndt, 2005).

1.4 Seismic indications of fluids

Seismic profiles are produced when pressure waves emitted from a source are reflected in the subsurface, and received by hydrophones in streamer arrays behind ships or geophones on the seabed. Seismic reflections originate from interfaces usually related by sedimentary bedding planes, unconformities and/or porefill in sediments. It is, however, the change in acoustic impedance across the interface that produces the reflection. The acoustic impedance is given by Equation 1.4 (Veeken and Moerkerken, 2013).

$$AI = v * \rho \qquad \text{(Equation 1.4)}$$

v = P-wave velocity (m/s)

ρ = Density (kg/m^3)

1.4.1 Appearance of fluids in reflection seismic profiles

Accumulation and traces of hydrocarbons are often recognized by high amplitude anomalies. Such anomalies can either be caused by increase or decrease in acoustic-impedance, and are commonly called hydrocarbon indicators (Brown, 2004; Andreassen et al., 2007a). Hydrocarbon indicators, as bright spots and flat spots, represent fluid contacts and more often relates to gas than oil, as the acoustic properties of oil are similar to that of water (Brown, 2004).

The presence of gas in sediments dramatically reduces the P-wave velocity, hence giving rise to a negative change in acoustic impedance. Veeken and Moerkerken (2013) argued that already five percent of gas saturation in the sediments would have a tremendous effect on P-wave velocity and give rise to a reflection with anomalously high amplitude, also called a *bright spot* (Fig. 1.9) (e.g. Andreassen et al., 2007a). In seismic the bright spots commonly occur close to leaking faults, within or on top of reservoirs, at gas pockets and along gas chimneys (Ligtenberg, 2005). It is important to bear in mind that negative changes in acoustic impedance could be also related to changes in the lithology (Badley, 1985).

The reflection at the top of a gas reservoir can change from a bright spot to an increase in acoustic impedance across the fluid contact, giving rise to a *phase reversal* (Fig. 1.9)

(Brown, 2004). A phase reversal is characterized by a phase-shift of 180° along a continuous reflection at gas-oil or gas-water contact, where the peak becomes a trough and a trough becomes a peak (Løseth et al., 2009). A local decrease in amplitude, a *dim spot* (Fig. 1.9), can occur when the acoustic impedance contrast is small, and can indicate that some gas has replaced the water in the pores (Brown, 2004; Løseth et al., 2009).

If the thickness of a gas-filled reservoir is sufficient, and there is a sufficient contrast in acoustic impedance between the gas and the underlying sediments, the reflection from the interface will produce a *flat spot* (Fig. 1.9). A flat spot is best identified by its flatness, and by its discordance with adjacent reflections (e.g. Brown, 2004; Andreassen et al., 2007a). Below a gas reservoir the reflections can exhibit a *pull down* as a result of the low velocity (increased travel time) in the gas-bearing sediments. The reflection will then appear deeper in the seismic data than it actually is (e.g. Judd and Hovland, 1992; Andreassen et al., 2007a).

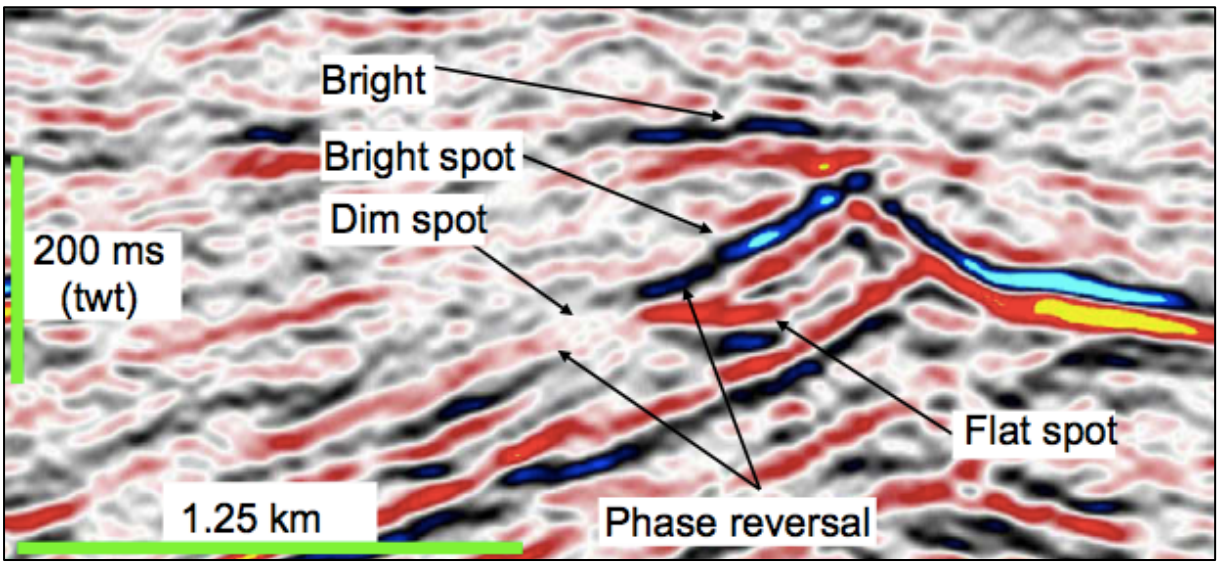

Fig. 1.9: Bright spot, dim spot, phase reversal and flat spot are all hydrocarbon indicators. Figure from Løseth et al. (2009).

1.4.2 Seismic amplitudes and shallow gas accumulations

Fluid migration pathways can be identified on seismic data, which has been successfully used to map zones of high fluid flux, to detect zones of hydrocarbon expulsion and to investigate which faults are leaking and which do not (Ligtenberg, 2005). Migration pathways are detected in the seismic as vertical zones of acoustic masking and have been described as gas chimneys (Løseth et al., 2009). Andreassen et al. (2007a) described acoustic masking as an area of the seismic profile with low seismic reflectivity or where seismic reflections are highly distorted or disturbed. Gas chimneys may represent a fractured cap rock with irregularly distributed low-velocity gas zones, and the shape of the chimney can vary from diffuse shadows to distinct vertical zones (Løseth et al., 2009).

Acoustic pipes are sub-vertical zones of acoustic masking where the continuity of reflections is disrupted over long vertical extent (Fig. 1.10). They represent migration pathways for fast flowing gas-charged fluids from underlying reservoirs (Andreassen et al., 2007a). In plan view they appear as circular to oval features measuring 20 – 200 m in diameter with up-bending, low-amplitude reflections (Berndt et al., 2003; Løseth et al., 2011; Plaza-Faverola et al., 2014). They often appear in association with bright spots, and can terminate at the seabed in large pockmark craters 100 – 500 m wide and up to 30 m deep (Andreassen et al., 2007a; Løseth et al., 2009; Plaza-Faverola et al., 2014).

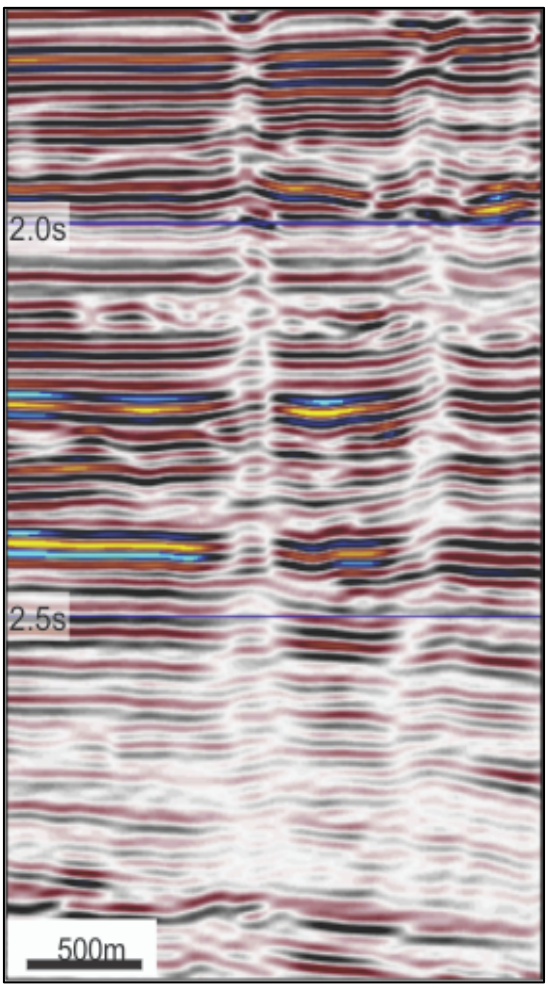

Fig. 1.10. Seismic expressions of an acoustic pipe where the continuity of the reflections is disrupted over a long vertical extent. Figure modified from Løseth et al. (2011).

1.5 Fluid migration models

Migration of fluids can occur in a variety of ways, and fluids are not uncommon to migrate more than 2 km vertically and over 100 km laterally (e.g. England et al., 1987). Petroleum migration occurs below a sealing surface and both the fracturing and the fluid potential largely controls the migration pathway, with fluids moving from high to lower fluid potential. Gradients in fluid potential are derived from variations in excess water pressure, natural buoyancy forces (gas more buoyant than oil, and oil more buoyant than water) and capillary pressure differences (England et al., 1987; Hindle, 1997).

1.5.1 Lateral fluid migration

Lateral fluid migration occur in most sedimentary basins on Earth, where the origin of the petroleum is located several hundreds of kilometres away from the petroleum reservoir (e.g. Thrasher et al., 1996). Migration along permeable carrier beds will occur if there is a sufficient sealing horizon present, and will continue along the bed until it reaches the end of the sealing surface (Hindle, 1997). Sedimentary basins that have experienced little tectonic activity favour lateral fluid migration (Thrasher et al., 1996).

1.5.2 Vertical fluid migration

Petroleum fluids will move up vertically if it can overcome the excess capillary pressure of the seals overlying the horizontal carrier beds. It will then continue within vertical migration pathways until another seal is encountered (England et al., 1987). The migration of hydrocarbons can damage primary sedimentary layering and result in permanent alteration of rocks (Løseth et al., 2009). Tectonic activity (including faulting and piercement structures), depositional rate and muddy sedimentations tend to produce vertical migration in sedimentary basins (Thrasher et al., 1996).

Cartwright et al. (2007) described geological features embedded within sealing sequences that promoted cross-strata fluid migration, and inferred the term seal bypass systems (SBS). The large-scale features are visible in seismic data and are commonly developed in petroliferous basins. Based on seismic interpretational criteria, SBS are classified into three groups: (1) fault related, (2) intrusion related and (3) pipe related (Cartwright et al., 2007).

Fault zones represent good fluid conduits, and are the main migration pathway for fluids in sedimentary basins worldwide (Ligtenberg, 2005; Løseth et al., 2009). Leakage can occur along both small- and large-scale faults, with the small faults having the same leaking potential as larger faults (Cartwright et al., 2007; Plaza-Faverola et al., 2014). Ligtenberg (2005) argued that fluid flow occurred along local, weak sections within a fault zone, and not across the whole fault zone. The complexity and intersections of fault zones, in combination with the shape and roughness of individual fault planes, are all factors controlling the nature of fluid flow (Ligtenberg, 2005). Faults do not have to be leaking or sealing all the time as episodes of flushing can occur. Fault gouge along fault planes will affect the permeability and the connectivity of fractures and pores, and the faults could then be sealing or leaking when the fluid pressure increases above a threshold value (Ligtenberg, 2005; Cartwright et al., 2007; Løseth et al., 2009).

Polygonal fault systems are non-tectonic, non-gravitational faults confined to a stratigraphic layer, and are formed by compaction and dewatering of fine-grained sediments (Berndt et al., 2003; 2005; Ostanin et al., 2012). Polygonal faults can be mapped in 2D and 3D seismic data and occur in sedimentary basins all over the world. The fault systems have also supplied fluids into hydrate stability zones and produced pathways for structures as sand injections (Ostanin et al., 2012).

Migration along faults could be challenging to identify and map in seismic data due to uneven distribution and limited extent of the fault zone. However, the hydrocarbons may migrate into permeable strata on the sides of the fault zone and give rise to hydrocarbon indicators as bright spots (Løseth et al., 2009). If leaking faults extends up to or close to the seabed they could give rise to carbonate build-ups (REF), asphalt volcanoes (Macdonald et al., 2004), gas plumes in the water column (Hustoft et al., 2007; Smith et al., 2014), or lines of pockmarks (e.g. Cartwright et al., 2007; Hustoft et al., 2007; Løseth et al., 2009).

Intrusions are structures that breach a sealing sequence and assist fluids to flow migrate through it. There are four groups of intrusions: sandstone intrusions, igneous intrusions along with salt and mud diapirs. Intrusions through impermeable sequences can transmit fluids through the sequence along with the intrusive material, or they can

create fractures and deform the strata that fluids could exploit to migrate. The intrusions themselves could also be highly permeable due to high permeability material (sandstone intrusions) or fractures (igneous intrusions) (Cartwright et al., 2007).

Pipes and chimneys were mentioned and described in chapter 1.4.2, and are the least documented of the SBS groups. They can be defined and mapped in in 3D seismic data as sub-vertically narrow zones, formed by the gas that generated hydro fractures from the reservoir to the seabed (Cartwright et al., 2007; Løseth et al., 2011). Pipes can originate at different depths, like the base of a gas hydrate layer or top of polygonal fault systems, and penetrate hundreds of meters of sedimentary strata (Berndt et al., 2003; Ostanin et al., 2012). Active pipes can be identified with down-bending reflections produced by the low seismic velocity of gas-bearing sediments (Berndt et al., 2003).

1.5.3 Seabed expressions of fluid flow release

Pockmarks are concave depressions in the seabed representing the area where fluid or gas discharge from the subsurface via the seabed into the water column (Fig. 1.11) (Hovland et al., 2002). They are often located in areas where gas is present in near-surface sediments and above zones of deteriorated seismic data (pipes and gas chimneys) indicating fluid flow. They can occur in both active and passive continental margins (Hovland et al., 2002; Judd and Hovland, 2007; Løseth et al., 2009; Cathles et al., 2010). Pockmarks can also be found in buried surfaces, called paleo pockmarks. They indicate that fluid flow have ceased and the pockmark have been filled by sediments (Judd and Hovland, 2007).

The size and shape of pockmarks can vary distinctly between areas and within an individual site location. They may be circular or elliptical, where slope angle and tidal currents influence the long and short axes. Individual pockmarks may merge into each other (composite) or occur in large strings that extend for several hundreds of metres, often linked with faults and leaking structures in the subsurface (Hovland et al., 2002; Judd and Hovland, 2007; Løseth et al., 2009).

Pockmarks have a diameter of typically tens of metres, but can vary from only a few metres to several hundreds of metres (Løseth et al., 2009), while the depth differ from 1

to 45 metres (Hovland et al., 2002). The density and distribution are related to the surficial sediment type and thickness, where many but small pockmarks form in silts, and few but large pockmarks form in the clays (Judd and Hovland, 2007). Hydrocarbon leakage is frequently associated with unusual biological activity and precipitation of carbonate (Judd and Hovland, 2007; Løseth et al., 2009).

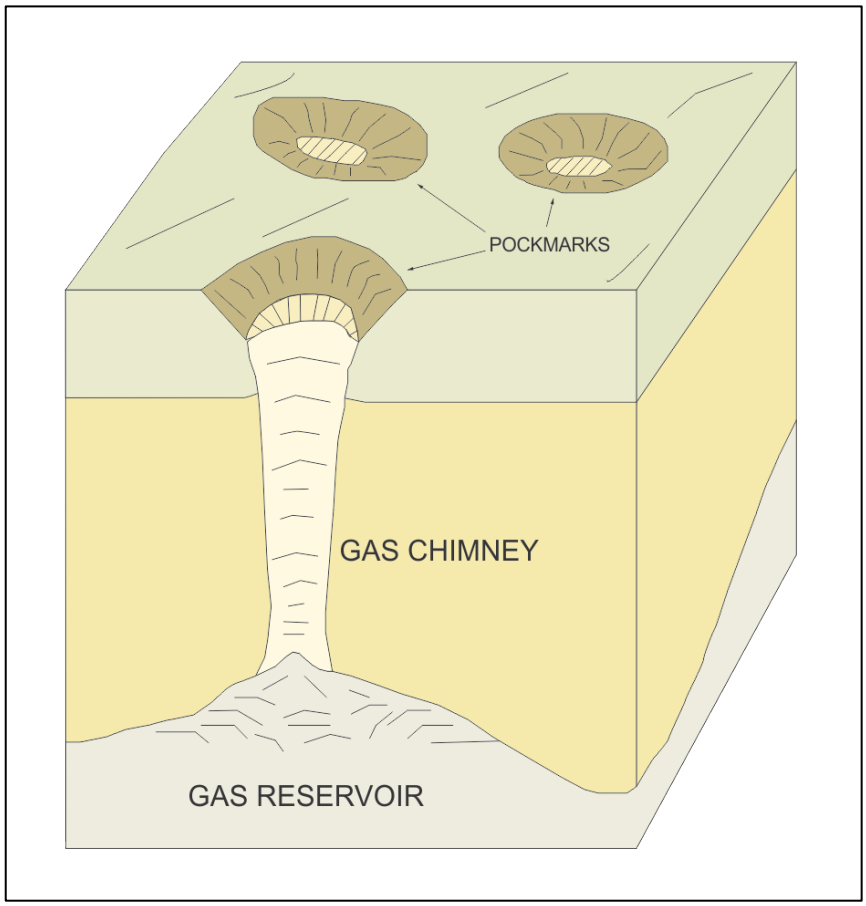

Fig. 1.11: Pockmark depressions are often located on top of gas chimneys, where gas discharge from the subsurface into the water column. Figure modified from Cathles et al. (2010).

2 Study area

2.1 Introduction

The Barents Sea, a part of the enormous shallow water shelf regions of the Arctic Ocean, is located off the northern coasts of Norway and Russia (Fig. 2.1). It is bordered in the east by the Novaya Zemlya, Franz Josef Land and the Svalbard archipelago in the north, and the eastern passive margin of the deep Atlantic Ocean in the west. In total the Barents Sea covers an area of 1,3 million km^2 with water depths averaging at approximately 300 m (Dorè, 1995; Smelror et al., 2009).

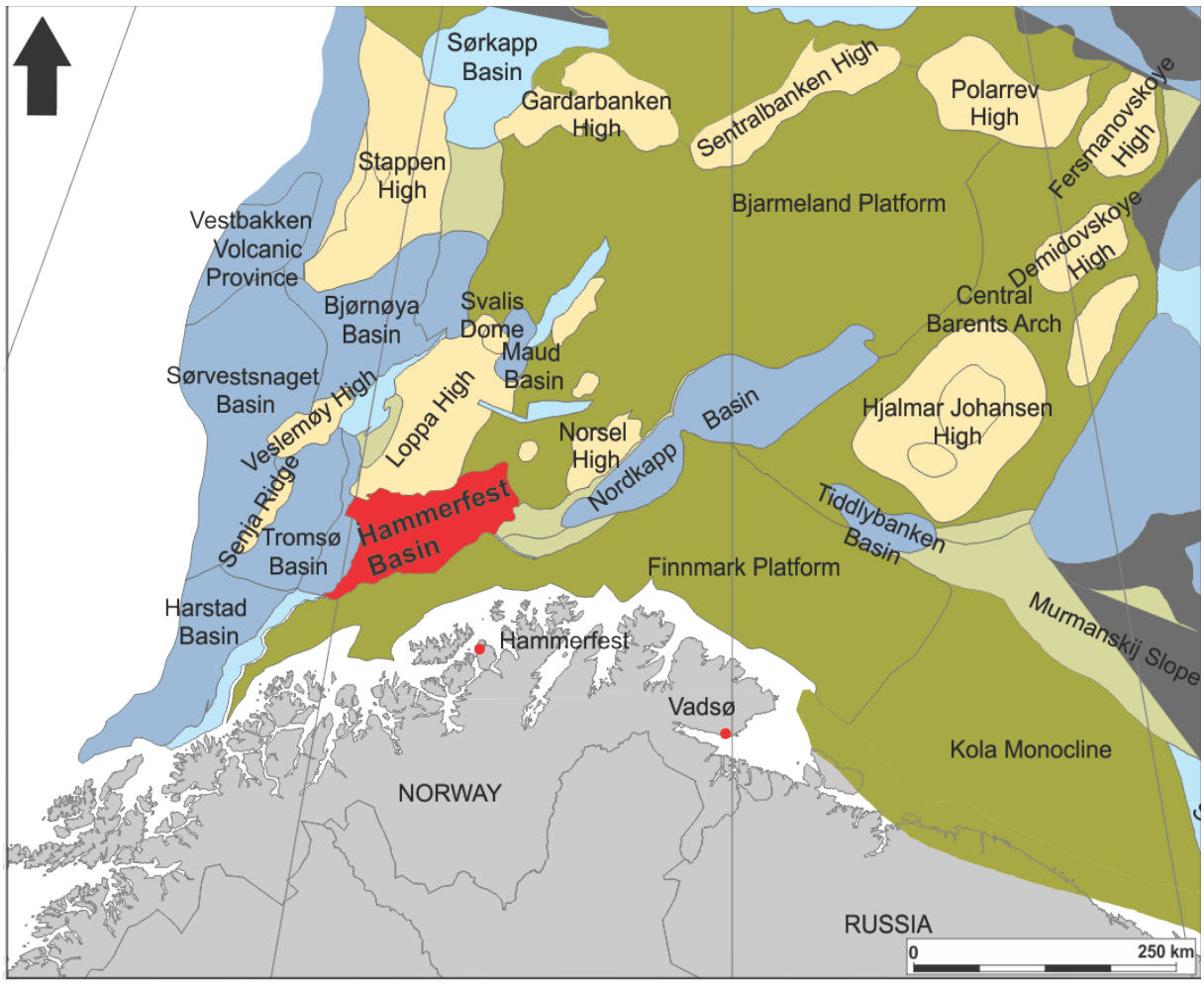

Fig. 2.1: Overview of the western and central Barents Sea in relation to the coast of the northern Norway, showing the main structural elements in the region. The study area (Hammerfest Basin) is colored red. Figure is modified from Henriksen et al. (2011a).

The Barents Sea region is the part of the Norwegian offshore territory that is least explored. After numerous geological surveys and hydrocarbon exploration on Svalbard land formations, the companies turned to the Barents Sea. In 1969 seismic acquisition started and the confirmation of sedimentary strata and delineation of the major sedimentary basins were soon made. The first well was drilled in 1980 and the following year the Askeladden and Alke discoveries were made (Dorè, 1995).

The mosaic of basins and platforms in the Barents Sea reflect the complex tectonic development of the northwestern corner of the Eurasian plate (Fig. 2.1). The Barents Sea comprises two geological disparate provinces separated by a north – south oriented monoclinal structure in the centre (Worsley, 2008). While the geology of the eastern province mainly has been influenced by the tectonic development of the Novaya Zemlya, Timan-Pechora Basin and the Uralian orogeny, the western province is a result of the post-Caledonian rifting and later rifting episodes (Smelror et al., 2009). The evolution of the Barents Shelf has been influenced by several tectonic events from Devonian to Paleocene – Eocene times (Duran et al., 2013a).

2.2 Geological history of the Barents Sea

Since the southwestern Barents Sea is the focus of this thesis the evolution of the eastern province will only briefly be summarized here.

2.2.1 Paleozoic

Two major continental collisions subsequently sundered by continental separation laid the foundation for the present geology of the Barents Sea (Dorè, 1995). The first event of collision, the Caledonian orogeny, culminated approximately 400 Ma when compressional tectonics led to closure of the Iapetus Ocean, a major seaway similar to the present northeast Atlantic (Dorè, 1995). The orogeny, which represented the consolidation of the Laurentian and Baltic plates into the Laurasian continent, influenced later the tectonic development of the western Barents Sea.

An extensional tectonic regime commenced in Late Devonian as rifting initiated the formation of sedimentary basins with N – S and NE – SW oriented structural trends inherited from the Caledonian orogeny. The Caledonian orogen was extensively eroded

and the southwestern Barents Sea was gradually peneplaned (Dorè, 1995; Smelror et al., 2009). Regional sag basins developed across the Barents Sea as the second event of collision, the Uralian orogeny propagated northwards and reached the eastern Barents Sea in Late Carboniferous (Smelror et al., 2009).

In the western Barents Sea extensional tectonics dominated in the Carboniferous and sedimentary systems, partly controlled by the basin formation. A strike-slip setting along the western margin resulted in horst-graben development along N – S trending lineaments. Geometries in areas further east, including the Nordkapp Basin and the Bjarmeland Platform, were controlled by NE – SW oriented lineaments (Smelror et al., 2009). A climatic shift took place in Carboniferous time as the Pangaea continent drifted northward. The climate shift towards warmer temperature combined with a regional transgression led to the formation of a carbonate platform where widespread deposition of evaporites occurred in the deepest basins, included the Tromsø and Nordkapp Basins (Faleide et al., 2008; Worsley, 2008; Smelror et al., 2009). Rifting ceased toward Late Carboniferous and led to regional subsidence in the western Barents Sea (Fig. 2.2).

Early Permian was characterized by major sea level changes driven by repeated glaciations in the southern hemisphere (Smelror et al., 2009). At the onset of Wordian time there was a change in climate and the depositional regime developed from carbonate to a siliciclastic. A major intracratonic seaway opened along the western shelf and remained open to the time of development of the early Atlantic rift system (Faleide et al., 1984; Worsley, 2008; Smelror et al., 2009).

2.2.2 Mesozoic

In early Mesozoic the Uralian collisional event had led to closure of the marine connection from the southeast to the Barents Sea. The western part of the Barents Sea experienced a tectonically quiet period with both regional subsidence and high sedimentation rate (Worsley, 2008; Smelror et al., 2009). Erosion of the Fennoscandian Shield, Novaya Zemlya and the Uralian highlands, supplied the Hammerfest and the Nordkapp basins with siliciclastic sediments. Minor tectonic activity occurred on the Bjarmeland and Finnmark platforms, and rifting west of the Loppa High resulted in uplift and erosion of the high itself. The Early Triassic rifting initiated salt-tectonic

activity in the Nordkapp Basin (Fig. 2.2) (Smelror et al., 2009). Erosion of larger areas followed in the Late Triassic – Early Jurassic when the eastern Barents Sea Shelf was uplifted. This resulted in extensive westward coastal progradation and the development of deltaic and floodplain environments over much of the province, with marine environments restricted to the westernmost areas (Worsley, 2008; Smelror et al., 2009).

The Barents Sea experienced little faulting activity in Jurassic times, i.e. before the onset of the Kimmeridgian tectonic phase in the Middle Jurassic, where extension and minor strike-slip adjustment along pre-existing tectonic lineaments caused faulting along east and northeast trends (Faleide et al., 1993). A regional transgression followed, with the deposition of anoxic black shales between tilted fault blocks and renewed subsidence of the Tromsø and Bjørnøya Basins. Doming occurred in the central Hammerfest Basin (Faleide et al., 1984; Faleide et al., 1993; Worsley, 2008).

The Early Cretaceous in the southwestern Barents Sea is associated with at least three tectonic phases related to the northward propagation of Atlantic rifting. The structuring of the margin was characterized by large-scale extension with minor sinistral transtension along the Bjørnøyrenna Fault Complex. The Hauterivian – Barremian tensional event resulted in activation of the N – S oriented Ringvassøy-Loppa Fault Complex, and also marked the end of rifting in the Hammerfest Basin (Faleide et al., 1993; Ostanin et al., 2012). The final rift phase was followed by rapid subsidence of the Harstad, Bjørnøya and Tromsø basins and infill by a 5 – 6 km thick shale sequences covering the structural relief (Faleide et al., 1993).

In the Late Cretaceous rifting and continental breakup of the North Atlantic commenced. The rifting set up a dextral stress field along the Senja Fracture Zone and Hornsund Fault Zone that during Paleogene acted as a relay zone between spreading centres (Smelror et al., 2009). Oblique slip caused the formation of pull-apart basins and subsidence in the southwestern Barents Sea (Fig. 2.2) (Faleide et al., 2008). The Tromsø and Sørvestnaget Basins continued to subside in Late Cretaceous while areas further east experienced uplift (Faleide et al., 1993; Smelror et al., 2009).

2.2.3 Cenozoic

The onset of seafloor spreading in the Greenland – Norwegian Sea took place in the transition between Palaeocene and Eocene, and developed a sheared margin on the western Barents Sea (Faleide et al., 1993). The margin is composed of two sheared segments (Senja Fracture Zone & Hornsund Fault Zone) separated by a central rift complex (Faleide et al., 2008). The Senja Fracture Zone developed first by continent – continent shear followed by continent – ocean shear, and has been passive since early Oligocene time (Faleide et al., 2008). The right stepping nature of the dextral sheared margin gave rise to the rift complex, where the releasing bend led to volcanism and basin formation in a pull-apart setting. The resulting Vestbakken Volcanic Province is located within this segment (Faleide et al., 1993; 2008). The northern initially sheared, and later rifted segment, the Hornsund Fault Zone, developed with components of transpression and transtension as Greenland slid past Svalbard in Eocene time (Faleide et al., 1996; 2008).

A change to NW – SE directed rifting in the Greenland – Norwegian Sea occurred in Early Oligocene and caused the seafloor spreading to extend northward in the Greenland Sea, separating the Barents Self from Greenland/North America (Faleide et al., 1993; Bergh et al., 2007; Smelror et al., 2009). The change in rifting also caused reactivation of faults in the Vestbakken Volcanic Province, and the transpressional setting around Svalbard were replaced with incipient seafloor spreading (Faleide et al. 2008).

In the Late Pliocene the Northern Hemisphere were subjected to repeated glaciations. As the entire Barents Shelf was uplifted and eroded several times, a regional hiatus (URU – Upper Regional Unconformity) created by erosional ice-sheet movements, separated variously dipping sedimentary rocks beneath from a sequence of glacigenic sediments above the URU (Fig. 2.2). The most extensive erosion occurred in the areas around Svalbard where 2 – 3 km of sediments were removed, while the Hammerfest Basin and Loppa High in the south, usually experienced less than 2 km of erosion (Vorren et al., 1991; Smelror et al., 2009). The large volumes of sediment transported by glaciers were deposited in fans along the western margin, where the Bjørnøya and Storfjorden fans showed an enormous up to 4 km thick sediment accumulation (Faleide et al., 2008; Smelror et al., 2009).

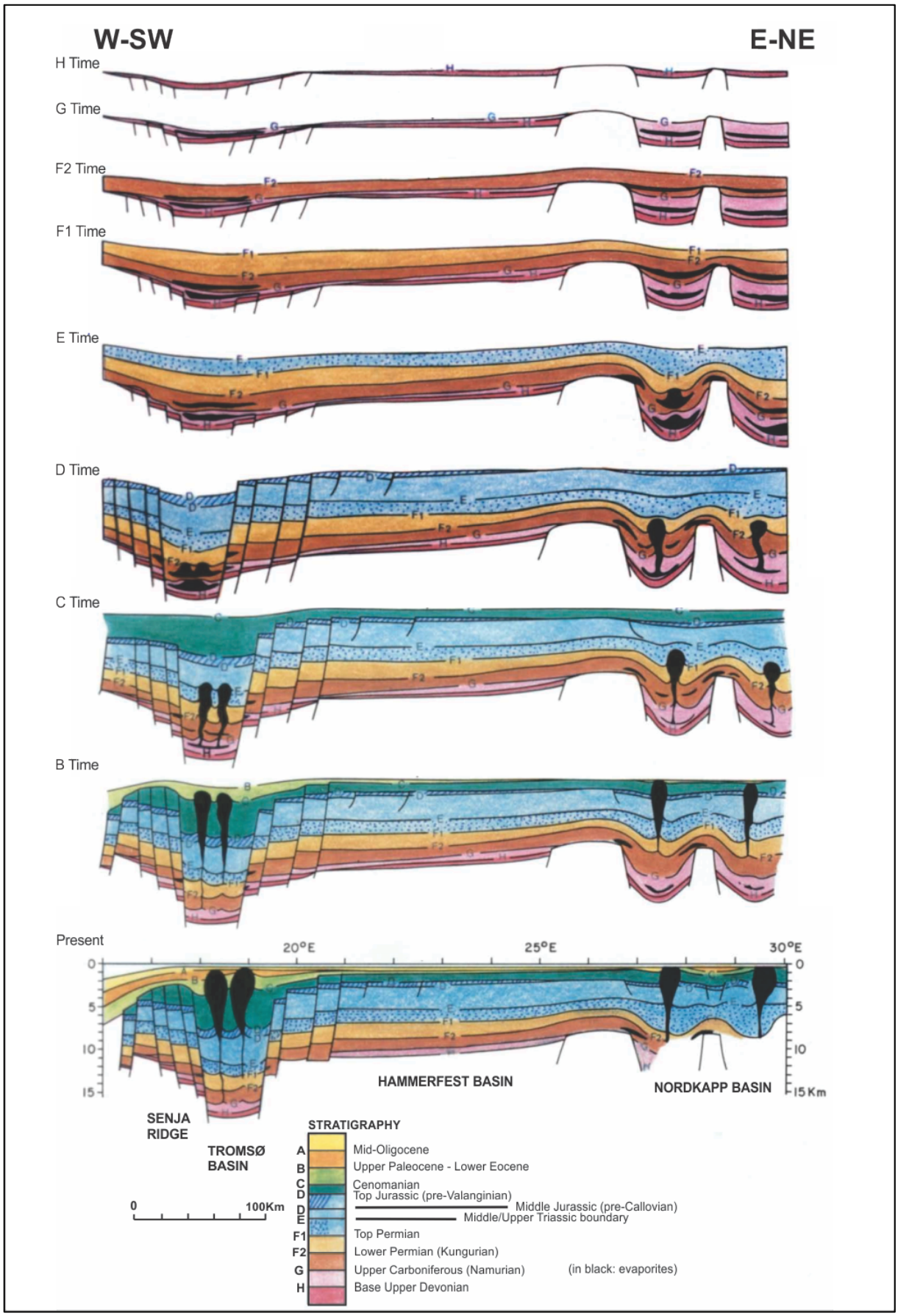

Fig. 2.2: Evolution of the southwestern Barents Sea between the Senja Ridge in the west and the Nordkapp Basin in the east, from Devonian to the present. Figure modified from Faleide et al. (1984).

2.2.4 Hammerfest Basin

The Hammerfest Basin is a relatively shallow east-northeast oriented graben-like structure, 150 km long and 70 km wide (Fig. 2.1). In the south the Troms-Finnmark Fault Complex separates the Hammerfest Basin from the Finnmark Platform, and in the north the west-east trending Asterias Fault Complex separates the basin from the Loppa High. The Asterias Fault Complex is extensional in origin and has since Jurassic times been important in the development of the Hammerfest Basin (Gabrielsen et al., 1990). To the east the structural relief dies out toward the Bjarmeland Platform, while the Ringvassøy-Loppa Fault Complex marks the transition to the deep Tromsø Basin in the west (Faleide et al., 1984; Gabrielsen et al., 1990; Gudlaugsson et al., 1998). The Ringvassøy-Loppa Fault Complex is N – S striking and made up of a series of west-dipping curvilinear normal faults. The fault complex has been interpreted by Indrevær et al. (2013) to be the northern continuation of the southern segment of the Troms-Finnmark Fault Complex. Subsidence along the fault complex most likely started in Middle Jurassic and culminated in the Cretaceous. Late Cretaceous and Cenozoic reactivation occurred (Gabrielsen et al., 1990).

The development of the fault-controlled Hammerfest Basin started in the Carboniferous with the main subsidence in the Triassic and Early Cretaceous (Larssen et al., 2005). The western Hammerfest Basin is characterised by an elongated dome structure trending the basin axis, and a system of associated east-west trending faults, reflecting Late Jurassic tectonism (1984; Gabrielsen et al., 1990; Larssen et al., 2005). The eastern part is less faulted and has the characteristics of a sag basin (Gabrielsen et al., 1990).

2.3 Stratigraphy and paleoenvironment

The stratigraphy in the western Barents Sea encompasses Late Paleozoic to Quaternary (Fig. 2.3). Information of the underlying crystalline basement is scarce, but indirect evidence suggests that it was consolidated during the Caledonian orogeny (Gudlaugsson et al., 1998).

2.3.1 Paleozoic

Rift-fill alluvial fan and floodplain clastic sediments mixed with carbonates and evaporites characterize the Upper Paleozoic sequence on the western Barents Sea (Duran et al., 2013a). Significant tectonic and climatic changes took place from Late Devonian times as the shelf moved northwards from the equatorial zone. The early

period was characterized by widespread rifting that took place along old Caledonian lineaments, and resulted in the deposition of rift-fill clastics (Billefjorden Group) (Worsley, 2008). Ceasing of the tectonic activity and sea level rise in Late Carboniferous developed the shelf into a warm-water carbonate platform, with the deposition of sabkha evaporites at the time of lowstand (Worsley, 2008; Duran et al., 2013a).

During the Permian period a change in water temperature and depth resulted in the deposition of cool-water carbonates (Bjarmeland Group) especially around the subsiding margins of the Nordkapp Basin. Late Permian experienced even cooler water conditions and deposition of siliceous shales of the Tempelfjorden Group took place (Worsley, 2008).

2.3.2 Mesozoic

The Permian – Triassic transition is poorly understood as there is a significant hiatus in latest Permian on highs and platforms (Worsley, 2008). In the Early to Middle Triassic three progradational, but strikingly different units were deposited, the Havert, Kobbe and Snadd formations. Sediments deposited along the coastline in the southwestern area were derived from the Fennoscandian Shield and the Urals (Worsley, 2008; Smelror et al., 2009).. The Havert and Kobbe formations are part of the Sassendalen Group that has been referred to as the "Early Triassic silica gap" because of the domination of non-siliceous fine clastics, and reached a thickness of 1500 m on the southwestern Barents Sea margin during a time with high subsidence and sedimentation rate (Worsley, 2008). Restricted anoxic basins south on the shelf gave rise to the organic rich Kobbe and Snadd formations (Smelror et al., 2009; Duran et al., 2013a).

During the Lower – Middle Jurassic the Tubåen, Nordmela and Stø formations were deposited. The Tubåen Formation is restricted to the western Barents Shelf due to uplift and erosion in Lower Jurassic, which is typical for the Tromsø, Hammerfest and Nordkapp basins, representing tidal inlets, estuaries and lagoons, with portions of shale and coal (Smelror et al., 2009). The Nordmela Formation consisting of silty shales and fine-grained sandstones represented a floodplain environment that during a transgression in Middle Jurassic changed to a shallow-marine environment and the deposition of stacked shoreface deposits of the Stø Formation (Smelror et al., 2009). A

sea level rise in Late Jurassic coeval with uplift of highs developed large areas of the Barents Sea into a marine shelf. A hiatus below the Late Jurassic sediments marks the onset of the Kimmeridgian tectonic phase. Anoxic seabed conditions led to deposition of the Fuglen and Hekkingen formations comprised of shale, siltstone, limestone and sandstone. The organic-rich shales of the Hekkingen Formation are considered as the main oil-prone source rock in the region (Worsley et al., 1988; Faleide et al., 1993).

In the Early Cretaceous the deposition of the Knurr and Kolje formations took place in the Barents Sea. The formations, consisting of claystone with thin stringers of limestone and dolomite took place in the Barents Sea in an open and generally distal marine environment (Worsley et al., 1988; Smelror et al., 2009). During Aptian – Albian times a transgression resulted in the deposition of shales, mudstones and siltstones of the Kolmule Formation, which top is eroded due to the Upper Cretaceous uplift (Ostanin et al., 2012; Duran et al., 2013a).

The Kveite and Kviting formations of the Nygrunnen Group were deposited in a deep to shallow shelf environment in the Late Cretaceous. While the calcareous units of the Kviting Formation were restricted to the central and eastern part of the Hammerfest Basin, the claystone dominated Kveite Formation extended across the Ringvassøy-Loppa Fault Complex and into the Tromsø Basin (Worsley et al., 1988; Ostanin et al., 2012).

2.3.3 Cenozoic

Tectonic activity controlled the deposition of the Paleogene Torsk Formation (Sotbakken Group) in an open and deep marine shelf environment, dominated by claystones interbedded with siltstones, tuffs and carbonates (Fig. 2.3) (Faleide et al., 1993). The Nordland group consisting of sandstones and claystones, rests unconformable on the Torsk Formation, and was deposited in a bathyal to glacial marine environment (Faleide et al., 1993).

The onset of the northern hemisphere glaciations in Pliocene-Pleistocene resulted in several phases of uplift and erosion in basins and highs (Reemst et al., 1994; Faleide et al., 1996). The southwestern Barents Sea continental margin prograded 30-40 km westward as a result of the erosion and redeposition on the slope (Faleide et al., 1996). Three main prograding sediment packages (GI – GIII) and seven regional seismic reflectors (R7 – R1) have been identified along the margin. The deepest reflector, R7, has

been interpreted to mark the onset of glacially-dominated deposition at 2.3 Ma (e.g. Faleide et al., 1996; Andreassen et al., 2007b; Knies et al., 2009). The deepest sediments package, GI, is interpreted to represent a glaciomarine environment with dipping clinoforms and general continuity of seismic reflections. The chaotic reflection pattern of the GII and GIII packages are interpreted to represent mass-movement deposits related to grounded glaciers along the outer shelf (Andreassen et al., 2004; 2007b).

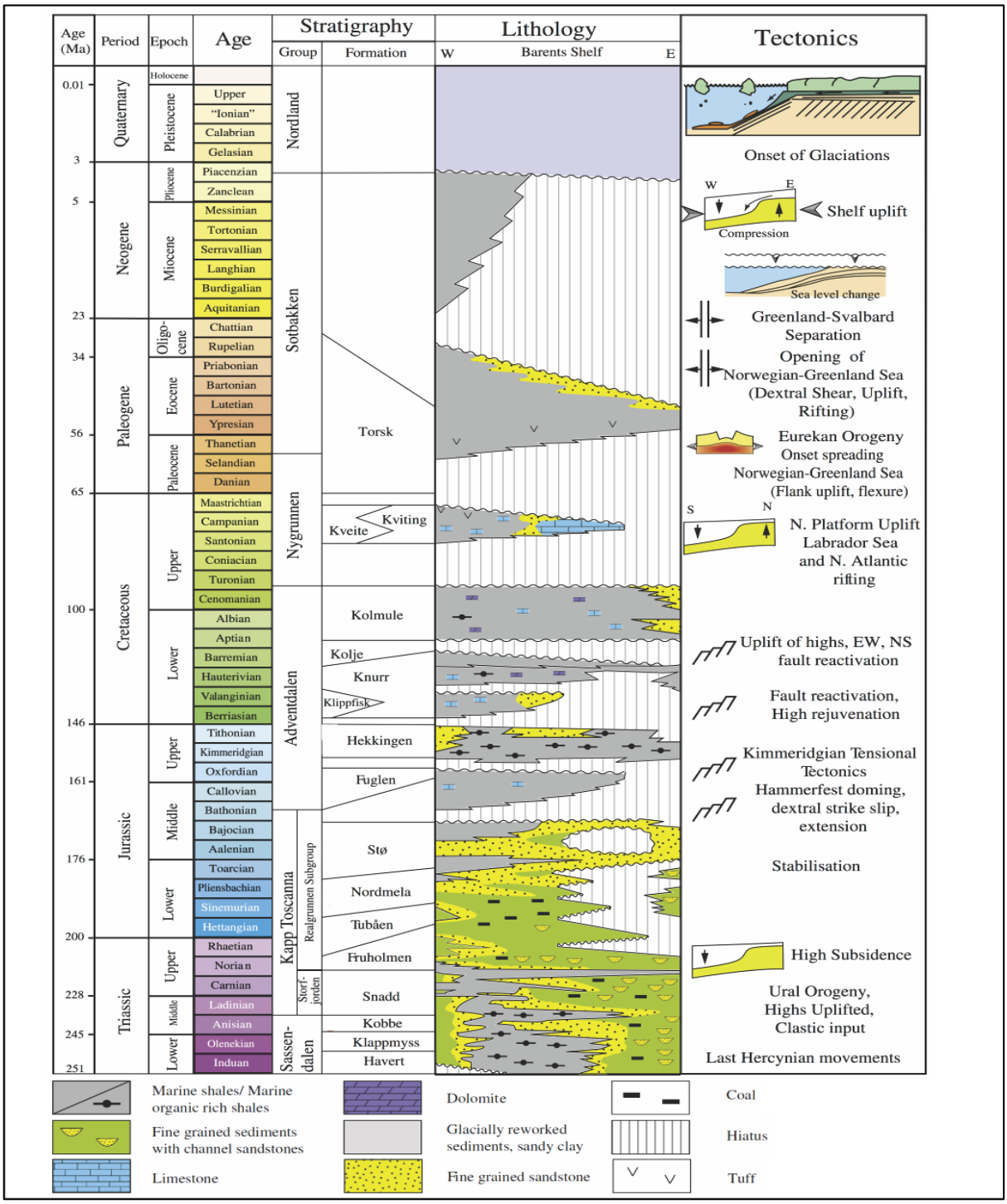

Fig. 2.3: Lithostratigraphic overview of the Barents Sea showing the main tectonic events. Figure modified from Ostanin et al. (2012).

2.4 Source rock

Exploration drilling, since the 1980s, in the Barents Sea has proven a series of source rocks of Silurian to Cretaceous age (Fig. 2.4) (Leith et al., 1992; Linjordet and Grung-Olsen, 1992; Dorè, 1995; Abrams et al., 1999; Ohm et al., 2008; Henriksen et al., 2011a). To understand the migration and accumulation of hydrocarbons within the study area, the presence of source rocks with good hydrocarbon potential is essential. A good source rock is characterized by having relatively high content of organic matter (kerogen) that can be converted to hydrocarbons given enough time and temperature. Oil is produced at lower temperatures than gas, although subjected to too high temperatures the hydrocarbon potential is reduced. Hence, knowing the burial history of the source rock is essential to understanding the hydrocarbon generation (Dorè, 1995; Dorè and Jensen, 1996; Selley, 1997; Ohm et al., 2008).

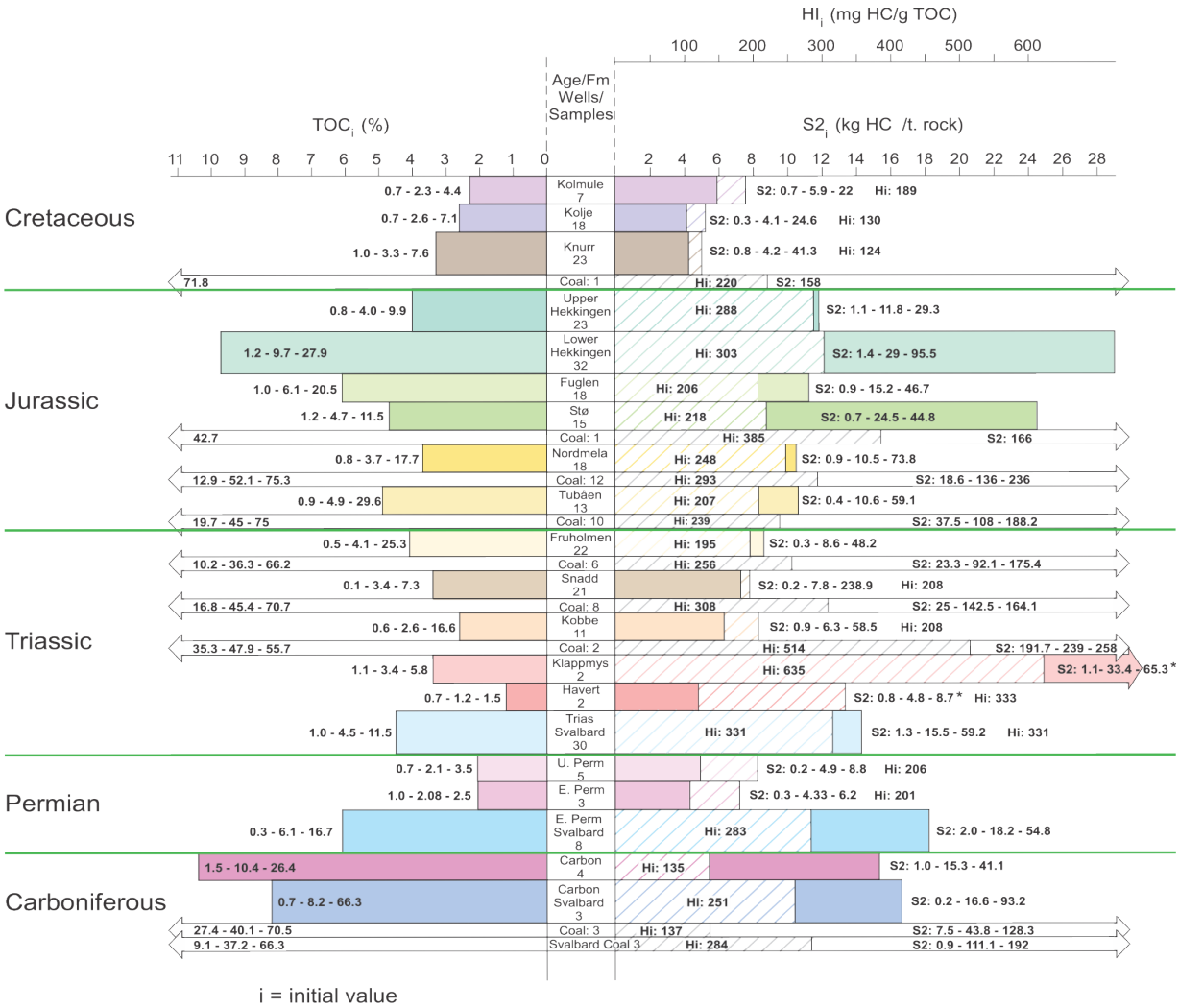

Fig. 2.4: Diagram showing the characteristics from source rocks in intervals from Carboniferous to Cretaceous, presenting the initial total organic carbon (TOC), S2, and hydrogen index (HI). Based on 32 wells the Lower Hekkingen is the most prolific source rock in the Barents Sea. Only a few wells have penetrated pre-Triassic sources, and the extent of these are less known. Figure from Ohm et al. (2008).

Compared to elsewhere on the Norwegian continental shelf, the source rocks in the Barents Sea show larger differences in maturity level, often more mature than expected, and does not follow the same trends in maturity versus depth (Ohm et al., 2008; Henriksen et al., 2011b). An explanation for this could be that the Barents shelf have higher temperature gradients than elsewhere, however, the repeating phases of uplift and erosion, since the onset of the Plio-Pleistocene glaciations, has also affected the maturity profile (Dorè, 1995; Dorè and Jensen, 1996; Knies et al., 2009; Duran et al., 2013b). The highly variable uplift and erosion, in addition to the timing of the processes, makes it difficult to predict the maturity (Henriksen et al., 2011b). In the areas of highest uplift, the cooling of the source rock may have stopped the generation of hydrocarbons, while in areas of no uplift the source rock may be overmature (Ohm et al., 2008). The uplifted source rocks will only resume generating hydrocarbons when they are subjected to higher temperatures and pressures than they experienced prior to the uplift (Dorè et al., 2000).

Potential source rocks of Triassic age are present in large parts of the southwestern Barents Sea (Fig. 2.4). They are generally buried beneath the Jurassic source rocks, and consequently maturing earlier, being in the gas window where the Hekkingen Formation is in the oil window, and overmature where the Hekkingen is in the gas window (Ohm et al., 2008). The Triassic source rocks appear to be in the oil window in the western and central parts of the Hammerfest Basin. Toward the Tromsø Basin they progressively move into the gas window before they eventually become overmature (Ohm et al., 2008; Henriksen et al., 2011a). Occasionally the Triassic source rocks have not reached mature levels on the Loppa High and the Finnmark Platform (Ohm et al., 2008). The Permian source rocks are overmature over large parts of the Barents Sea, and only in the oil window on the upper part of the Loppa High and along the margins of the Finnmark Platform (Ohm et al., 2008).

3 Data & methods

3.1 Dataset

This study is based on nine 3D seismic data sets located inside and along the margins of the Hammerfest Basin in the Barents Sea (Fig. 3.1). Wells have been used for correlation of seismic units and to determine formation tops.

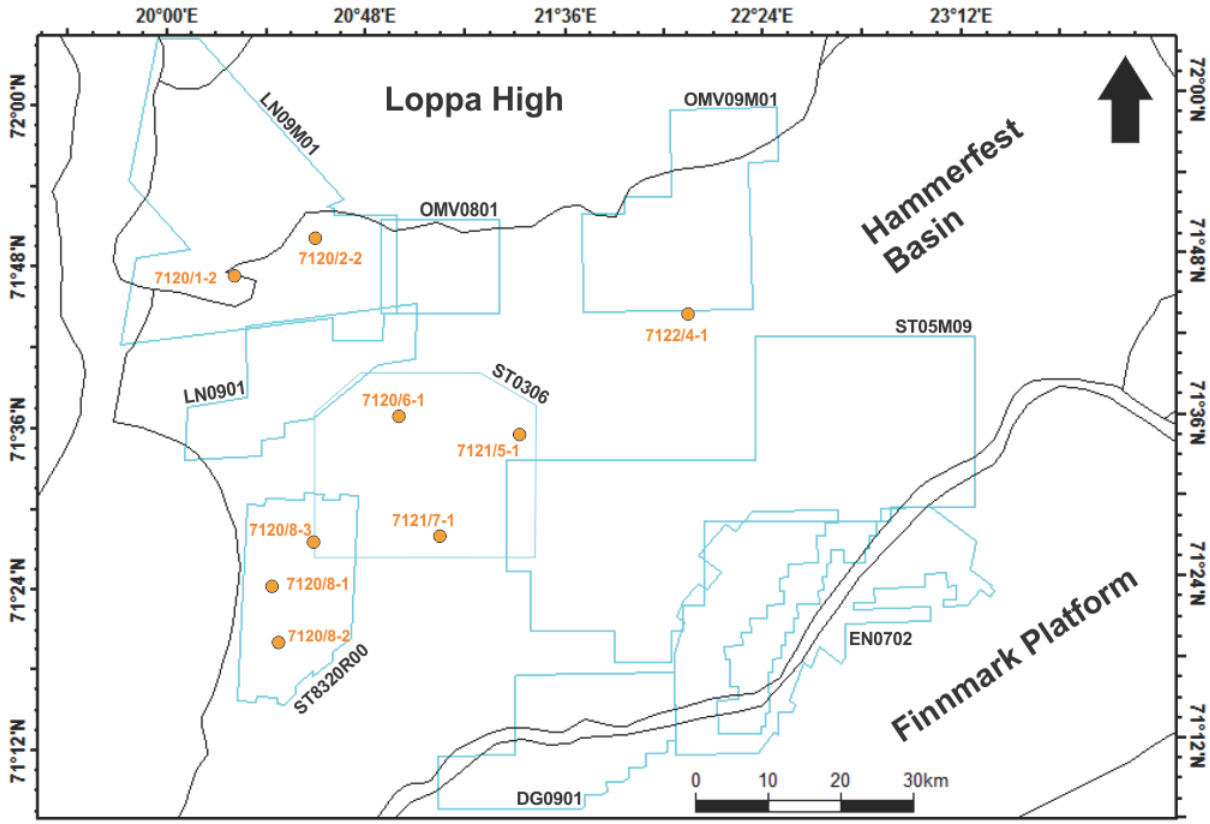

Fig. 3.1: Overview of study area showing the location of the 3D seismic datasets (blue polygons) and the wells (orange circles) used in this study. Black lines show the main structural elements enclosing the Hammerfest Basin.

3.1.1 3D seismic data

Faults and amplitude anomalies were mapped using nine 3D seismic surveys covering the Hammerfest Basin in the southwestern Barents Sea (Fig. 3.1). The phase, polarity, area and the dominating frequency for each of the datasets is given in Table 3.1.

The polarity standard that is used is the SEG of Sheriff (2006). For a zero-phase wavelet with normal polarity (SEG normal), a central positive (plotted black) amplitude correspond to an increase in acoustic impedance, or positive reflection coefficient. For a minimum-phase wavelet with normal polarity, a reflection with positive reflection coefficient begins with a negative amplitude (plotted white) followed by a positive

amplitude (plotted black) (Fig. 3.2). For reversed polarity (SEG reverse) the opposite is true, where the negative amplitude becomes a positive and the positive amplitude becomes a negative (Fig. 3.2). In this study the positive amplitude is given a blue color and the negative amplitude a red/yellow color (Fig. 3.2).

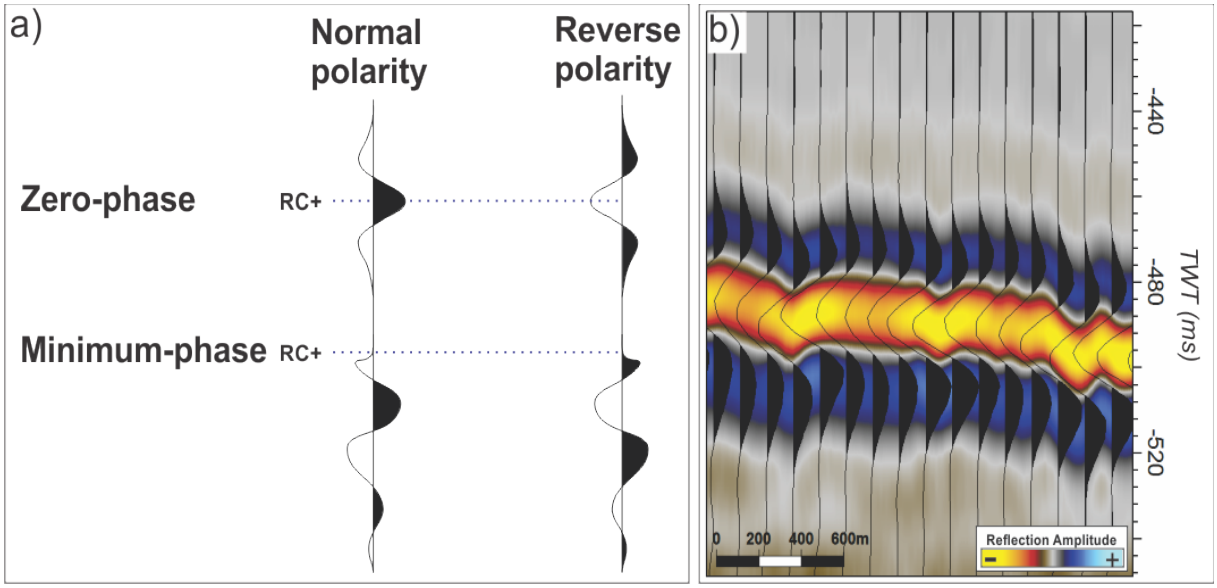

Fig. 3.2: ***a)*** *Overview of the polarity convention that is used in this study (SEG). Figure is modified from Sheriff (2006).* ***b)*** *In this study the positive amplitude is given a blue color, while the negative amplitude is given a red/yellow color. Image displays the seabed reflection, a zero-phase signal with negative polarity.*

The frequency spectrum for the datasets occurs between 6 and 67 Hz. The peak frequencies were determined by doing a spectral analysis for each of the datasets, and are presented in Table 3.1.

Survey name	***Polarity***	***Phase***	***Bandwidth (Hz)***	***Peak frequency (Hz)***	***Area (km²)***	***Inline orientation***
LN09M01	Reverse	Zero-phase	16 – 49	33	1010	N – S
LN0901	Reverse	Zero-phase	9 – 52	27	348	N – S
OMV0801	Normal	Minimum-phase	7 – 22	10	212	N – S
OMV09M01	Reverse	Minimum-phase	6 – 18	12	513	N – S
ST8320R00	Normal	Zero-phase	10 – 33	16	389	N – S
ST0306	Normal	Zero-phase	20 – 45	32	714	N – S
ST05M09	Normal	Minimum-phase	10 – 34	23	1453	E – W
DG0901	Reverse	Zero-phase	15 – 44	29	427	NE – SW
EN0702	Reverse	Zero-phase	17 – 67	56	647	NW – SE

Table 3.1: Overview of polarity and phase of the datasets used in this study. The area is the total coverage for the seismic dataset.

3.1.2 Well data

The lithostratigraphic units within the Hammerfest Basin were interpreted and tied to the seismic data using 9 exploration wells (Fig. 3.1). Correlation between datasets was done to obtain a comprehensive understanding of both the stratigraphy and depositional environment in the study area. In order to be able to calculate fault throw and determine the thickness of geologic features, the velocity for each of the lithostratigraphic units was estimated by combining the depths of the units with a velocity-depth profile. In this study a velocity-depth profile, established by Storvoll et al. (2005), was used. The profile were put together by using caliper, bulk density, deep resistivity and velocity log data from 13 exploration wells within the southwestern Barents Sea (Fig. 3.3a) (Storvoll et al., 2005). To obtain a representative velocity for the entire Hammerfest Basin, the average depths for the top of each of the geologic formations were calculated using well data from 9 wells (Fig. 3.1) acquired from the NPDs fact pages (NPD, 2015). For the water column and the Quaternary sediments above the URU, a velocity of 1500 m/s and 1700 m/s, respectively, is used (Andreassen et al., 2008; Chand et al., 2008). The velocity for pre-Quaternary sediments is indicated in Table 3.2.

Interval	***Top depth TWT (ms)***	***Top depth TVD (m)***	***Velocity (m/s)***
Water column	-	-	1500
Nordland GP	413	330	1700
Torsk FM	476	491	2000
Kviting/Kveite FM	1055	1089	2300
Kolmule FM	1142	1150	2500
Kolje FM	1575	1798	2600
Knurr FM	1750	2013	3000
Hekkingen FM	1857	2126	3200

Table 3.2: Overview of the velocity that will be used for calculating fault throw and thickness of geologic features in the study area. Velocity for the water column and the Nordland Group sediments were obtained from Andreassen et al. (2008) and Chand et al. (2008). Velocity of the Torsk – Hekkingen formations were calculated from the velocity-depth profile in Fig. 3.3b that were established by Storvoll et al. (2005). The average depth (TVD) of the geologic formation were obtained from NPD (2015).

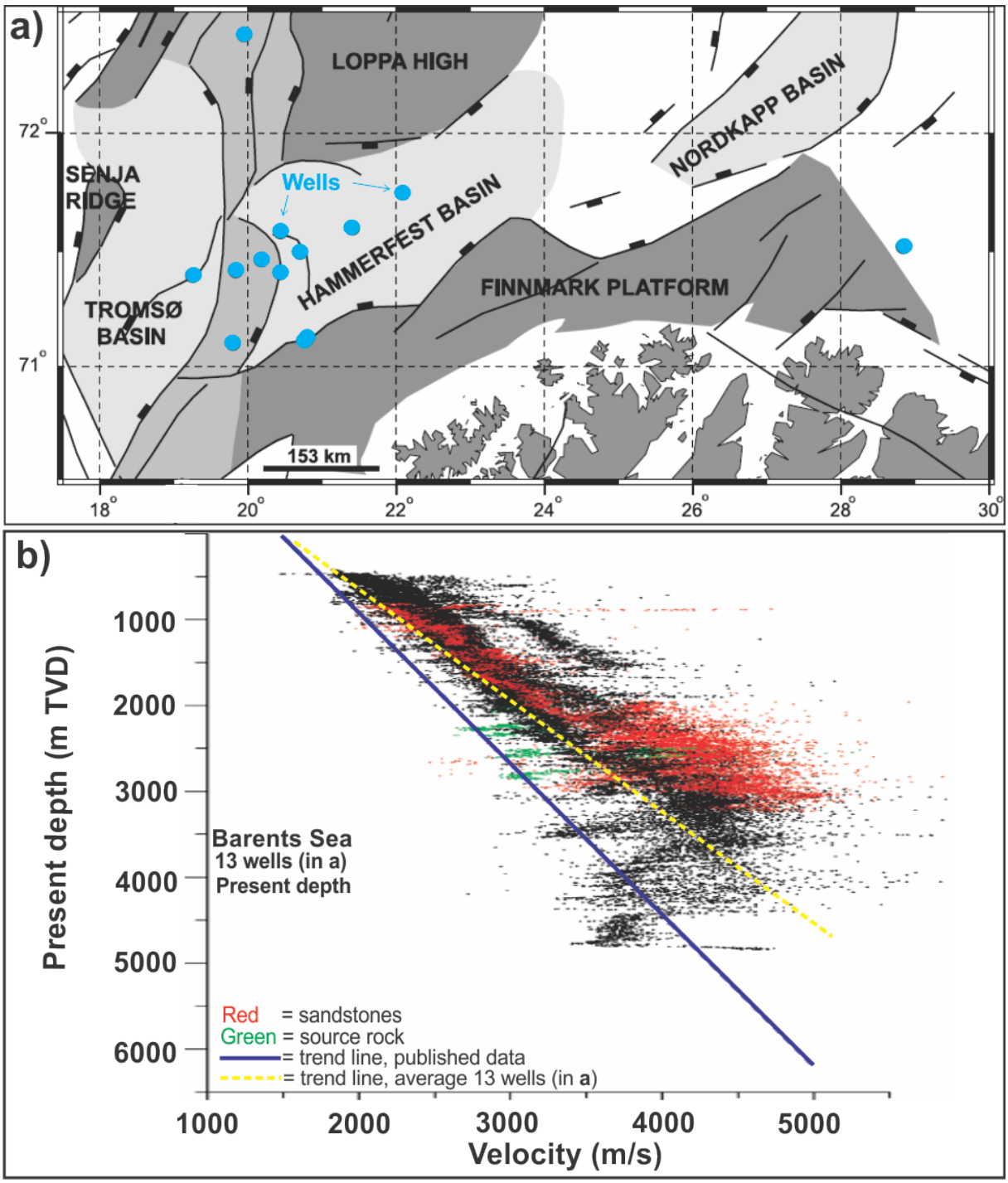

Fig. 3.3: ***a)*** *Overview of wells (blue circles) and the main structural elements in the southwestern Barents Sea.* ***b)*** *Sonic velocity measurements at present burial depth from the 13 wells in* ***a****. Velocities of sandstones are shown in red, shales in black and Hekkingen source rock in green. Blue line represents average velocities from wells from the North Sea, Norwegian Sea and Barents Sea. Yellow line represents the average velocities from the wells in* ***a****. Both figures modified from Storvoll et al. (2005).*

3.2 Seismic resolution

Seismic resolution has both vertical and horizontal aspects, and is defined as the ability to distinguish between two individual reflectors (Sheriff, 1985; Brown, 2004). The resolvability of seismic data is given in terms of the seismic wavelength (Equation 3.1).

$$\lambda = \frac{v}{f} \qquad \text{(Equation 3.1)}$$

λ = Wavelength (m)

v = Velocity (m/s)

f = Frequency (Hz)

Seismic resolution decreases with depth as the seismic wavelength increases (Fig. 3.4). Velocity will normally increase with depth as the rocks become older and more compacted, while the frequency will decrease because the higher frequencies of the seismic signal are attenuated at a faster rate than the low frequencies (Brown, 2004).

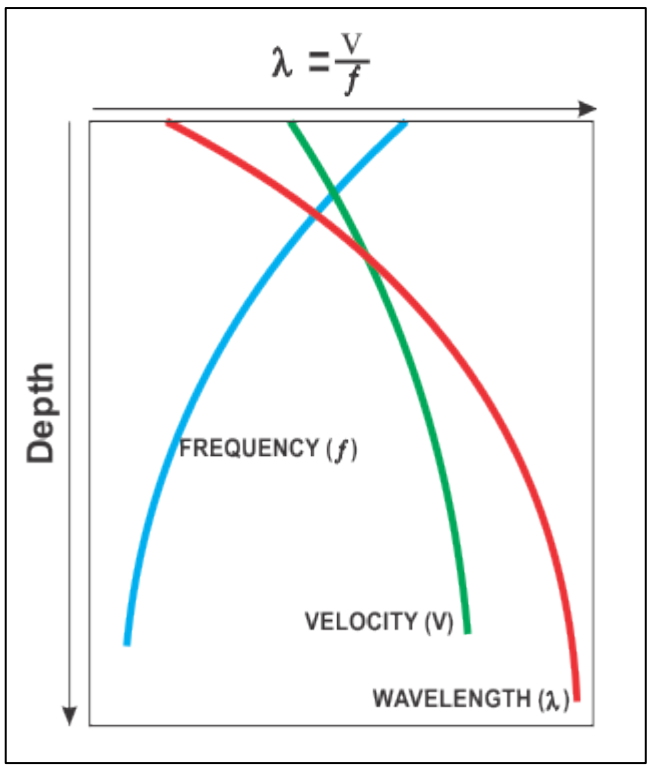

Fig. 3.4: The wavelength of the seismic wave increase with depth, reducing the resolution of the seismic data. Figure modified from Brown (2004).

3.2.1 Vertical resolution

The vertical resolution, also referred to as the limit of separability, is the ability to identify the top and base of a thinning sedimentary bed, and is given by the Equation 3.2 (Brown, 2004; Bulat, 2005).

$$Vr = \frac{\lambda}{4} \qquad \text{(Equation 3.2)}$$

Vr = Vertical resolution (m)

λ = Wavelength (m)

When two reflecting interfaces are separated by more than half of a wavelength, the wavelets will not interfere and two separate reflections will be produced. When the separation of the interfaces approaches a quarter of a wavelength, the top and base interferes constructively and merges into one waveform and produce an amplitude increase. Below a quarter of a wavelength destructive interference occur until the limit of visibility is reached and the signal becomes obscured by the background noise (Sheriff, 1985; Brown, 2004; Bulat, 2005). It is important to be aware that the vertical resolution of a quarter of a wavelength also is valid for the seabed reflection. The reflection will represent the average reflection response of the seabed and the near seabed sediments, so that the seismic seabed image may be dominated by the geomorphology of the underlying glacigenic accumulations (Bulat, 2005). The vertical resolution for the 3D seismic datasets is shown in Table 3.3. An average velocity of 2300 m/s is used to calculate the resolution (Table 3.2).

Survey name	***Peak frequency (Hz)***	***Wavelength (m)*** $\lambda = v/f$ ***(V_P = 2300 m/s)***	***Vertical resolution (m)*** $V_r = \lambda/4$
LN09M01	33	69.7	17.4
LN0901	27	85.1	21.3
OMV0801	10	230	57.5
OMV09M01	12	191.7	47.9
ST8320R00	16	143.7	35.9
ST0306	32	71.8	17.9
ST05M09	23	100	25
DG0901	29	79.3	19.8
EN0702	56	41.1	10.2

Table 3.3: Overview of the vertical resolution for the 3D seismic datasets used in this study. An average velocity of 2300 m/s (Table 3.2) is assumed for the subsurface sediments and is used to calculate the resolution.

3.2.2 Horizontal resolution

The concept of the Fresnel zone is commonly used when discussing the horizontal resolution, and is the ability to distinguish between two adjacent reflectors in the subsurface (Bulat, 2005; Chaouch and Mari, 2006). Chaouch and Mari (2006) defined the Fresnel zone (often referred to as the first Fresnel zone) as the subsurface area that reflects energy that arrives at the geophone/hydrophone within a half-cycle. The subsurface area that produce the reflection is indicated in Fig. 3.5 where the wavefront is tangent to the reflecting interface, and is limited by the area that the wavefront arriving quarter of a wavelength later makes with the reflector. High frequencies give a better resolution for the seismic data than the lower frequencies, but less penetration (Fig. 3.5). For an unmigrated seismic data, the radius of the Fresnel zone is given by Equation 3.3. (Sheriff, 1985; Chaouch and Mari, 2006).

$$rf = \frac{v}{2}\sqrt{\frac{t}{f}} \qquad \text{Equation 3.3}$$

rf = Radius of the Fresnel Zone (m)

v = Velocity (m/s)

t = Two-way travel time (s)

f = Dominant frequency (Hz)

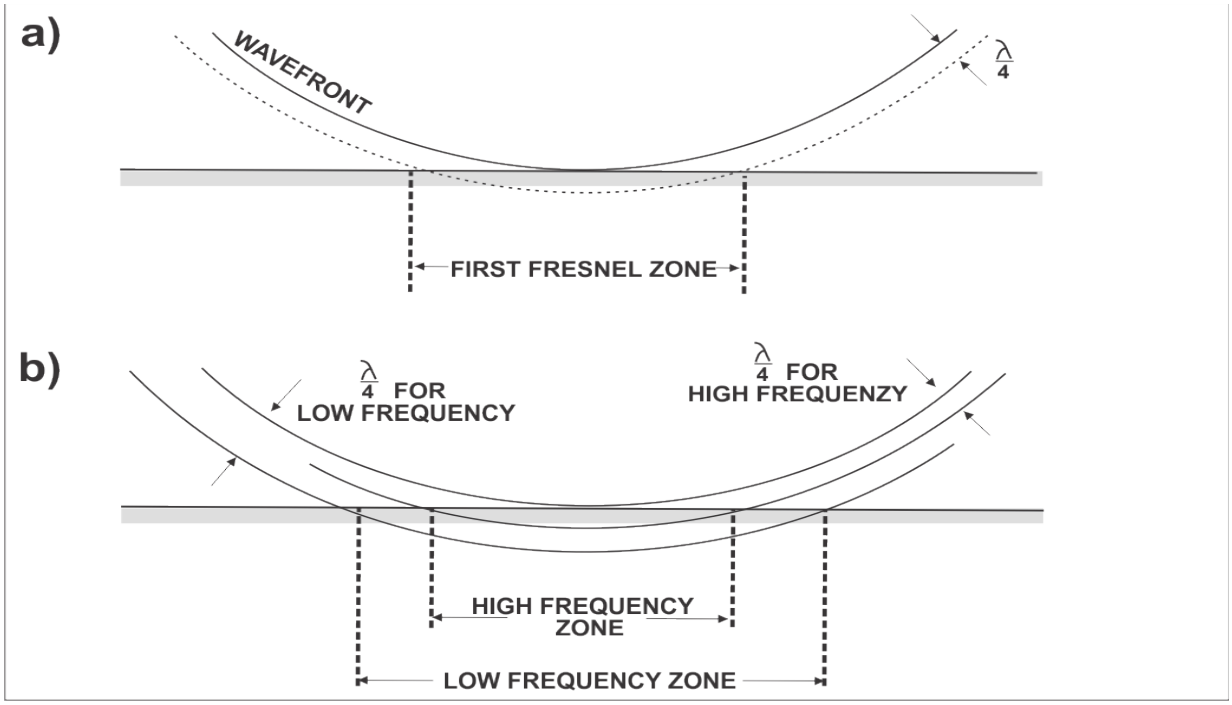

Fig. 3.5: ***a)*** *The Fresnel Zone is the area defined by point where the wavefront is tangent to the reflecting interface and is limited by the area that the wavefront arriving quarter of a wavelength later makes with the reflector.* ***b)*** *Higher frequency results in smaller Fresnel Zone, hence better resolution. Figure modified from Sheriff (1985).*

In migrated seismic data the horizontal resolution is improved by shrinking the Fresnel zone. For 2D seismic data the migration only allows the Fresnel zone to be collapsed in the inline direction to an ellipse (Fig. 3.6). For 3D seismic data the Fresnel zone is reduced to a small circle (Fig. 3.6), hence the energy is better focused and resolution improved. The horizontal resolution for migrated seismic data is given by Equation 3.4 (Sheriff, 1985; Brown, 2004; Bulat, 2005). Table 3.4 shows the resolution for the 3D seismic datasets used in this study using an average p-wave velocity of 2300 m/s (Table 3.2).

$$Hr = \frac{\lambda}{4} \qquad \text{Equation 3.4}$$

Hr = Horizontal resolution (m)

λ = Wavelength (m)

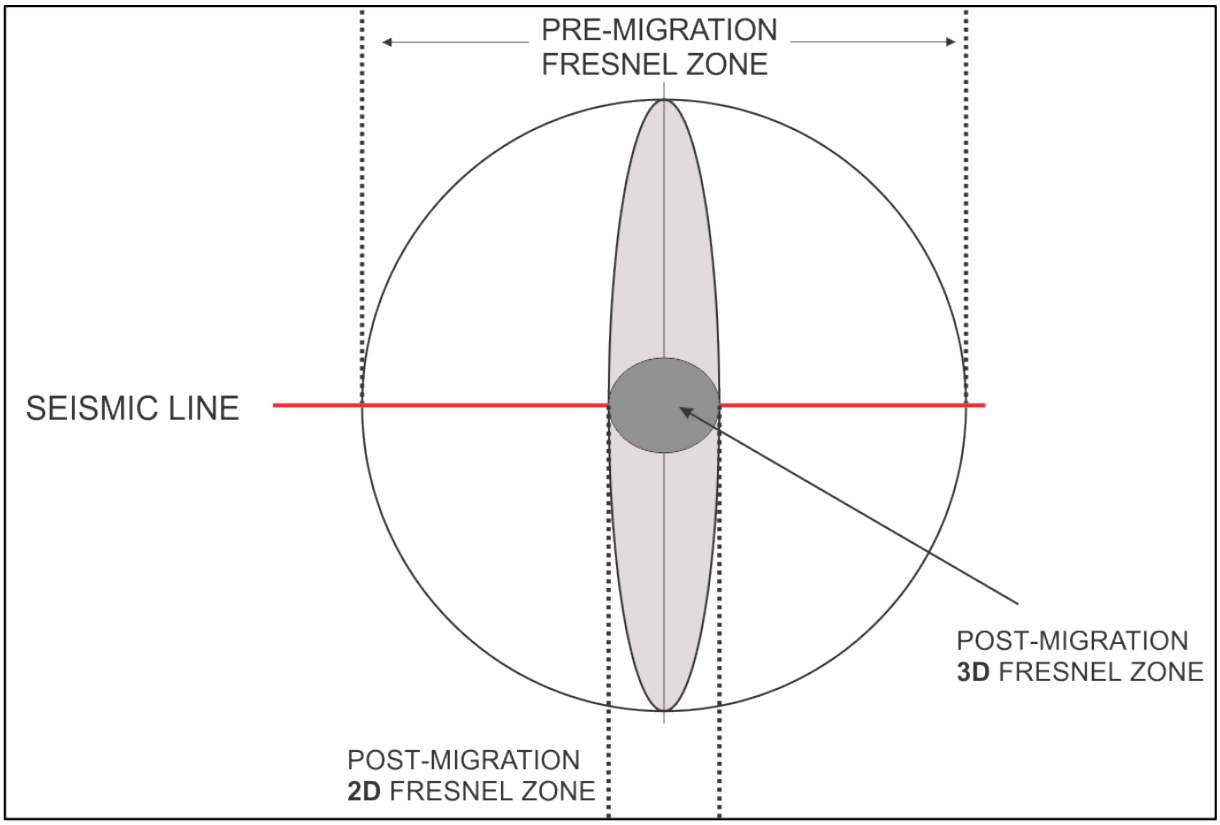

Fig. 3.6: The effect that migration has on the size on the Fresnel Zone. Migration on 2D seismic data allows only the Fresnel Zone to be collapsed in inline direction while migration of the 3D seismic data can reduce the Fresnel Zone to a small circle. Figure is modified from Brown (2004).

Survey name	*Peak frequency (Hz)*	*Wavelength (m)* $\lambda = v/f$ *(V_P = 2300 m/s)*	*Horizontal resolution, pre-migration (m)*	*Horizontal resolution, post- migration (m)*
LN09M01	33	69.7	156.4	17.4
LN0901	27	85.1	172.9	21.3
OMV0801	10	230	284.2	57.5
OMV09M01	12	191.7	259.4	47.9
ST8320R00	16	143.7	224.6	35.9
ST0306	32	71.8	158.8	17.9
ST05M09	23	100	187.4	25
DG0901	29	79.3	166.9	19.8
EN0702	56	41.1	120.1	10.2

Table 3.4: Overview of the horizontal resolution (both pre- and post-migration) for the 3D seismic datasets used in this study. An average velocity of 2300 m/s (Table 3.2) is assumed for the subsurface sediments and is used to calculate the resolution at Top Kviting/Kveite Formation (1055 ms TWT).

3.3 Artefacts

All seismic datasets used in this study do to some degree show artefacts in the form of survey footprints (Fig. 3.7). Survey footprints occur as parallel lines in the seismic image and its systematic noise correlates with the acquisition geometry of the survey, as they have the same orientation as inlines (Chopra and Larsen, 2000; Bulat, 2005). Such artefacts are most prominent in the oldest surveys (ST8320R00, ST0306 and ST05M09). They can complicate the process of identifying seabed and subsurface features. In the examples shown, seismic profiles including the noise suggest small time-shifts between lines that can be easily mistaken to represent faults and seismic pipes (Fig. 3.7) (Bulat, 2005). Thus the interpreter needs to be more careful using older 3D seismic data.

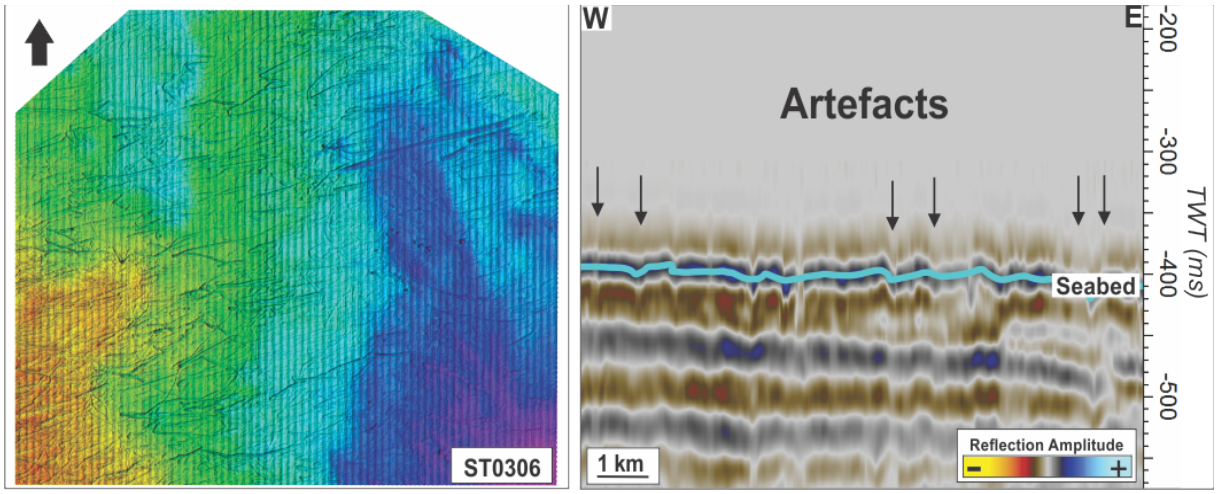

*Fig. 3.7: **a)** Survey footprints parallel to the inlines of survey ST0306. **b)** Seismic section perpendicular to the footprints in **a**. The noise is similar to faults and pipe structures and could be mistaken to represent actual features.*

3.4 Interpretation methods

In this study the Petrel 2014 software from Schlumberger was used to visualize and interpret the 3D seismic data. The Petrel software comprises several tools and features that has been used to perform seismic interpretation, create horizons and generate attributes of horizons and volumes. The depth of the seismic data is presented in two-way time (TWT) and is given with negative sign (e.g. -2500 ms TWT). Figures were created and modified using the CorelDraw X6 software from Corel Corporation.

3.4.1 Interpretation of the seismic data

Seismic horizons in the seismic datasets were interpreted using seeded 2D autotracking where seeds on every 50 – 100 inline and crossline were picked. Seeded 3D autotracking and the paintbrush function in Petrel 2014 were used to fill in the areas between the in- and crosslines. The seabed is represented by a strong and continuous reflection and was interpreted on peak events (troughs for reversed polarity), as this provided the best seismic horizons. Interpretation of the URU was carried out on zero-crossings between peaks and troughs as the continuity of the URU reflection varied laterally. Cropping of seismic volumes in the x, y and z domain was done to increase the work rate and improve the performance.

3.4.2 Seismic attributes

Seismic attributes are useful for visualizing and enhance the geological understanding of the seismic interpretations. Chopra and Marfurt (2005) defined a seismic attribute as a quantitative measure of a seismic characteristic of interest, meaning that seismic attributes can provide more information of the geometry or physical parameters of features or patterns observed in the subsurface (Chopra and Marfurt, 2005). In this study several seismic attributes were used to identify and map faults, amplitude anomalies and morphological features.

Structural smoothing is an attribute used to smooth the input signal guided by the local structure. Reflection continuity is increased at the same time as important discontinuities, e.g. faults, are preserved (Schlumberger, 2010).

Discontinuities in the horizontal continuity of amplitudes are highlighted when creating a variance attribute cube. The attribute estimates the local variance in the input signal

and can be used to map buried deltas and channels (Chopra and Marfurt, 2005; Schlumberger, 2010). In this study the variance attribute cube was used to map and identify both large- and small-scale faults. Time-slices were created at various depths to ensure accurate and detailed mapping.

The chaos in the seismic signal was visualized by generating a chaos attribute cube, which is a measure of the "lack of organization" in the dip and azimuth estimation method (Schlumberger, 2010). Similar to the variance attribute the chaos attribute was utilized to map faults, but also identify gas chimneys and other gas migration paths. To map the vertical extent of gas chimneys time slice were created at various depths.

RMS attribute is used to highlight strong amplitudes in a specified volume. The tool computes the square root of the sum of squared amplitudes divided by number of samples (Schlumberger, 2010). The attribute was used to identify and delineate boundaries of amplitude anomalies within the study area.

4 Results

This chapter presents the observations and interpretations done for the nine seismic datasets located in and along the margins of the Hammerfest Basin (Fig. 4.1). The main focus has been to map the vertical and lateral distribution of faults and amplitude anomalies above the Base Cretaceous Unconformity (BCU). Extensive surface interpretation of the upper regional unconformity (URU) and the seabed reflection are aimed to link deeper structures to shallower morphological features. The focus on the regional understanding and the large extent of the study area (approximately 5700 km^2) has resulted in the use of large-scale maps, which prevented to some degree a detailed and comprehensive descriptions of individual features. Some of the faults, amplitude anomalies and related structures have previously been described and interpreted by other published works (e.g. Martens, 2009; Kristensen, 2010; Ostanin et al., 2012; Ostanin et al., 2013; Arvo, 2014), and have, in addition to new features, been described and included in this study.

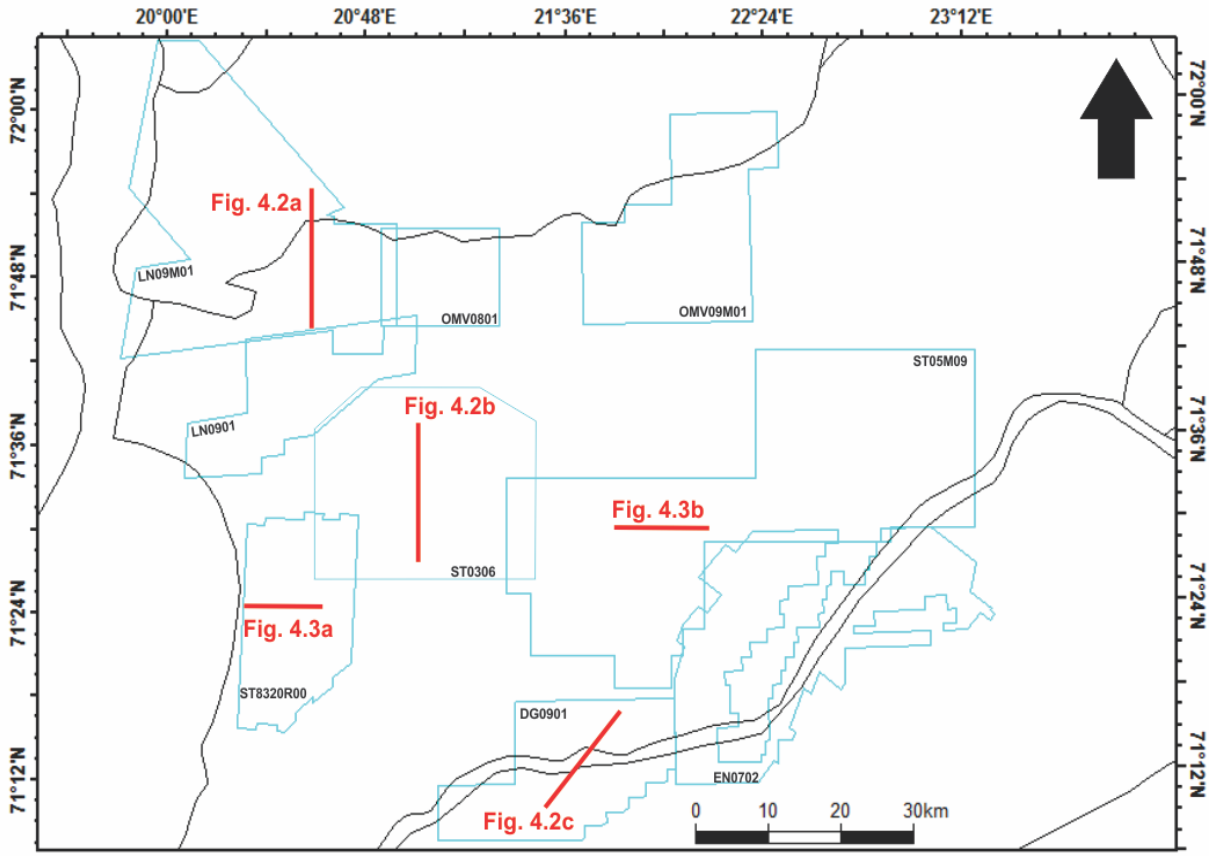

Fig. 4.1: Overview of the study area in the southwestern Barents Sea, indicating the main structural elements (black lines) and the locations of the 3D seismic datasets (blue polygons).

4.1 Seismic stratigraphy

The complex structural and sedimentary history of the Barents Sea is revealed by multiple strong and prominent seismic reflections. The seismic stratigraphy in the Hammerfest Basin is determined by use of well data located within the study area (Fig. 3.1). The focus of this study encompasses the geologic history from the Base Cretaceous to the present, hence less attention has been given to deeper levels. Formation tops from the Top Hekkingen level up to Top Torsk Formation has been obtained from NPD (NPD, 2015) to create a basic stratigraphy of the basin. All stratigraphic units can be identified in all the datasets, except for survey ST05M09 where only the upper 1100 ms (TWT) of the seismic data is available.

The Top Hekkingen Formation characterises a strong, continuous, negative reflection coefficient that can be easily identified in all the seismic surveys. Multiple faults and fault complexes across the Hammerfest Basin affect the formation top. The depth of the formation top varies across the Hammerfest Basin where the deepest part (2.4 – 2.6 s (TWT)) occurs in the northwest close to the Loppa High (Fig. 4.2a). Southwards in the basin the depth gradually decreases to about 2.0 – 2.2 s (TWT) in the centre (Fig. 4.2b), and 1.6 s (TWT) at the southern margin (Fig. 4.2c). Likewise, the depth decreases towards the Bjarmeland Platform in the east – northeast, but no quantification exists due to a lack of seismic data.

The Lower Cretaceous Knurr Formation is placed unconformable on top of the Hekkingen Formation, and its top is characterized by a continuous reflection with a strong negative reflection coefficient. The depth of the formation appears to increase toward to west – northwest. Close to the Loppa High the formation occurs between 2.1 s and 2.4 s (TWT) (Fig. 4.2a), and show low-amplitude and continuous internal reflections where the formation thickness is sufficient. In the centre and toward the southern margin of the Hammerfest Basin the thickness decreases and the formation mainly occur between 1.6 s and 1.7 s (TWT) (Fig. 4.2bc). The Knurr Formation is affected by faults to the same extent as the Hekkingen Formation.

The Kolje Formation is most prominent in the northern and western part of the Hammerfest Basin, and thins toward the south and east (Fig. 4.2). In the northwest the

Kolje Formation mainly occur between 1.6 s and 1.9 s (TWT), and between 1.5 s and 1.6 s (TWT) in the south. The top of the formation characterises a continuous low-amplitude reflection with a positive reflection coefficient. The lower parts of the formation show internal reflections with good continuity and low frequency. Upwards the reflections become discontinuous and appear to be chaotic (Fig. 4.2). A number of faults terminate within and across the Kolje Formation, but they do not appear to be as intensive as in the Hekkingen and Knurr formations.

The Kolmule Formation exists in the entire Hammerfest Basin. The thickness appears to be at its highest in the southern and eastern areas. In the south the Kolmule Formation occurs between 0.9 s and 1.6 s (TWT) (Fig. 4.2c), while in the northeast (survey OMV09M01) it mainly occurs between 0.8 s and 1.7 s (TWT) (Fig. 4.2ab). Towards the northwest the Kolmule Formation gradually thins before it pinches out towards the Loppa High. The lowermost part of the formation characterizes internal chaotic reflections, while further up a few low-amplitude reflections with low continuity appear in seismic cross-sections (Fig. 4.2). The top of the Kolmule Formation characterizes a strong reflection with a positive reflection coefficient. The continuity of the top reflection is interrupted by small faults extending from the overlying Kviting/Kveite Formation.

The Upper Cretaceous Kviting/Kveite Formation exists as a thin and narrow layer deposited unconformable on the Kolmule Formation, dipping mainly towards west-northwest. The Kviting/Kveite Formation characterizes strong reflections with low continuity, where small faults occur frequently principally in the westernmost areas (Fig. 4.2b). Along the Loppa High the formation is relatively thin and occurs mainly between 1.1 s and 1.3 s (TWT), before it pinches out toward the high itself (Fig. 4.2a). At the centre and southern part of the Hammerfest Basin the formation thickens and occurs between 0.8 s and 1.2 s (TWT). Several deep-seated faults penetrate the formation.

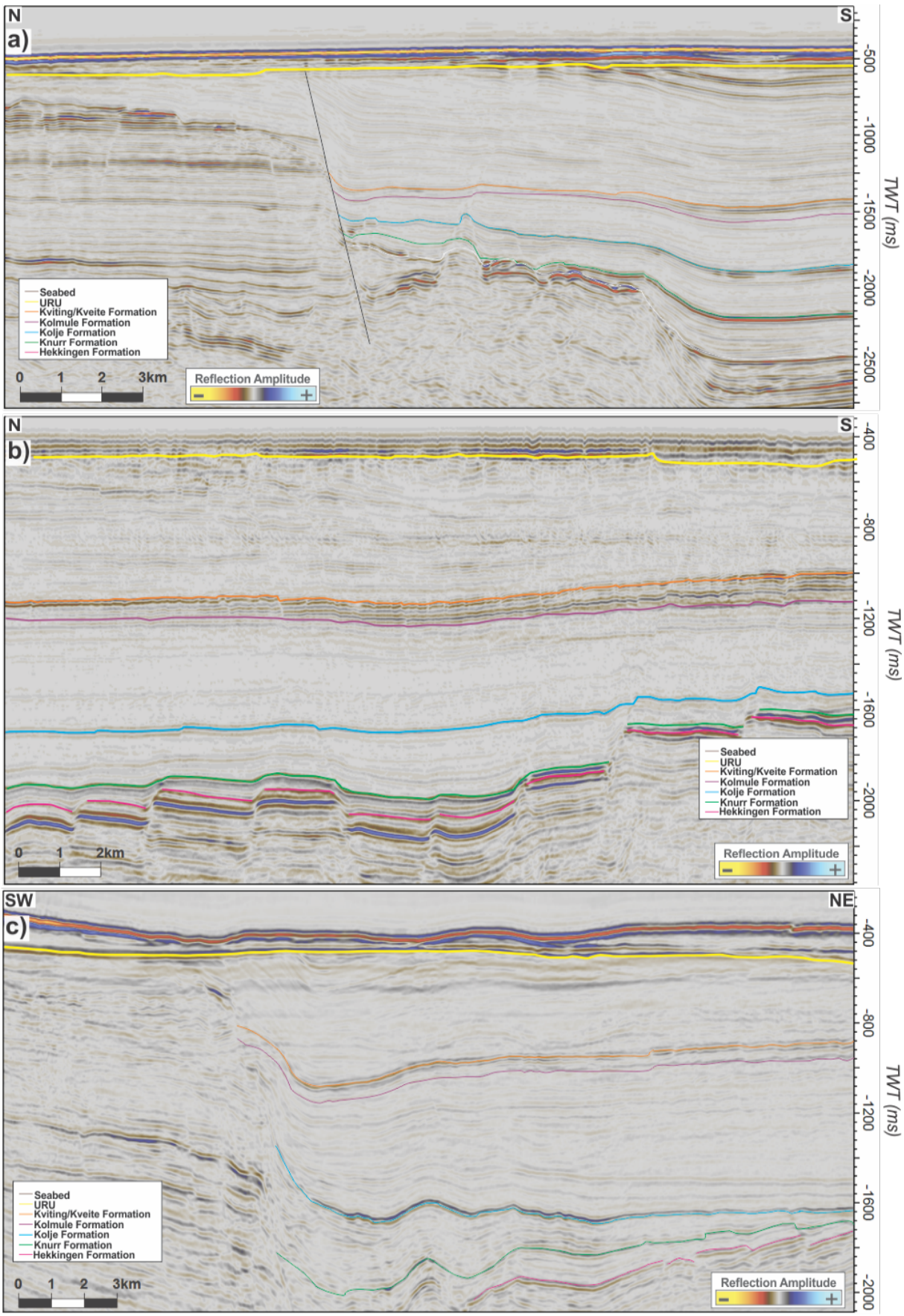

Fig. 4.2: ***a-c)*** *Seismic sections showing the stratigraphic tops within the Hammerfest Basin. Positions of* ***a-c*** *indicated in Fig. 4.1.*

The Paleocene-Eocene Torsk Formation exists in the entire study area and is deposited unconformable on top of the Kviting/Kveite Formation. It occurs between 300 ms and 1500 ms (TWT) and is thickest in the northwest (Fig. 4.2a). The reflection configuration in the lower parts of the Torsk Formation varies laterally across the basin. In the centre and along the southern margin, toward the Finnmark Platform, the formation show chaotic low-amplitude reflections with low continuity (Fig. 4.2bc). In the northern area against the Loppa High, the reflections in the lower part show slightly higher continuity and frequency. The upper part of the Torsk Formation is dominated by clinoforms dipping towards the south – southwest. The clinoform reflections show high continuity and frequency with low to medium amplitudes. The top of the clinoforms are truncated by a regional unconformity, the URU (see descriptions below).

4.1.1 Upper Regional Unconformity

The Barents Sea region has been influenced by several glaciations since Plio-Pleistocene (e.g. Vorren et al., 1991; Andreassen et al., 2007b; Knies et al., 2009). A regional reflection representing the upper regional unconformity (URU) represents the interface between underlying sedimentary bedrocks and overlying glacigenic deposits, the Nordland Group (Solheim and Kristoffersen, 1984; Vorren et al., 1991; Andreassen et al., 2008). The URU is commonly characterised by a high amplitude reflection indicating a positive reflection coefficient (Fig. 4.3bc). Generally the URU reflection shows high continuity and is thus relatively unproblematic to identify, although occasionally it is affected by truncated clinoforms of the underlying Torsk Formation, challenging the mapping process.

The URU has been identified in all datasets used in this study (Fig. 4.3a). In the southwestern area the unconformity is typically located between 50 and 70 ms (TWT) below seabed. Northwards towards the Loppa High and eastwards into the eastern part of survey ST05M09, the Plio-Pleistocene sedimentary package thins and the URU reflection coincides with the seabed reflection (Fig. 4.3c). The URU is shallowest in the west but gradually deepens towards east/northeast. The Nordland Group, where sufficiently thick, is characterized by weak internal reflections.

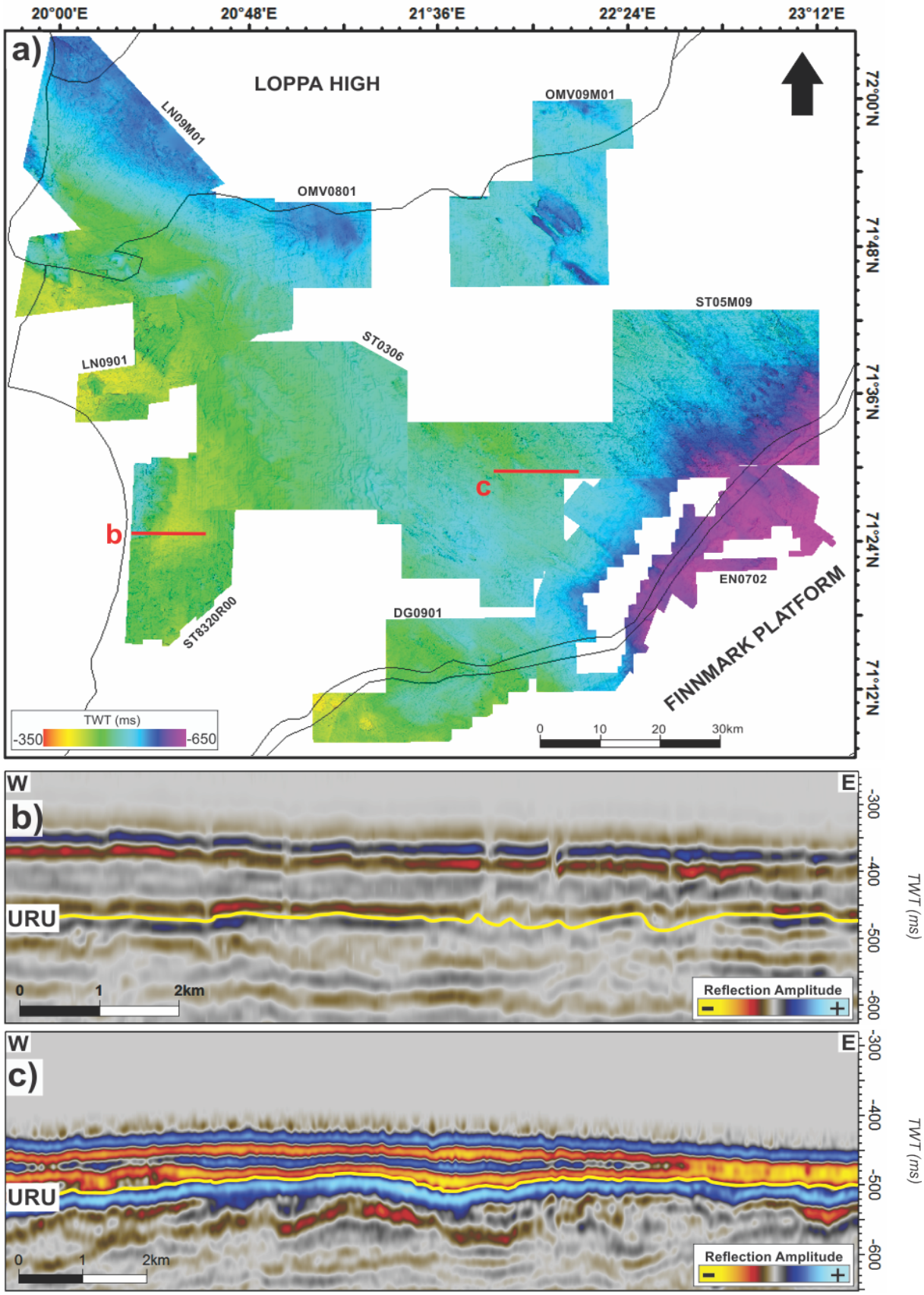

Fig. 4.3: ***a)*** *Overview of the mapped URU reflection within the study area along with the main structural elements (black lines).* ***b & c)*** *Seismic cross-sections indicating the URU reflection (yellow line) and its position relative to the seabed reflection. Position of* ***b*** *&* ***c*** *is indicated in* ***a****. URU reflection coincides with the seabed reflection eastwards, in* ***c****.*

4.2 Faults

Several faults have been identified and mapped in the seismic datasets used in this study (Table 4.1). Based on their vertical extent two groups exist: *deep-seated faults* and *shallow faults*. The deep-seated faults are defined as faults extending from the Base Cretaceous into younger strata. Faults that terminate at or below the Base Cretaceous are not mapped due to the scope of this study. The shallow faults are defined as faults that are restricted to the Cenozoic Torsk Formation.

The deep-seated faults appear to affect different stratigraphic levels across the Hammerfest Basin and have been classified with respect to the formation they terminate within. The lack of seismic data below 1100 ms (TWT) in survey ST05M09 restricted the identification of faults in the eastern part of the basin to a minimum, hence only the most obvious faults in the western part of the survey were mapped.

The shallow faults are observed and mapped in all seismic surveys except for ST8320R00, ST05M09 and OMV09M01, where the poor seismic quality of the seismic data limited observations and interpretations. Thus the variable quality of datasets may have influenced the number and distribution of shallow faults that has been identified. Also, the horizontal and vertical resolution may not be sufficient to detect minor faults with infinitesimal throw.

Fault group	***Orientation***	***Affected interval***
First order (F1)	E – W / NE – SW	Jurassic – Plio-Pleistocene (reaching the URU)
Second order (F2)	N – S E – W NE – SW	Jurassic – Plio-Pleistocene (terminating below the URU)
Third order (F3)	E – W NE – SW	Jurassic – Lower Cretaceous
Shallow faults	NW – SE / NE – SW / E – W	Plio-Pleistocene

Table 4.1: Summary and description of groups and types of faults within the study area. F1 – F3 are termed deep-seated faults.

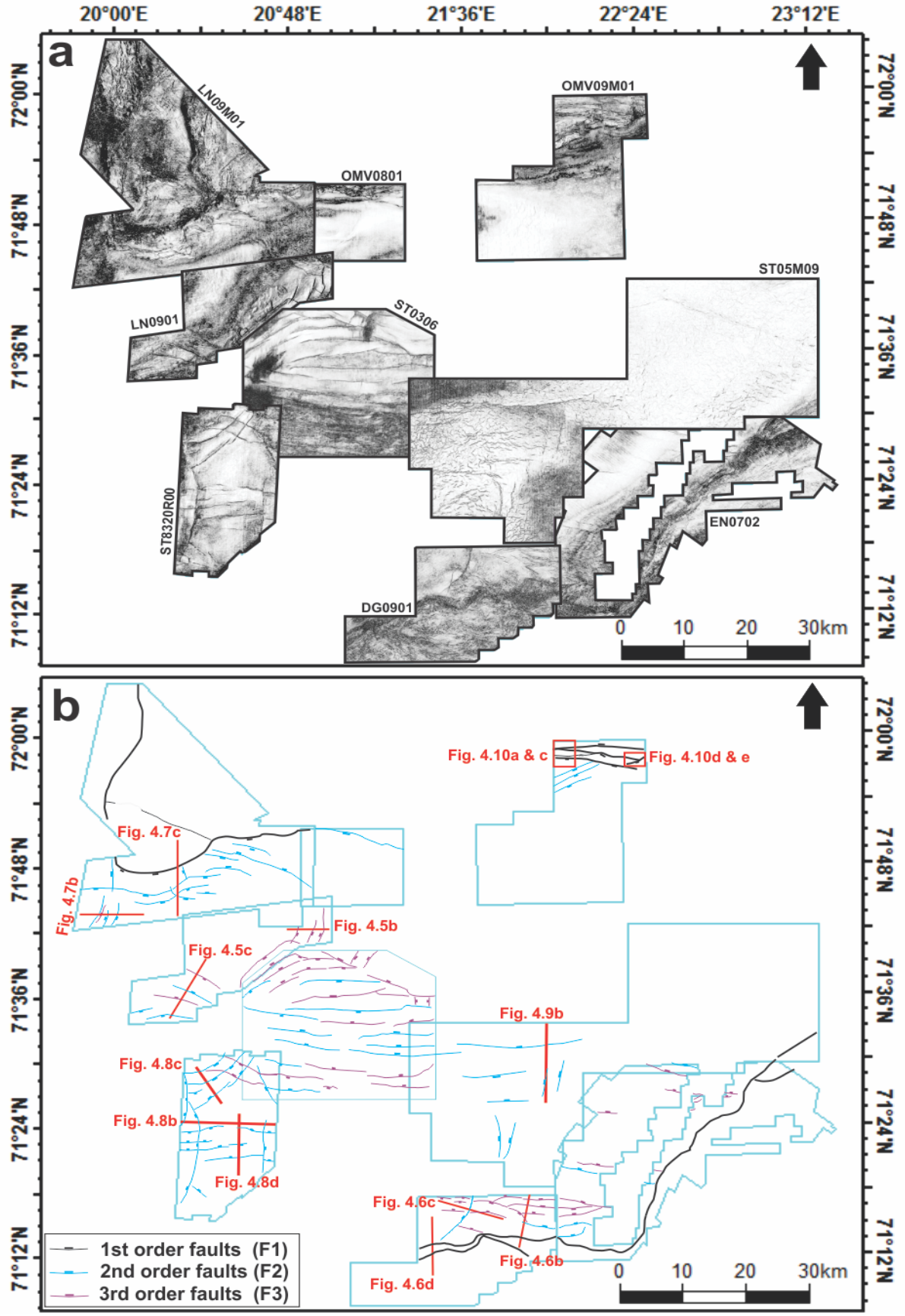

Fig. 4.4: Overview picture of the deep-seated faults within the study area. ***a)*** *Variance time slices used to map and identify faults. Depth (TWT) of time slices indicated in Table 4.2.* ***b)*** *Location of deep-seated faults based on* ***a****. Colours on faults indicate what geologic formation the deep-seated faults terminate within (see legend lower left corner).*

4.2.1 Deep-seated faults

The seismic data reveal several faults and fault complexes within the study area (Fig. 4.4). The deep-seated faults appear to have three dominating strike orientations: N – S, NE – SW and E – W (Table 4.1), and appear to be extensional features. The fault throw varies along strike and in dip direction, having the largest throw in the deeper levels. The deep-seated faults are subdivided into three groups (F1 – F3) based on the affected interval (Table 4.1). The fault groups will be described from oldest to youngest below.

Survey name	***Time slice depth TWT (ms)***	***Survey name***	***Time slice depth TWT (ms)***
LN09M01	1600	ST0306	2000
OMV0801	1800	ST05M09	900
OMV09M01	1000	DG0901	1770
LN0901	2200	EN0702	1750
ST8320R00	2000		

Table 4.2: Overview of the depth (TWT) for the variance time slices used in Fig. 4.4a.

4.2.1.1 Third order faults (F3)

Third order faults (F3) are identified mainly in the western and southern part of the Hammerfest Basin (Fig. 4.4b). The lack of seismic data below 1100 ms (TWT) within survey ST05M09 limited the full scale mapping of deep-seated F3 faults, which from a geologic perspective could be interesting. The F3 faults extend from deeper stratigraphic levels and displace the strata in the Lower Cretaceous. The majority of the F3 faults terminate between the upper part of the Kolje Formation and the middle part of the Kolmule Formation. Noteworthy, none of the F3 faults extend through the top Kolmule Formation. The faults appear to have two dominating strike orientations: *NE – SW* and *E – W*.

The *NE – SW* oriented F3 faults are limited to the western Hammerfest Basin, and are observed in the northeastern, western and northern parts of survey LN0901, LN09M01 and ST0306, respectively (Fig. 4.4). One isolated NE – SW striking F3 fault is observed in the southern Hammerfest Basin, close to the Finnmark Platform. The faults are extensional features having dip directions toward the northwest and southeast, forming horst and graben structures (Fig. 4.5ab). In map view the faults appear to consist of

several closely spaced segments between 1.5 and 11 km long. The NE – SW striking F3 faults can be traced from levels deeper than the Upper Jurassic and commonly terminate within the lower part of the Kolmule Formation. The fault throw within the Kolje Formation varies between 10 and 15 ms (TWT), which correspond to 13 – 20 m (TVD) assuming a velocity of 2600 m/s (Table 3.2). Considerably higher throw is observed within the Lower Cretaceous Knurr Formation, varying between 20 and 50 ms (TWT), corresponding to 30 – 75 m (TVD) (V_P = 3000 m/s).

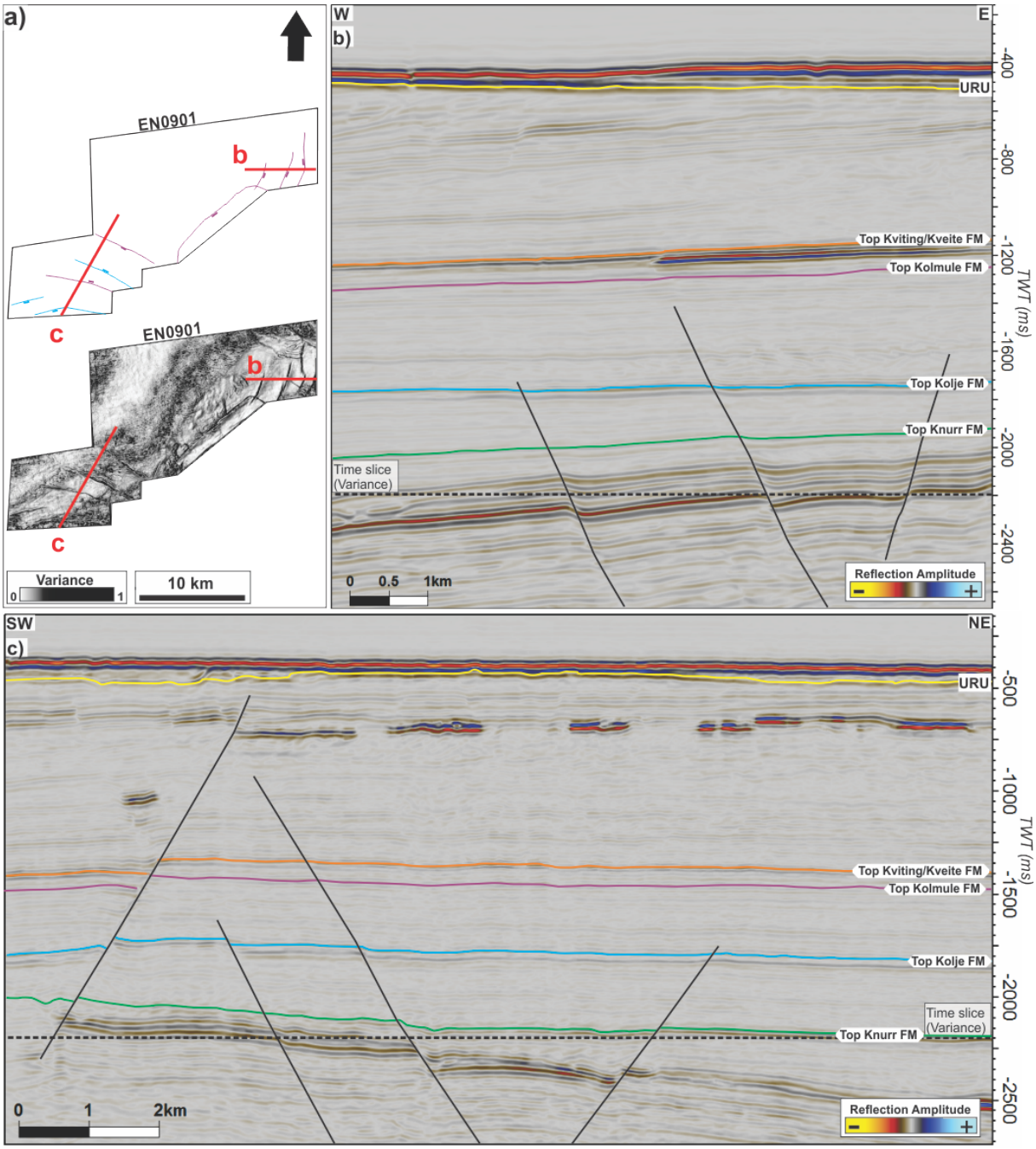

Fig. 4.5: ***a)*** *Overview of survey LN0901, whose position is indicated in Fig. 4.4, showing examples of NE – SW and E – W striking F3 faults (purple), and E – W striking F2 faults (blue). Variance time slice as indicated in* ***b*** *and* ***c*** *(2200 ms TWT).* ***b)*** *Seismic section showing NE – SW striking F3 faults. Position indicated in* ***a****.* ***c)*** *Seismic section showing examples of F2 and F3 faults. Position indicated in* ***a****.*

The *E – W* striking F3 faults occur in the western and southern part of the Hammerfest Basin, and are identifiable in survey LN0901, ST8320R00, ST0306, DG0901 and EN0702 (Fig. 4.4). The majority of the F3 faults are E – W striking. There appears to be a prominent change in the nature of the E – W striking F3 faults, going from west to east. In the west the faults occurs as long continuous segments, each 4 – 13 km long and spaced 2 – 8 km apart, dipping both north and south (Fig. 4.5ac). They generally terminate within the lower part of the Kolmule Formation, with the throw increasing with depth. The vertical displacement within the Kolmule Formation is 10 – 20 ms (TWT) that correspond to 12 – 25 m (TVD) (V_P = 2500 m/s). In the Knurr Formation the throw is 20 – 35 ms (TWT), or 30 – 50 m (TVD) (V_P = 3000 m/s).

Toward the eastern part of the Hammerfest Basin, the E – W striking F3 faults occur as closely spaced segments having a length of 2 – 12 km (Fig. 4.6ab). The segments appear to curve toward south and occasionally having a right-stepping pattern. The majority of the faults reach the lower part of the Kolmule Formation and a few the middle of the Kolje Formation. The fault throw in the Kolmule Formation is 10 – 25 ms (TWT), or 12 – 30 m (TVD) (V_P = 2500 m/s). This increases downwards to 35 – 45 ms (TWT) in the Knurr Formation, or 50 – 70 m (TVD) (V_P = 3000 m/s). The majority of the E – W striking faults, both in the western and eastern region, has a dip direction toward the north. Half-graben geometries occur at the southern margin of the Hammerfest Basin.

4.2.1.2 Second order faults (F2)

The second order faults (F2) refer to the group of deep-seated faults that dominate, in terms of quantity, the study area (Fig. 4.4). They are observed within all seismic datasets and are differentiated from third order faults (F3) as they clearly penetrate younger stratigraphic levels, and terminate within the Paleocene-Eocene Torsk Formation. The F2 faults are inconsistently distributed within the Hammerfest Basin, as they occur most frequently in the western part of the basin. In the east they are most common along the northern and southern margin. All the F2 faults are extensional features and appear to have three dominating directions: *N – S, NE – SW* and *E – W*. Within survey ST05M09 only the most obvious faults are mapped.

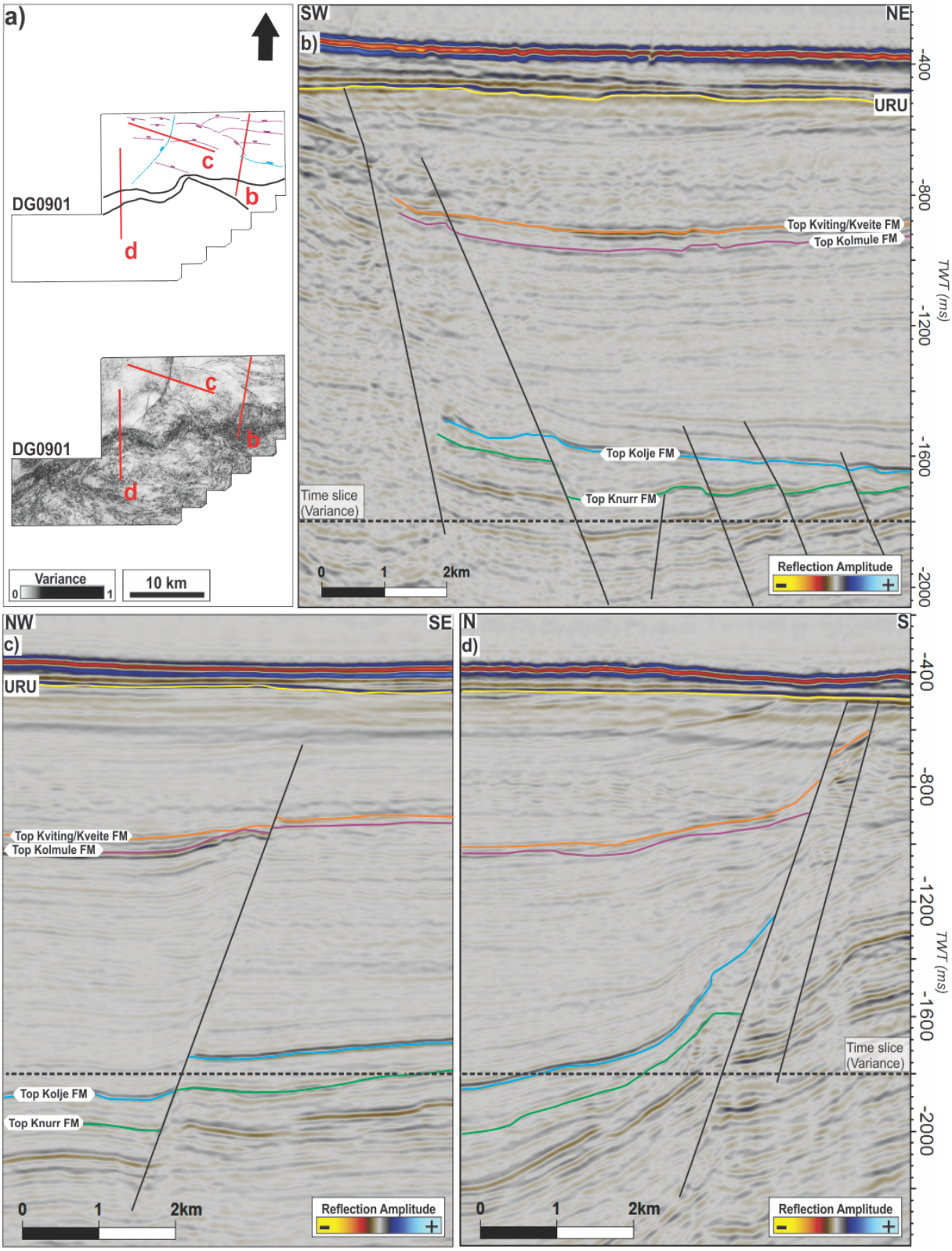

Fig. 4.6: Overview of survey DG0901, whose position is indicated in Fig. 4.4, showing examples of E – W striking F3 faults (purple), N – S striking F2 faults (blue) and E – W striking F1 faults (black). Variance time slice as indicated in ***b-d*** *(1800 ms TWT).* ***b)*** *Seismic section showing E – W striking F1 and F2 and F3 faults. Position indicated in* ***a****.* ***c)*** *Seismic section showing N – S striking F2 fault. Position indicated in* ***a****.* ***d)*** *Seismic section showing E – W striking F1 fault. Position indicated in* ***a****.*

The *N – S* striking F2 faults are observed at three locations within the Hammerfest Basin, in the northwest, southwest and southeast (Fig. 4.4). The F2 faults in the northwestern area occur within the southwestern part of survey LN09M01 and consist of four fault segments, merging into the southwestern corner of the Loppa High (Fig. 4.7ab). The segments are relatively straight and approximately 2 – 8 km long. The easternmost segment dip toward the east, while the three others dip steeply toward the west, showing increased throw westwards (Fig. 4.7b). The westerly dipping faults terminates within the middle to upper part of the Torsk Formation where the displacement is 15 – 30 ms (TWT), or 15 – 30 m (TVD) (V_P = 2000 m/s, Table 3.2). Within the Knurr Formation a significantly higher throw exists in the range of 80 – 230 ms (TWT), or 120 – 345 m (TVD) (V_P = 3000 m/s). A smaller throw is observed for the easterly dipping fault: 10 – 25 ms (TWT), or 10 – 25 m (TVD), in the Torsk Formation, and 25 – 35 ms (TWT), or 37 – 52 m (TVD), in the Knurr Formation.

In the southwestern Hammerfest Basin four N – S striking F2 faults can be identified within survey ST8320R00, dipping west and east (Fig. 4.8ab). The three westerly dipping faults appear to be curving toward the west and have a strike length of 2 – 8 km. The displacement in the Torsk Formation is 25 – 40 ms (TWT), or 25 – 40 m (TVD) (V_P = 2000 m/s), and 120 – 140 ms (TWT), or 180 – 210 m (TVD) (V_P = 3000 m/s), in the Knurr Formation. These are similar throws if compared to the northwestern region. The easterly dipping fault consists of a single straight fault segment, 4 km long, and terminates in the lower part of the Torsk Formation (Fig. 4.8b). Fault throw is 10 ms (TWT), or 10 m (TVD), in the Torsk Formation and 50 ms (TWT), or 75 m (TVD), in the Knurr Formation.

In the southeastern Hammerfest Basin the N – S striking F2 faults occur within survey DG0901 and ST05M09 (Fig. 4.4). In map view the faults emerge from the E – W striking Troms-Finnmark Fault Complex and have a right-stepping nature into survey ST05M09. Each segment is 4 – 7 km long and appears to be curving towards the west (Fig. 4.6ac). All the faults dip westwards and displace the Paleocene-Eocene (Torsk Formation) strata by 15 – 25 ms (TWT), which correspond to 15 – 25 m (TVD) (V_P = 2000 m/s). The Knurr Formation is displaced by 60 ms (TWT), or 90 m (TVD) (V_P = 3000 m/s), within survey DG0901. The deeper displacement within survey ST05M09 is unattainable.

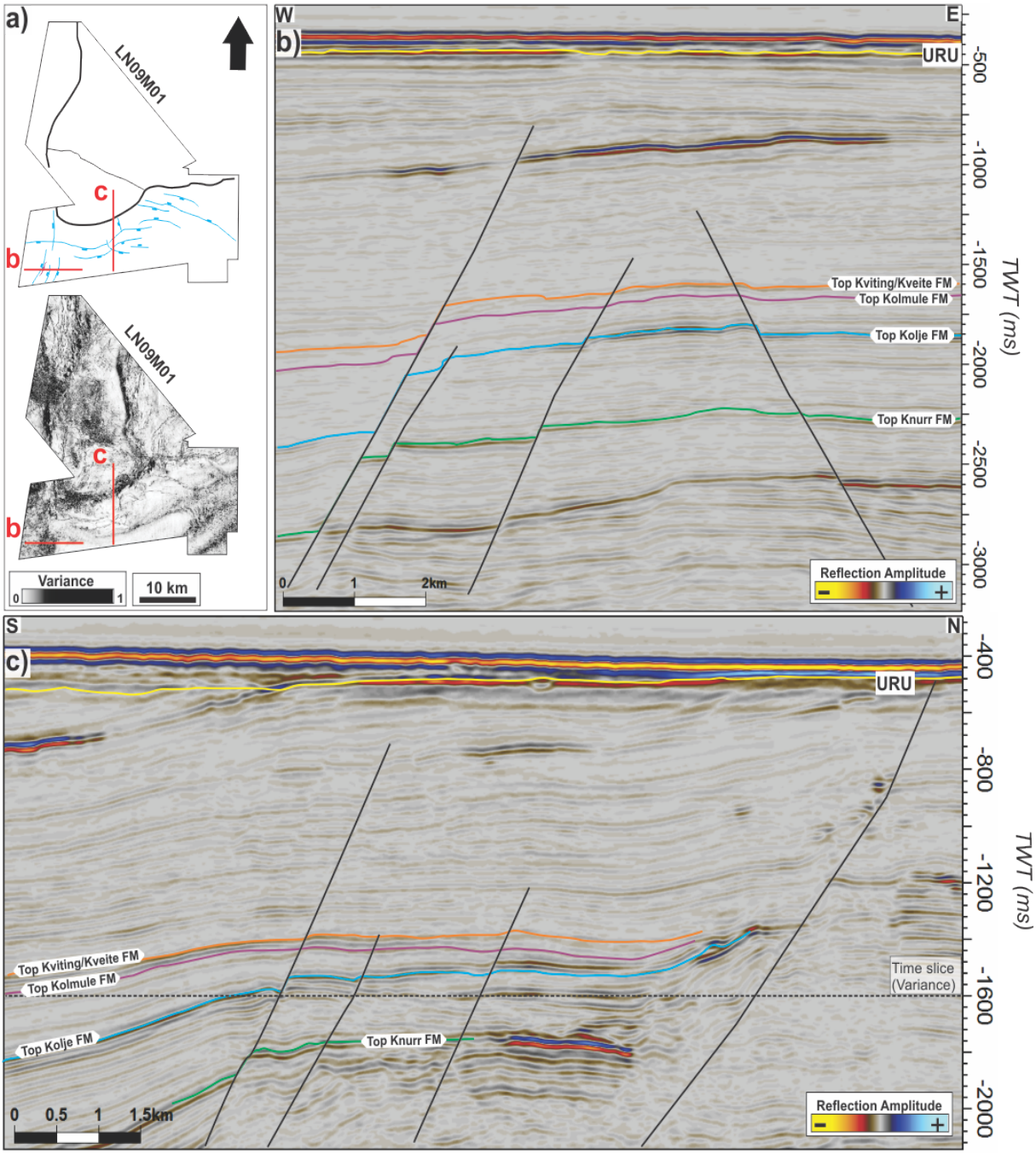

Fig. 4.7: ***a)*** *Overview of survey LN09M01, whose position is indicated in Fig. 4.4, showing examples of N – S and E – W striking F2 faults (blue), and F1 faults (black). Variance time slice as indicated in* ***c*** *(1600 ms TWT).* ***b)*** *Seismic section showing N – S striking F2 faults and a NE – SW striking F3 fault. Position indicated in* ***a****.* ***c)*** *Seismic section showing E – W striking F2 and F1 faults. Position indicated in* ***a****.*

The *NE – SW* striking F2 faults are located within the southwestern and northeastern part of the Hammerfest Basin (Fig. 4.4). In the southwestern area, in the northern part of survey ST8320R00, parallel NE – SW striking F2 faults of opposite dip form a graben structure (Fig. 4.8ac). The faults consists of small segments, each 2 – 9 km long, and appear to cross-cut the N – S striking F2 faults. The two northernmost faults dip toward the southeast and terminate in the lower part of the Torsk Formation, where the

displacement is 15 – 30 ms (TWT), or 15 – 30 m (TVD) (V_P = 2000 m/s). Higher throw is observed in the Knurr Formation where the strata are displaced 40 – 55 ms (TWT), or 60 – 82 m (TVD) (V_P = 3000 m/s). The southernmost fault, dipping northwest, terminates 100 ms (TWT) shallower. The displacement in the Torsk Formation is 20 – 35 ms (TWT), or 20 – 35 m (TVD). Displacement within the Knurr Formation is 45 – 60 ms (TWT), or 67 – 90 m (TVD).

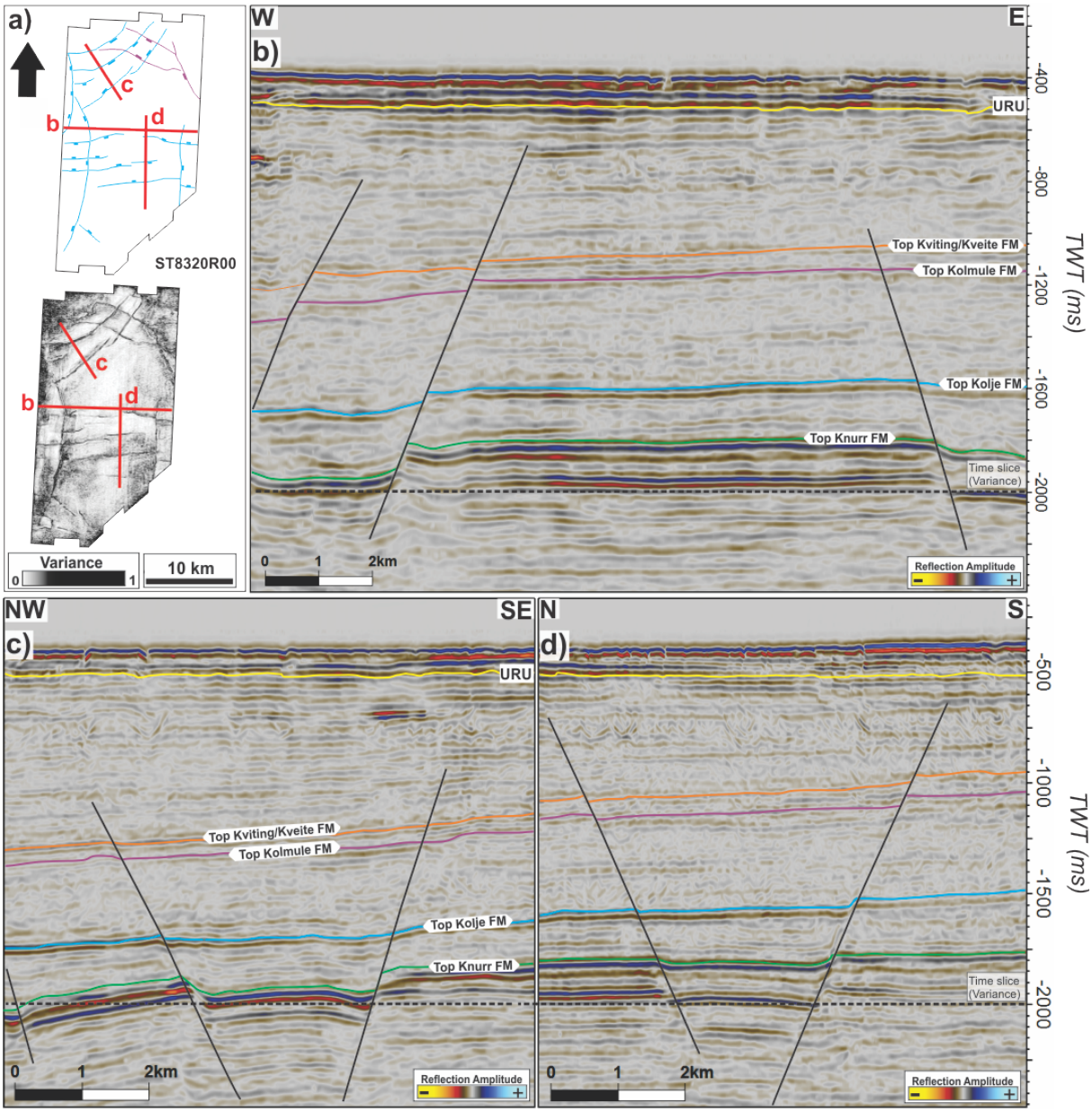

Fig. 4.8: ***a)*** *Overview of survey ST8320R00, whose position is indicated in Fig. 4.4, showing examples of N – S, NE – SW and E – W striking F2 faults (blue). Variance time slice as indicated in* ***b-d*** *(2000 ms TWT).* ***b)*** *Seismic section showing N – S striking F2 faults. Position indicated in* ***a****.* ***c)*** *Seismic section showing NE – SW striking F2 faults. Position indicated in* ***a.*** ***d)*** *Seismic section showing E – W striking F2 faults. Position indicated in* ***a.***

The NE – SW striking F2 faults in the northeastern part of the Hammerfest Basin is located in the northern part of survey OMV09M01 (Fig. 4.4). Faults occur as three continuous segments, 4 – 10 km long, emerging from the E – W trending Asterias Fault Complex and extending westwards out of the dataset. They dip toward the southeast and have a throw of 25 ms (TWT), or 25 m (TVD) (V_P = 2000 m/s), within the Torsk Formation. Displacement within the Knurr Formation is 50 – 70 ms (TWT), or 75 – 105 m (TVD) (V_P = 3000 m/s).

The *E – W* striking F2 faults occur within the western and central part of the Hammerfest Basin (Fig. 4.4). In the northwestern area, within survey LN09M01 and OMV0801, the fault trace appears to be following the contours of the Loppa High, where the fault segments are 7 – 18 km long and curves toward the south (Fig. 4.7ac). The faults dipping toward the south have higher throws than faults dipping north, as they displace the strata in the Torsk Formation by 15 – 40 ms (TWT), or 15 – 40 m (TVD) (V_P = 2000 m/s), and 40 – 60 ms (TWT), or 60 – 90 m (TVD) (V_P = 3000 m/s) in the Knurr Formation. The northerly dipping fault has a throw of 10 – 25 ms (TWT), or 10 – 25 m (TVD), in the Torsk Formation, and 35 – 65 ms (TWT), or 52 – 97 m (TVD) in the Knurr Formation. The westernmost E – W striking F2 fault appears to cross the N – S striking F2 fault, but the strike is not displaced across the fault which indicate that they have been active simultaneously.

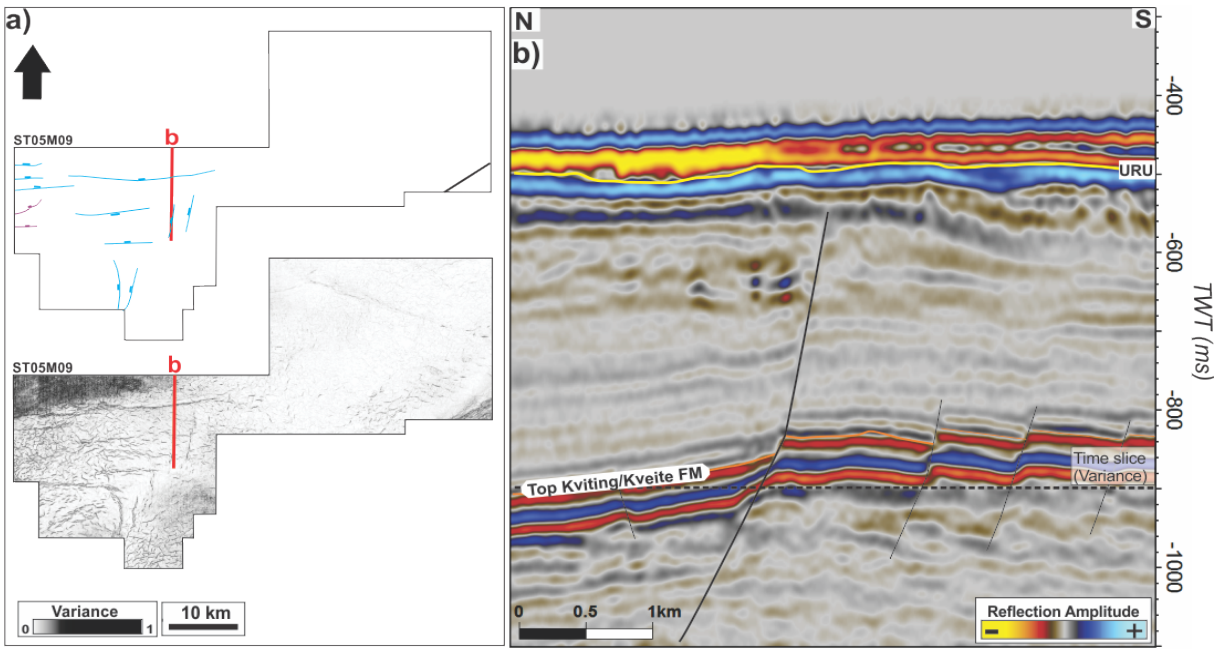

Fig. 4.9: ***a)*** *Overview of survey ST05M09, whose position is indicated in Fig. 4.4, showing examples of E-W striking F3 faults (purple), N-S and E-W striking F2 faults (blue), and F1 fault (black). Time slice as indicated in* ***b*** *(900 ms TWT).* ***b)*** *Seismic section showing a E-W striking F2 fault. Position indicated in* ***a****.*

Southwards along western margin of the Hammerfest Basin, the E – W striking F2 faults occur more frequently (Fig. 4.4). Within survey LN0901, ST8320R00 and ST0306, the faults have opposite dip and form horst and graben structures (Fig. 4.8ad). They cross N – S striking F2 faults without being displaced along strike. In map view the faults appear as 4 – 15 km long continuous segments, terminating in the middle to upper part of the Torsk Formation. The fault throw increases with depth, where the Torsk Formation is displaced 10 – 25 ms (TWT), or 10 – 25 m (TVD) (V_P = 2000 m/s), and the Knurr Formation 35 – 55 ms (TWT), or 52 – 82 m (TVD) (V_P = 3000 m/s).

Eastwards within the Hammerfest Basin and into survey ST05M09, only six E – W striking F2 faults occur (Fig. 4.4). The frequency of faulting is significantly less than in the rest of the basin. The fault segments show a length of 7 – 12 km long and appear to dip both north and south (Fig. 4.9). The faults terminate only 70 ms (TWT) below URU. The strata within the Torsk Formation is displaced by 15 – 20 ms (TWT), or 15 – 20 m (TVD) (V_P = 2000 m/s). Displacement within the Knurr Formation is unattainable.

4.2.1.3 First order faults (F1)

First order faults (F1) are limited to the northwestern, northeastern and southeastern margin of the Hammerfest Basin (Fig. 4.4). The F1 faults can be distinguished from the second order faults (F2) as they reach the URU and occasionally even cross the unconformity. Commonly the faults occur as single continuous segments that separate the Hammerfest Basin from other structural features. In map view the fault measure 37 km long horizontally and have a vertical throw in the range of 90 – 330 ms (TWT), or 117 – 429 m (TVD) (V_P = 2600 m/s, Table 3.2), within the Torsk Formation. Displacement in the deeper levels is not obtainable.

In the northeast the F1 faults are observed in the northern part of survey OMV09M01 (Fig. 4.4). Similar to the northwestern margin, these faults are part of the Asterias Fault Complex, and occur as five E – W striking segments. Faults dipping both north and south appear to cross the URU, as evidenced by a series of time changes on the interpreted URU reflection (Fig. 4.10). The displacement of the URU is only minimal and in the range of 10 – 15 ms (TWT), or 8 – 12 m (TVD) (V_P = 1700 m/s). The Torsk Formation is displaced by 10 – 15 ms (TWT), or 10 – 15 m (TVD) (V_P = 2000 m/s), and the deeper formations by 25 – 55 ms (TWT), or 40 – 88 m (TVD) (V_P = 3200 m/s).

In the southeastern Hammerfest Basin the F1 faults are crossing survey DG0901, LN0702 and in the southeastern corner of survey ST05M09 (Fig. 4.4), They occur as a single or two parallel segments striking E – W to NE – SW (Fig. 4.6d). The faults dip toward the north forming half-graben structures. The fault throw is 80 – 110 ms (TWT), or 104 – 143 m (TVD) (V_P = 2600m/s), within the Torsk Formation. Throw at deeper levels is not obtainable. Occasionally the faults appear to cross the URU, although there is a high degree of uncertainty.

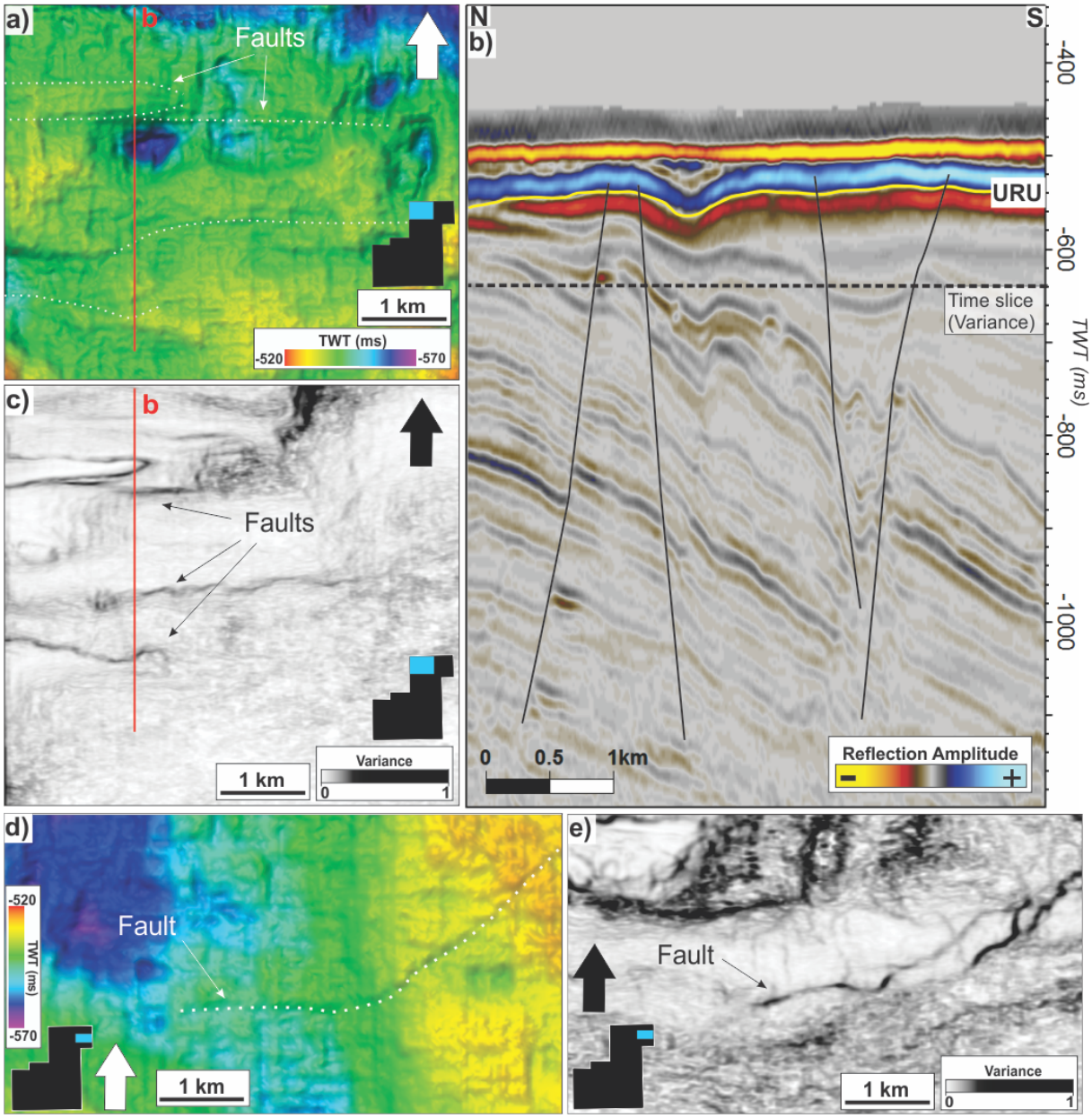

Fig. 4.10: ***a, c, d*** *and* ***e*** *is located in northern part of survey OMV09M01, whose location is indicated in Fig. 4.4.* ***a*** *and* ***d*** *show part of the interpreted URU reflection where a series of deep-seated faults (F1) has formed time changes on the surface.* ***b)*** *Seismic section showing E – W striking F1 faults penetrating the URU. Position of section indicated in* ***a*** *and* ***c****.* ***c & e)*** *Variance time slice as indicated in* ***b*** *(640 ms TWT).*

4.2.2 Shallow faults

Fault interpretations along variance time slices within the Torsk Formation revealed numerous shallow faults in the western and southeastern part of the Hammerfest Basin. The faults are extensional features and commonly occur within the upper part of the Paleocene-Eocene Torsk Formation. All shallow faults appear to be terminating at or just below the URU. The distribution and density of faults within the study area may be influenced and limited by the seismic resolution of each individual dataset. No shallow faults have been identified within survey ST8320R00, OMV09M01 and ST05M09. The faults are commonly striking NW – SE, N – S, NE – SW and E – W.

In the northwestern area, shallow faults have been identified within survey LN09M01, LN0901 and OMV0801 (Fig. 4.11a). Close to the southwestern corner of the Loppa High, the majority of the shallow faults are oriented E – W to NW – SE. The faults mainly dip toward the west – southwest and appear to consist of small segments having a curvilinear shape. Each segment measure 1 – 6 km long horizontally and have a vertical throw of 5 – 15 ms (TWT), or 5- 15 m (TVD) (V_P = 2000 m/s, Table 3.2). The faults are confined to the upper part of the Torsk Formation, although some can reach the lower part of the formation (Fig. 4.11b).

Southwards along the western margin, into survey LN0901 and ST0306, there is a significantly increase in the number of identified shallow faults (Fig. 4.11a). The faults appear to be striking N – S, NE – SW and E – W, and consist of relatively linear segments. The segments are generally shorter (0.2 – 4 km) than in the northwestern area, and have no preferred dip direction. The fault throw is in the range of 5 – 15 ms (TWT), or 5 – 15 m (TVD) (V_P = 2000 m/s), and the majority are confined to the upper part of the Torsk Formation (Fig. 4.11c). No differences are observed between the various strike directions in relation to the fault throw.

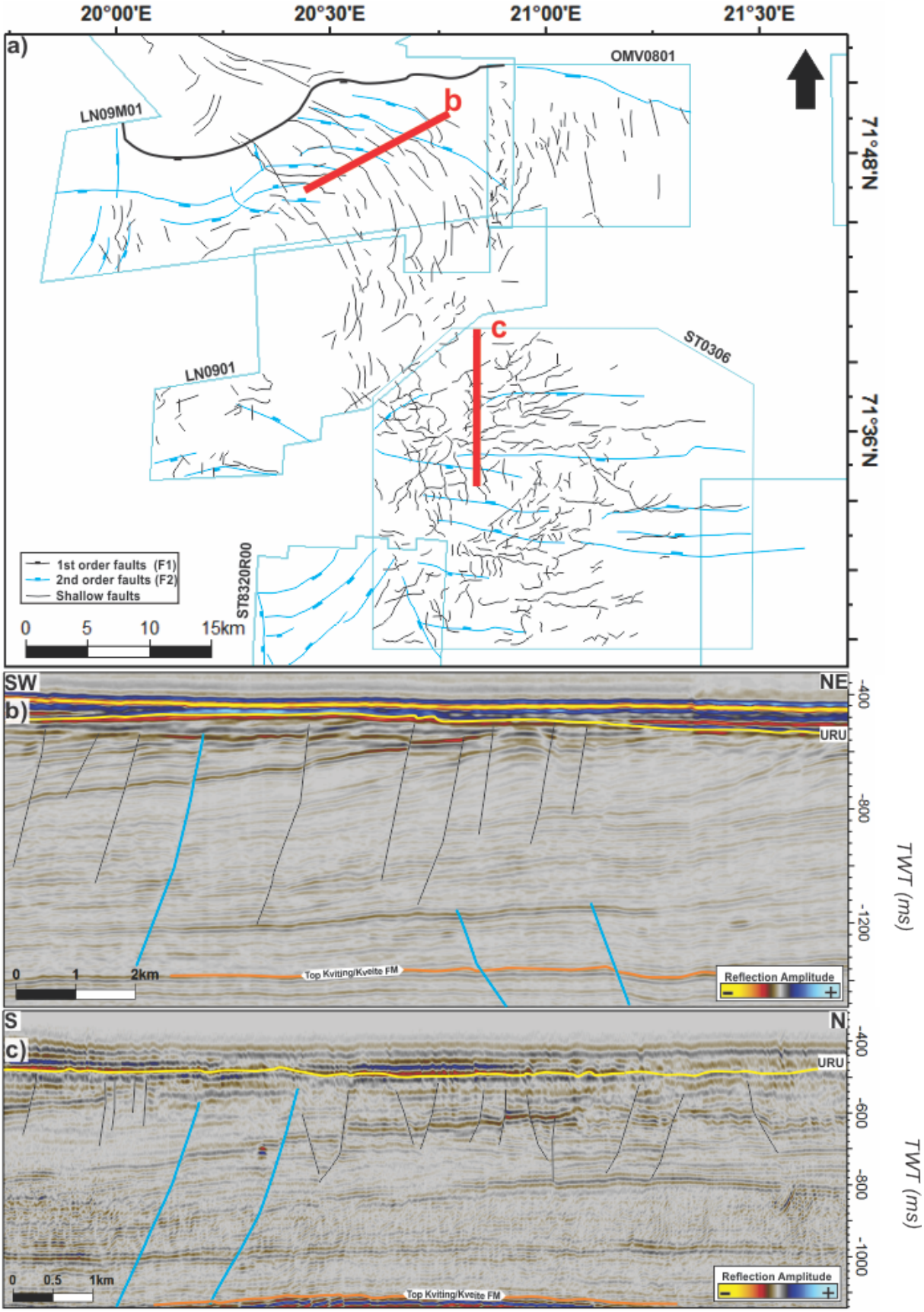

Fig. 4.11: ***a)*** *Overview of shallow faults and F1-F2 faults within survey LN09M01, OM0801, LN0901and ST0306. Shallow faults are mapped using variance time slices at various depths.* ***b)*** *Seismic section (LN09M01) showing shallow faults and E – W striking F2 faults. Position indicated in* ***a****.* ***c)*** *Seismic section (ST0306) showing shallow faults and E – W striking F2 faults. Position indicated in* ***a****.*

In the southeastern part of the Hammerfest Basin, the shallow faults identified concentrate within the northern and southwestern part of survey DG0901 and EN0702, respectively (Fig. 4.12a). The faults appear to be striking N – S and E – W and consist of small segments that are 0.5 – 3 km long. The segments have a curvilinear to linear shape and have a preferred dip direction toward west – northwest. The faults are confined to the upper part of the Torsk Formation and no faults appear to reach the Kviting/Kveite Formation (Fig. 4.12b). The throw of the shallow faults is in the range of 5 – 15 ms (TWT), or 5 - 15 m (TVD) (V_P =2000 m/s).

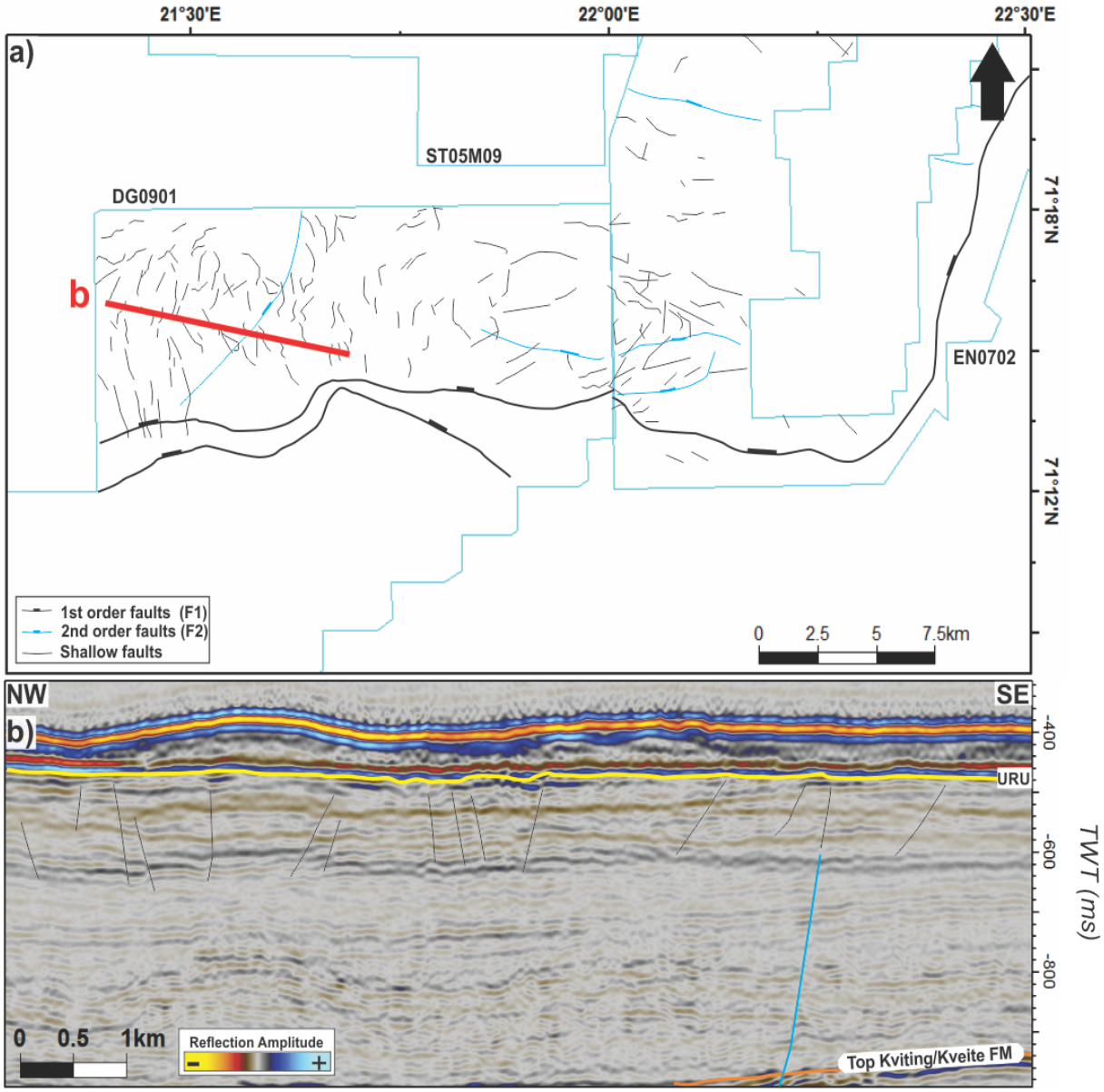

Fig. 4.12: ***a)*** *Overview of shallow faults and F1-F2 faults within survey DG0901 and EN0702. Shallow faults have been mapped using variance time slices at various depths.* ***b)*** *Seismic section showing shallow faults and N – S striking F2 fault. Position indicated in* ***a****.*

4.3 Fluid flow features

In the northwestern part of the Hammerfest Basin, in survey LN09M01, LN0901 and ST0306, the seismic data reveal seven zones (C1 – C7) where severe acoustic masking occurs (Fig. 4.13) (Table 4.3). The zones are characterized by having distorted seismic reflections with low amplitude and low coherency. They extend through several stratigraphic units and terminates in the middle to upper part of the Torsk Formation. The features are very similar to acoustic chimneys (e.g. Meldahl et al., 2001; Ligtenberg, 2005; Arntsen et al., 2007; Løseth et al., 2009). Noteworthy, bright spots occur at the upper termination of all acoustic chimneys

On the southwestern Loppa High, four (C1 – C4) acoustic chimneys are identified (Fig. 4.13ab). The largest of these (C1) are located above the high itself, and in plan view it has an elongated shape with the longest axis striking NW – SE. It covers an area of approximately 18 km^2 where the long and short axis measure 8.4 and 2.4 km, respectively. The top of the chimney, characterized by high amplitudes (bright spots), is located at approximately 640 ms (TWT) (Fig. 4.13b), within the upper part of the Torsk Formation. The chimney structure is most prominent down to 1800 ms, although low amplitude reflections also occur below this level (Fig. 4.13b) (TWT).

Three acoustic chimneys (C2 – C4) are located directly above the F1 fault separating the Loppa High from the Hammerfest Basin (Fig. 4.13ab). The chimneys have an oval shape with the long axis striking approximately E – W, and cover an area of 2.3 – 8.6 km^2. The upper termination of the chimneys occurs at 780 – 890 ms (TWT), in the middle of the Torsk Formation, and they are most prominent down to 2000 – 2300 ms (TWT), below the Base Cretaceous (Fig. 4.13b). Pull-down of the seismic reflections are observed in the deeper parts of the zone of acoustic masking. Stacked bright spots are observed above the chimneys, although the amplitudes are not as high as those above C1 (Fig. 4.13).

Two acoustic chimneys are identified in the northeastern (C5) and northwestern (C6) part of survey ST0306 (Fig. 4.13ac). They have an elongated shape where the long axis strikes NE – SW. C5 covers an area of 22.7 km^2, where the long and short axis measures 8.6 and 1.8 km, respectively. C6 covers an area more than twice than that of C5, 57 km^2,

and have a long and short axis of 14.1 and 3 km, respectively. The distorted seismic signal of both C5 and C6 terminates in the middle of the Torsk Formation and are most prominent down to the Hekkingen Formation, at 2000 – 2100 ms (TWT), although masking of the reflections also occur below this level. The reflections of the Kviting/Kveite, Kolmule and Kolje formations are totally wiped out, while a pull-down is observed in the reflections corresponding to the Top Knurr and Top Hekkingen formation, directly beneath the zone of acoustic masking (Fig. 4.13c). The top of the chimneys are characterized by a series of bright spots, covering a larger area than the chimneys themselves. Deep-seated E – W striking F2 faults are observed underneath the zone of acoustic masking, however they does not appear to control the shape of the chimneys.

C7, within the southwestern part of survey LN0901 (Fig. 4.13), share the same characteristics as C5 and C6 in terms of the vertical extent. The upper termination is within the centre of the Torsk Formation at 970 ms (TWT), where two bright spots are located above each other. The acoustic masking extends down to 2060 ms (TWT), below the Upper Jurassic Hekkingen Formation. In plan view the chimney has an oval shape with the long axis striking E – W, and have a long and short axis of 2.4 and 1.2 km, respectively. An E – W striking F2 fault is located in proximity to this acoustic chimney (Fig. 4.13).

Chimney	***Long axis (m)***	***Short axis (m)***	***Area (km²)***	***Top TWT (ms)***	***Base TWT (ms)***
C1	8430	2420	18.3	640	1800
C2	1805	1325	4.5	890	2210
C3	1268	941	8.6	780	2000
C4	4670	2305	2.3	790	2300
C5	8612	1847	22.7	740	2100
C6	14124	3047	57	780	2000
C7	2440	1258	2.7	970	2060

Table 4.3: Summary of the acoustic chimney structures (C1 – C7). The top is defined as the depth where the acoustic masking terminates into or enters an amplitude anomaly.

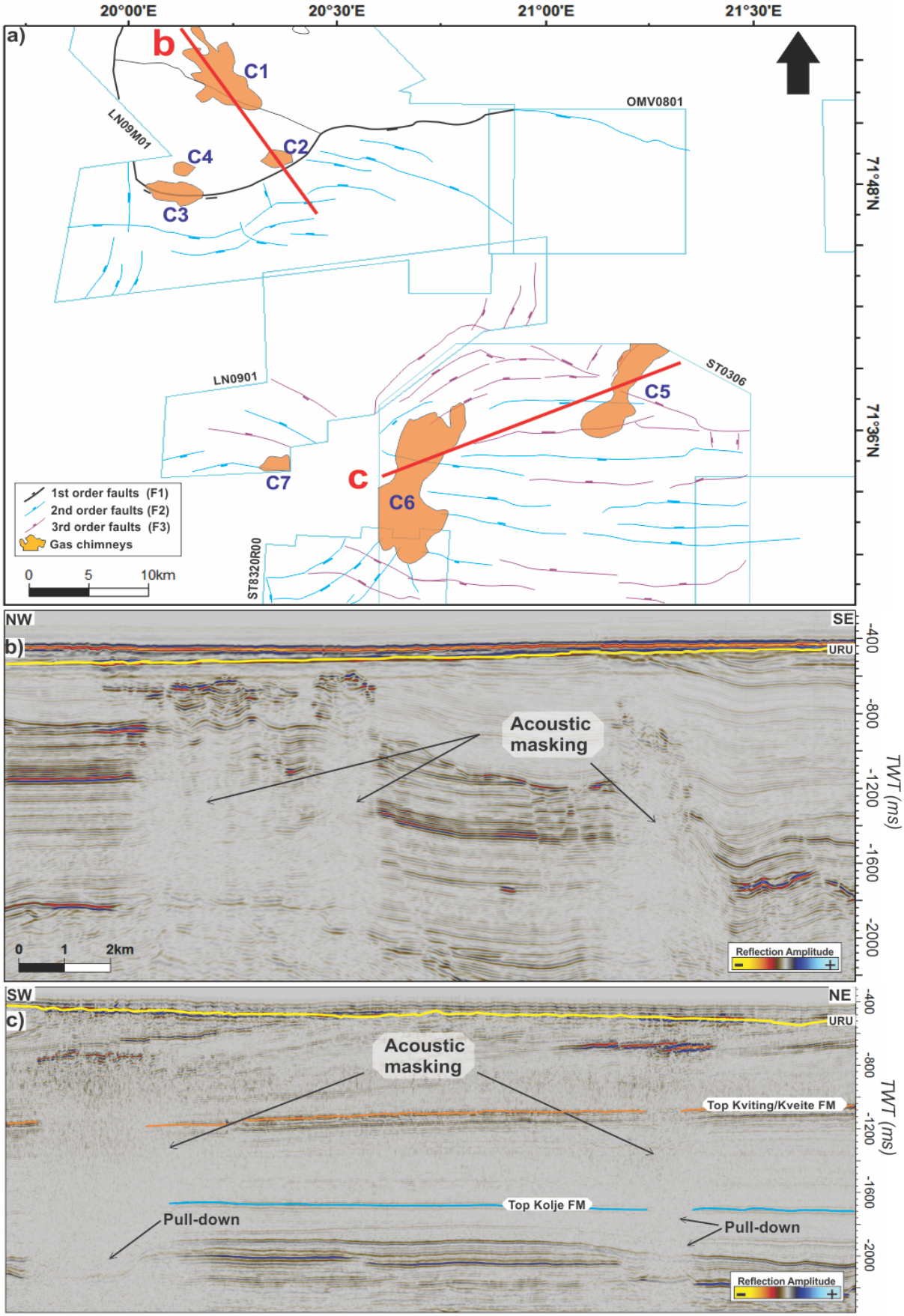

Fig. 4.13: ***a)*** *Overview map of acoustic chimneys in the northwestern Hammerfest Basin. They are observed in survey LN09M01, LN0901, ST8320R00 and ST0306. Pull-down of seismic reflections is observed in the deeper areas, below the most prominent zone of acoustic masking.*

4.4 Amplitude anomalies

Numerous high amplitude anomalies are observed within the study area and occur at several stratigraphic levels. The focus has been on the amplitude anomalies located above the Base Cretaceous, hence deeper anomalies are excluded from this study. The amplitude anomalies are divided into two groups:

- Amplitudes anomalies below the URU (A1 – A10) (Fig. 4.14) (Table 4.4).
- Amplitudes along the URU (Fig. 4.24).

Based on the location and stratigraphic level, a selection of amplitudes from each group is picked for a detailed and thorough description based on attribute maps and seismic cross-sections.

4.4.1 Amplitude anomalies below the URU

Below the upper regional unconformity ten (A1 – A10) sets of amplitude anomalies can be identified within the Hammerfest Basin and will be described in the following subchapters (Fig. 4.14). Each group of amplitude anomalies consist of one single high amplitude reflection or a collection of several smaller high amplitude reflections. The majority of the amplitude anomalies are located in the middle to upper part of the Torsk Formation, although they on two occasions occur within the Kviting/Kveite Formation. The anomalies are generally characterized with anomalous high amplitudes where the reflections have reversed polarity compared to the seabed reflection. Acoustic masking and pull-down of underlying reflections are frequently observed below the amplitude anomalies. The acoustic chimneys (described above) are observed directly beneath a few of the anomalies. Two amplitude anomalies occur above and west of the Loppa High and will not be included in this study as they are located outside the study area of interest.

4.4.1.1 Seismic amplitude anomaly 1 (A1)

Seismic amplitude anomaly 1 is located in the southwestern part of survey LN09M01 in the northwestern Hammerfest Basin (Fig. 4.14 and Fig. 4.15). The amplitude anomaly occur in the upper part of the Torsk Formation between 600 and 690 ms (TWT), and

covers an area of 28.6 km^2. It is located approximately 25 ms (TWT) below the URU. In map view A1 has an meandering shape with an overall NW – SE orientation (Fig. 4.15a). In seismic section the strong reflection is charactericed by a reversed polarity compared to the seabed reflection, and is dipping toward the south-southwest with clinoforms in the same direction (bright spot) (Fig. 4.15b). A deep-seated, E – W striking F2 fault appear to be affecting the edge of the anomaly down-to-southwest. Below A1 there is a thick zone of acoustic masking, reducing the horizontal continuity of the adjacent reflections, extending from Jurassic levels. A pull-down is observed in the zone below the zone of acoustic masking (Fig. 4.15b).

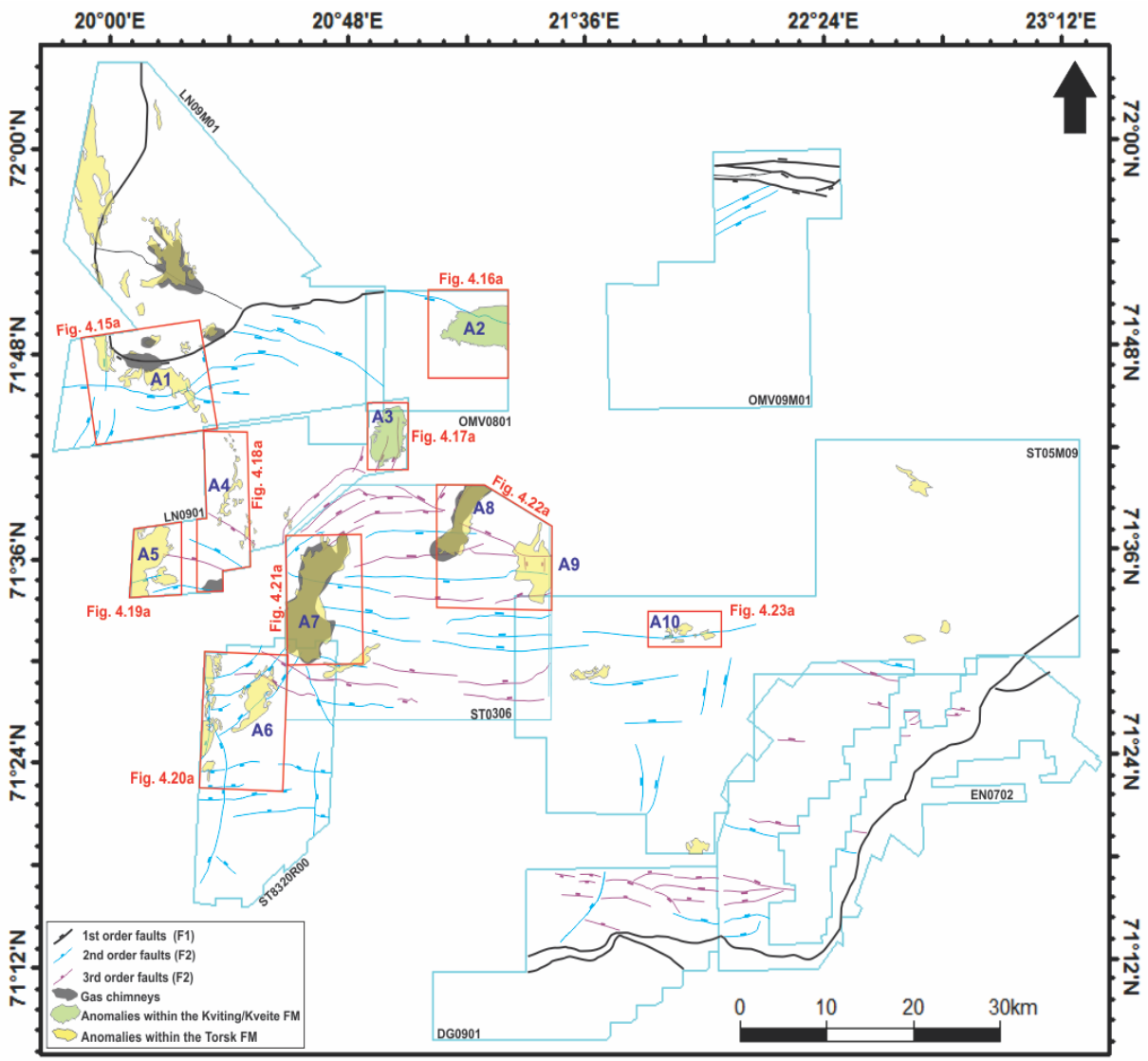

Fig. 4.14: Overview of amplitude anomalies (A1 – A10) within the study area, southwestern Barents Sea. Deep-seated F1, F2 and F3 faults in addition to acoustic/gas chimneys are included in the overview. Amplitude anomalies located above and west of the Loppa High are not included in this study. The red polygons shows the position of other figures describing the area.

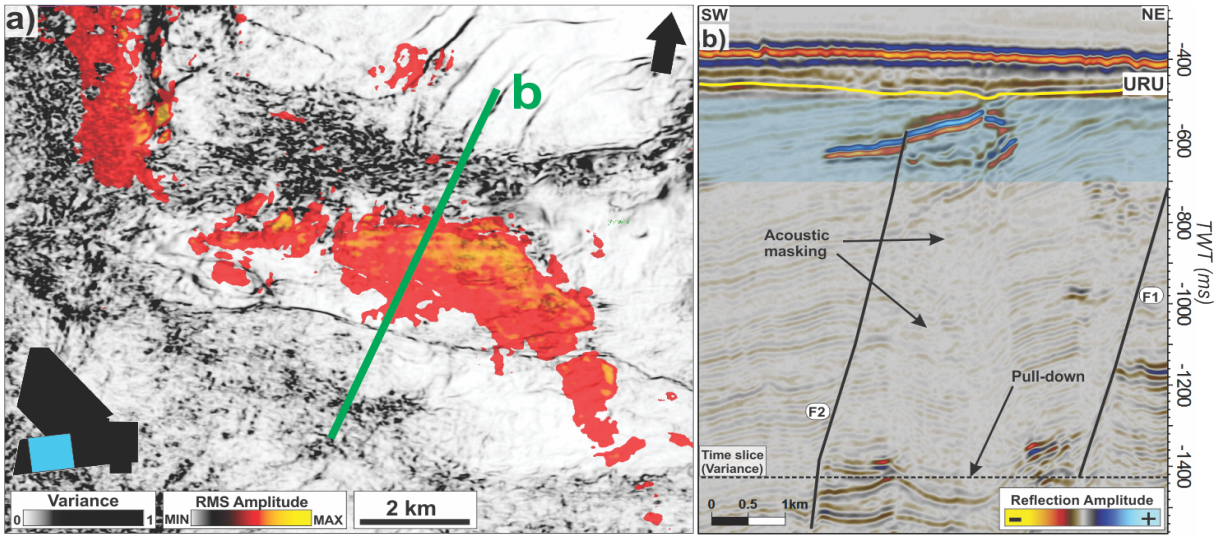

Fig. 4.15: ***a)*** *Overview of RMS amplitude anomaly A1 above variance time slice (1450 ms TWT). RMS amplitudes extracted from 200 ms (TWT) interval as indicated (blue shaded zone in in* ***b****). Position of map indicated within black polygon (survey LN09M01) in lower left corner, whose location is shown in Fig. 4.14.* ***b)*** *Seismic section through A1. Position indicated in* ***a****. A zone of acoustic masking occur below the anomaly, where a pull-down characterizes the deepest reflections.*

4.4.1.2 Seismic amplitude anomaly 2 (A2)

Seismic amplitude anomaly 2 is located in the northeastern part of survey OMV0801 (Fig. 4.14 and Fig. 4.16a). The anomaly occur within the upper part of the Kviting/Kveite Formation and is dipping incrementally toward the west. The reflection appear to have reversed polarity compared to the seabed reflection. A2 appear to have an oval shape where the longest axis is oriented E – W, and covers an area of 31.7 km^2 (Fig. 4.16a). It is located between 1060 and 1300 (TWT). The eastern margin of A2 is not covered by the dataset and probably extends to shallower levels. An E – W striking deep-seated F2 fault extends from Jurassic levels and penetrates the anomaly (Fig. 4.16b). Noteworthy, no signs of acoustic masking is observed below A2.

4.4.1.3 Seismic amplitude anomaly 3 (A3)

Amplitude anomaly 3 is located in the northeastern part of survey LN0901 (Fig. 4.14 and Fig. 4.17) within the upper part of the Kviting/Kveite Formation. It occurs between 1170 and 1250 ms (TWT), covers an area of 17.5 km^2 and is dipping westwards. The anomaly has an oval shape with the longest axis striking NE – SW, and appear to have reversed polarity compared to the seabed reflection. Three NE – SW striking deep-seated F3 faults are identified below A3 (Fig. 4.17). One of the faults terminates within the Kolje Formation while the two other terminates within the lower part of the Kolmule Formation. No signs of acoustic masking or pipe structures are observed below or above A3 (Fig. 4.17b).

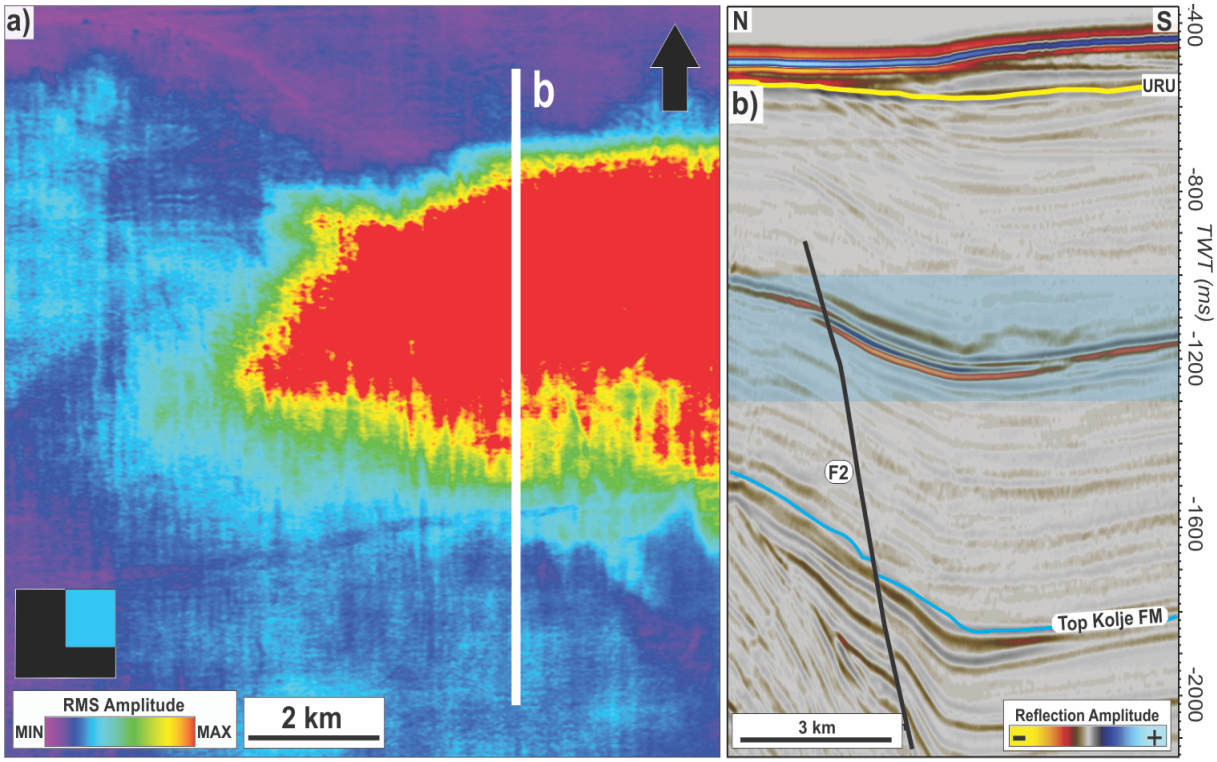

Fig. 4.16: ***a)*** *RMS amplitude map of amplitude anomaly A2. RMS amplitudes extracted from 200 ms (TWT) interval as indicated in* ***b*** *(blue shaded zone). Position of map indicated in black polygon (survey OMV0801) in lower left corner, whose location is indicated in Fig. 4.14.* ***b)*** *Seismic section through A2. Position indicated in* ***a****. A E – W striking F2 fault penetrates the amplitude anomaly.*

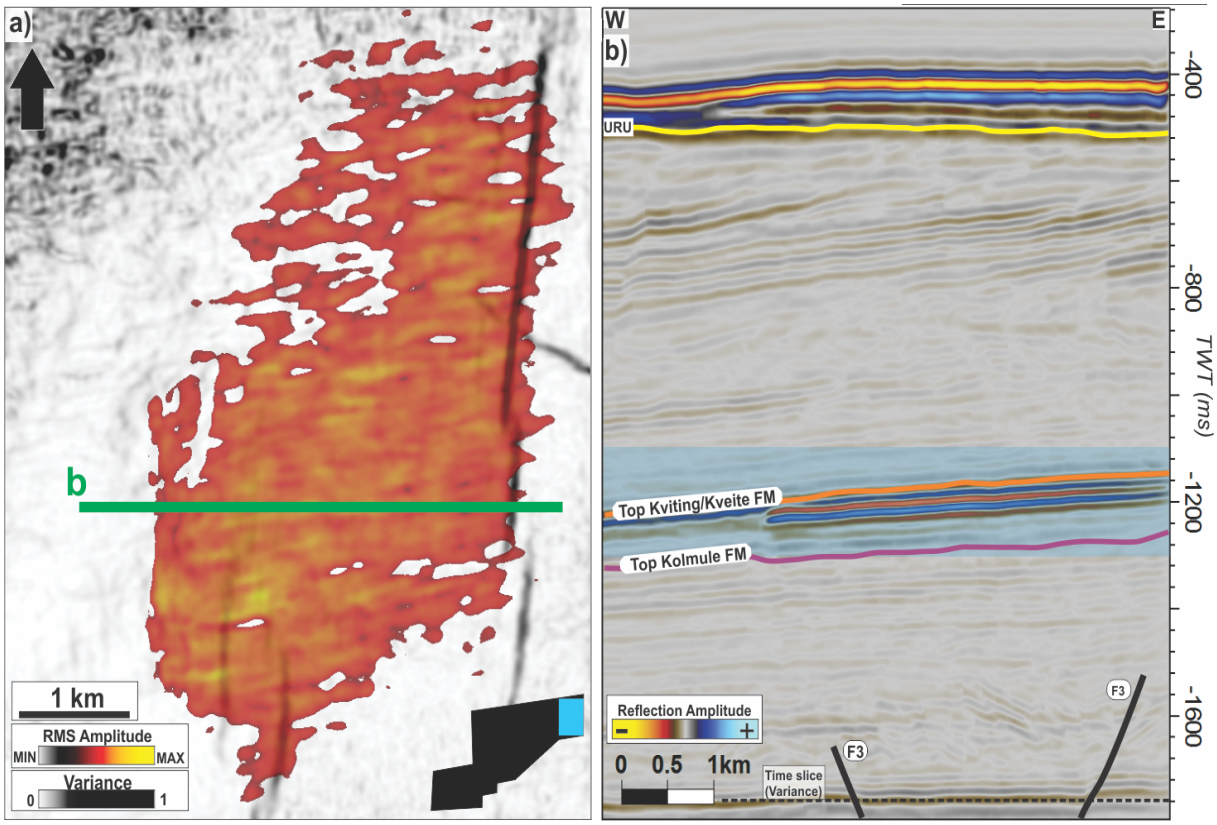

Fig. 4.17: ***a)*** *Overview of RMS amplitude anomaly A3 above a variance time slice (1760 ms TWT). RMS amplitudes extracted from 200 ms (TWT) interval as indicated (blue shaded zone in* ***b****). Position of map indicated within black polygon (survey LN0901) in lower left corner, whose location is shown in Fig. 4.14.* ***b)*** *Seismic section through A3. Position of section indicated in* ***a****. Two NE – SW striking F3 faults terminated within the Kolmule Formation below.*

4.4.1.4 Seismic amplitude anomaly 4 (A4)

Seismic amplitude anomaly 4 is located in survey LN0901 and is extending from the southern to the northern edge of the dataset (Fig. 4.14 and Fig. 4.18). The anomaly has a meandering shape with an overall NE – SW orientation, and in map view the amplitude anomaly appear to be the southern continuation of A1. The anomaly is 4.3 km wide in the southern part and thins to 1 km northward. The length is 17.4 km and in total it covers an area of 21.2 km^2 (Fig. 4.18a). A4 is characterized with a reversed polarity compared to the seabed reflection and appears to be a relatively flat event that to some degree mimics the seabed, cross-cutting the westerly dipping strata (Fig. 4.18c). The anomaly is located within the upper part of the Torsk Formation between 630 ms and 740 ms (TWT), about 470 ms (TWT) below the URU. The seismic reflections above and adjacent to the anomaly do not appear to be influenced, as they have high continuity and relatively strong amplitudes. The URU reflection does not show anomalous amplitudes directly above A4. Directly beneath the anomaly a vertical zone of acoustic masking is observed, extending to below the Kolmule Formation (Fig. 4.18bc). Four E – W striking deep-seated F2 faults are identified below A4. Two of the faults (F2) reach the Torsk Formation, where only the southernmost fault reaches the anomaly. This fault appears to be displacing the southern tip of A4 to a shallower level (up 20 ms (TWT)), toward north, although the same fault in the deeper levels clearly have a throw toward the south-southwest (Fig. 4.18b). The southernmost fault appears to be affecting the shape of A4, however it does not control the lateral extent of the high amplitudes. Acoustic masking is observed along the fault plane.

4.4.1.5 Seismic amplitude anomaly 5 (A5)

Seismic amplitude anomaly 5 is located in the southwestern part of survey LN0901, approximately 190 ms (TWT) deeper and 4.3 km west of amplitude anomaly 4 (Fig. 4.14 and Fig. 4.19). The anomalous reflection is situated in the middle of the Torsk Formation at 820 – 960 ms (TWT) (Fig. 4.19b), and show reversed polarity compared to the seabed reflection. In map view A5 consists of two patches spaced 1.5 km apart, one large in the northwest and one small in the southeast (Fig. 4.19a). The large patch pinches out eastwards and covers an area of 19.1 km^2, however it is likely that it exceed this number as it extends westward beyond the coverage of the dataset. The small patch has an oval shape and covers an area of approximately 2.7 km^2. The longest axis measure 2 km and is striking E – W, while the short axis measure approximately 1 km. In general the

amplitude anomaly appears to be a sub-horizontal event that is crosscutting the west - southwesterly dipping strata. Above A5 there is a zone where the horizontal continuity of the reflections is low compared to the surroundings, although the continuity is increasing toward URU. Acoustic masking is observed directly beneath A5 and extends approximately 100 ms (TWT) downwards. Two E – W striking F2 faults is identified in the deeper levels and extend through A5, where the termination occur in the upper part of the Torsk Formation (Fig. 4.19b). The southern limit of the northern anomaly patch appears to be controlled by the westerly dipping faults. The shape of the southern patch is not affected. In seismic section acoustic masking is observed along the fault plane and occasionally enhanced reflections occur in adjacent strata.

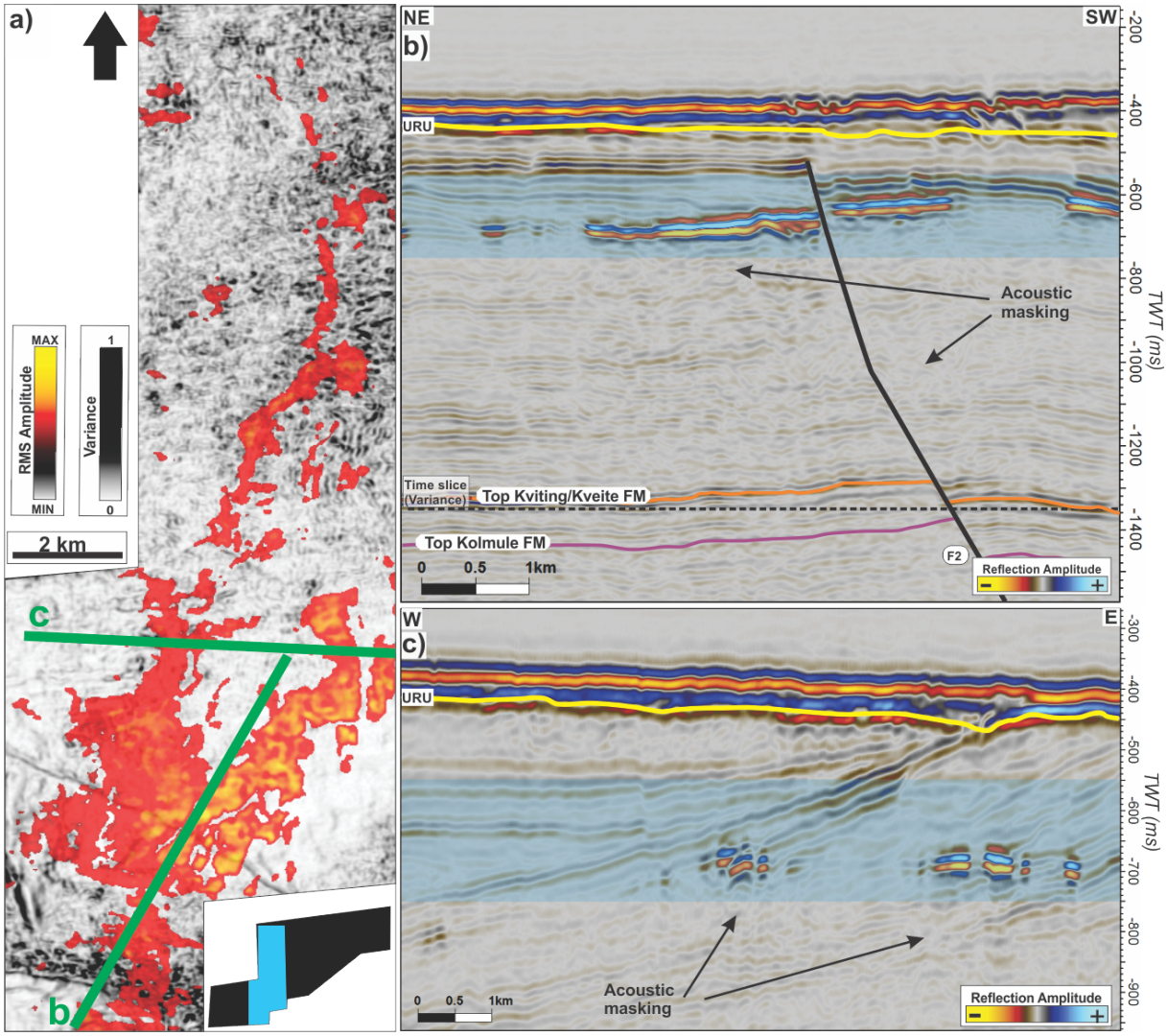

Fig. 4.18: ***a)*** *RMS amplitude map of amplitude anomaly A4 above variance time slice (1350 ms (TWT)). RMS amplitudes extracted from 200 ms (TWT) interval as indicated in* ***b*** *&* ***c*** *(blue shaded zone). Position of map indicated in the black polygon (survey LN0901) in the lower right corner, whose position is indicated in Fig. 4.14.* ***b)*** *NE – SW oriented seismic section through A4. Position indicated in* ***a****. Deep-seated E – W striking F2 faults reach and penetrates the amplitude anomaly. Acoustic masking is observed along the fault plane and below A4.* ***c)*** *E – W oriented seismic section through A4. Position indicated in* ***a****. The amplitude anomaly cross-cut the westerly dipping strata and have acoustic masking underneath.*

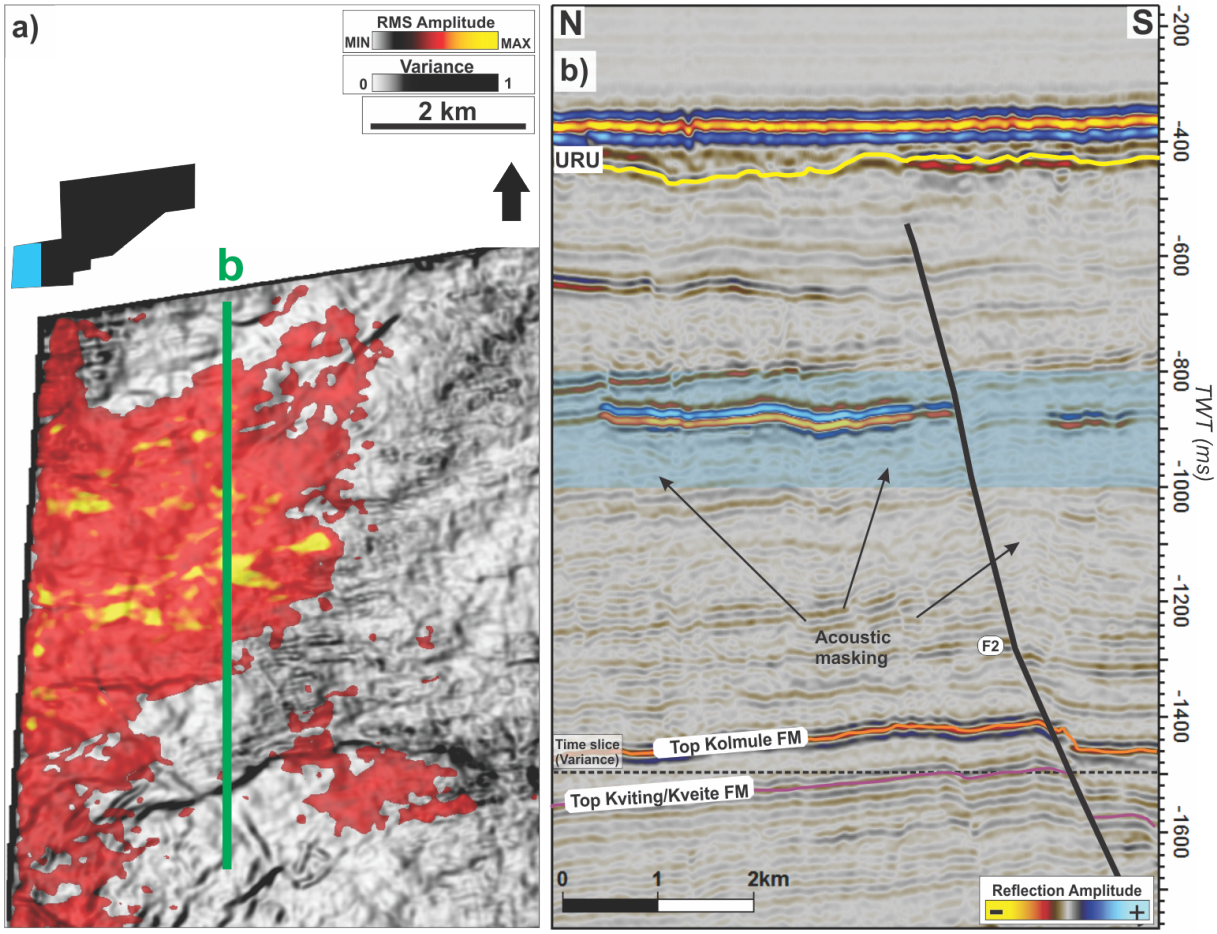

Fig. 4.19: ***a)*** *RMS amplitude map of amplitude anomaly A5 above variance time slice (1400 ms (TWT)). RMS amplitudes extracted from 200 ms (TWT) interval as indicated in* ***b****. Position of map is indicated in black polygon (survey LN0901) in the upper left corner, whose location is indicated in Fig. 4.14.* ***b)*** *Seismic section through A5 together showing an E – W striking F2 fault that penetrates the anomaly. Acoustic masking is observed below the anomaly and along the fault plane. Position of section indicated in* ***a****.*

4.4.1.6 Seismic amplitude anomaly 6 (A6)

Seismic amplitude anomaly 6 is located in the northwestern part of survey ST8320R00 (Fig. 4.14 and Fig. 4.20). A6 consists of a western and eastern set of high amplitudes spaced 2.8 km apart (Fig. 4.20a). The anomaly is located in the upper part of the Torsk Formation between 600 and 730 ms (TWT) and has a flat top and base (Fig. 4.20bc). Both the western and eastern set have an elongated to oval shape. The western set covers an area of 16.8 km^2, where the longest and shortest axis measures 14.1 km and 1.1 km, respectively. The long axis is striking N – S, and the amplitude may extend north- and westwards out of the dataset. The eastern set covers an area of 23.9 km^2 and has a long axis of 7.7 km striking NE – SW, and a short axis of 3.7 km. The eastern set appears to be pinching out in all directions. Both the western and eastern anomaly show reversed polarity compared to the seabed reflection and have a zone of acoustic masking extending roughly 500 ms (TWT) downwards (Fig. 4.20bc). Reflection continuity is

relatively high and does not appear to be affected by A6. Several deep-seated F2 faults are observed below the anomalies (Fig. 4.20a). The F2 faults, striking N – S and NE – SW, extends from Jurassic level and terminates in the lower to middle part of the Torsk Formation. The western anomaly set is located directly above the intersection points between the N – S striking and the NE – SW striking F2 faults. Acoustic masking is observed along the fault planes. The eastern anomaly set is located between two oppositely dipping NE – SW striking F2 faults, and its shape appears to be controlled by the faults (Fig. 4.20ab). Dimmed seismic reflections are observed along the fault plane along the NE – SW striking F2 faults.

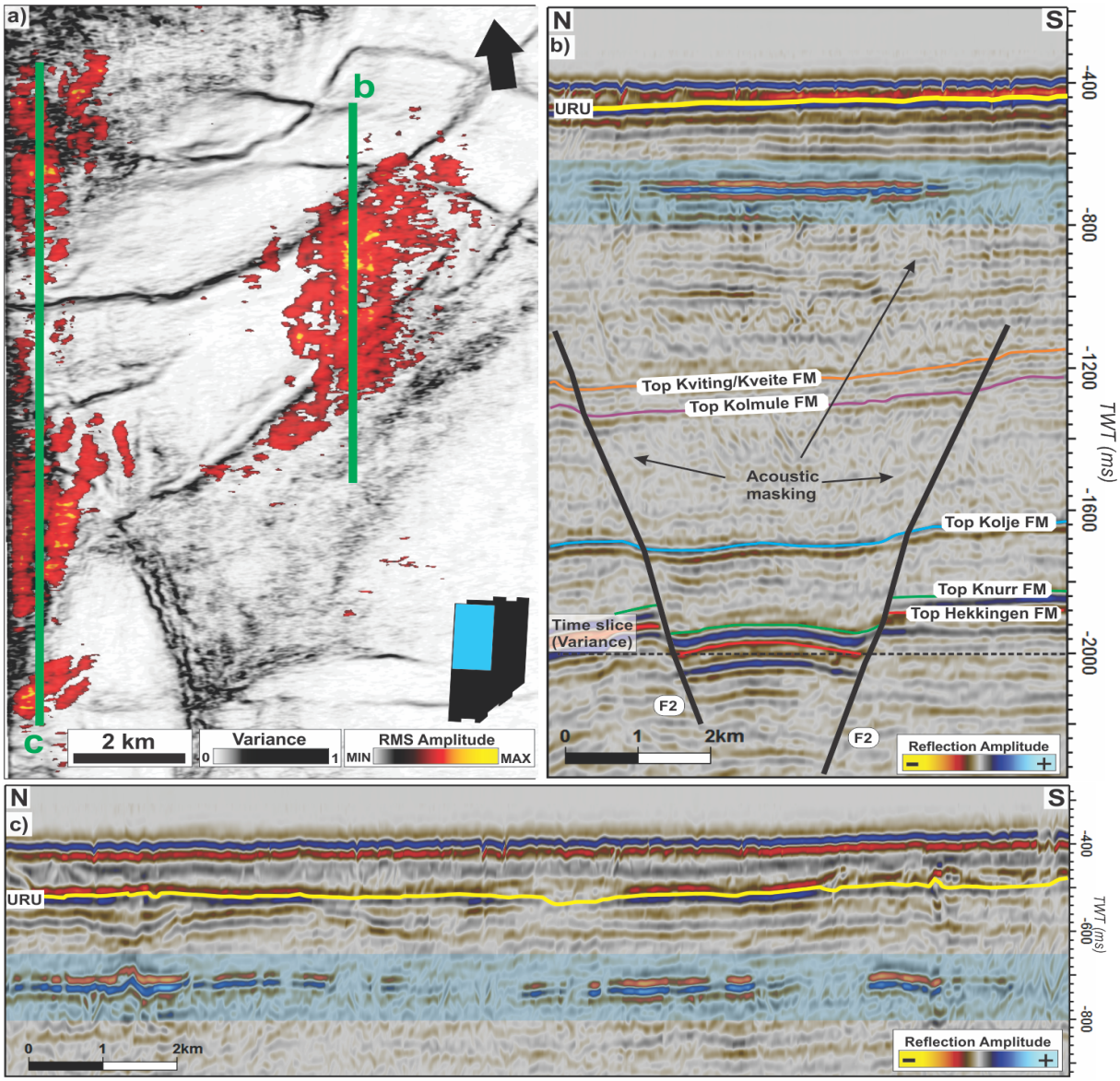

Fig. 4.20: ***a)*** *RMS amplitude map of amplitude anomaly A6 above variance time slice (2000 ms (TWT)). RMS amplitudes extracted from 200 ms (TWT) interval as indicated (blue shaded zone) in* ***b****. Position of map indicated in black polygon (survey ST8320R00) in the lower right corner, whose position is indicated in Fig. 4.14.* ***b)*** *N – S oriented seismic section through eastern part of A6 together with NE – SW striking F2 faults. Acoustic masking occur below the anomaly and along the fault planes. Position indicated in* ***a****.* ***c)*** *N-S oriented seismic section trough western part of A5. Position indicated in* ***a****.*

4.4.1.7 Seismic amplitude anomaly 7 (A7)

Seismic amplitude anomaly 7 is located at the western margin of survey ST0306 (Fig. 4.14 and Fig. 4.21). The amplitude has an elongated shape with the longest axis striking N – S to NE – SW, covering an area of 32.8 km^2. The longest axis measure 14.2 km and the shortest 3.1 – 6.5 km. The anomaly show reversed polarity compared to the seabed reflection and is located in the upper part of the Torsk Formation, between 680 and 870 ms (TWT), 240 ms (TWT) below the URU (Fig. 4.21b). The URU reflection that is situated directly above the anomaly has higher amplitude than the rest of the URU reflection. Adjacent reflections show low continuity and anomalous low amplitudes in a 2 – 4 km wide zone close to the anomaly. Below A7 a prominent zone of acoustic masking, acoustic chimney C6, occurs and distorts the seismic image in the deeper levels, where also a pull-down is observed (Fig. 4.21b). The zone of acoustic masking appears to have a slightly higher lateral extent than the overlying amplitude anomaly (Fig. 4.21b). Below A7, three E – W striking deep-seated F2 faults are identified (Fig. 4.21). These terminate in the middle to upper part of the Torsk Formation and do not appear to control the shape of amplitude anomaly 7. Poor seismic imaging prevents one to observe details of acoustic masking along the fault plane.

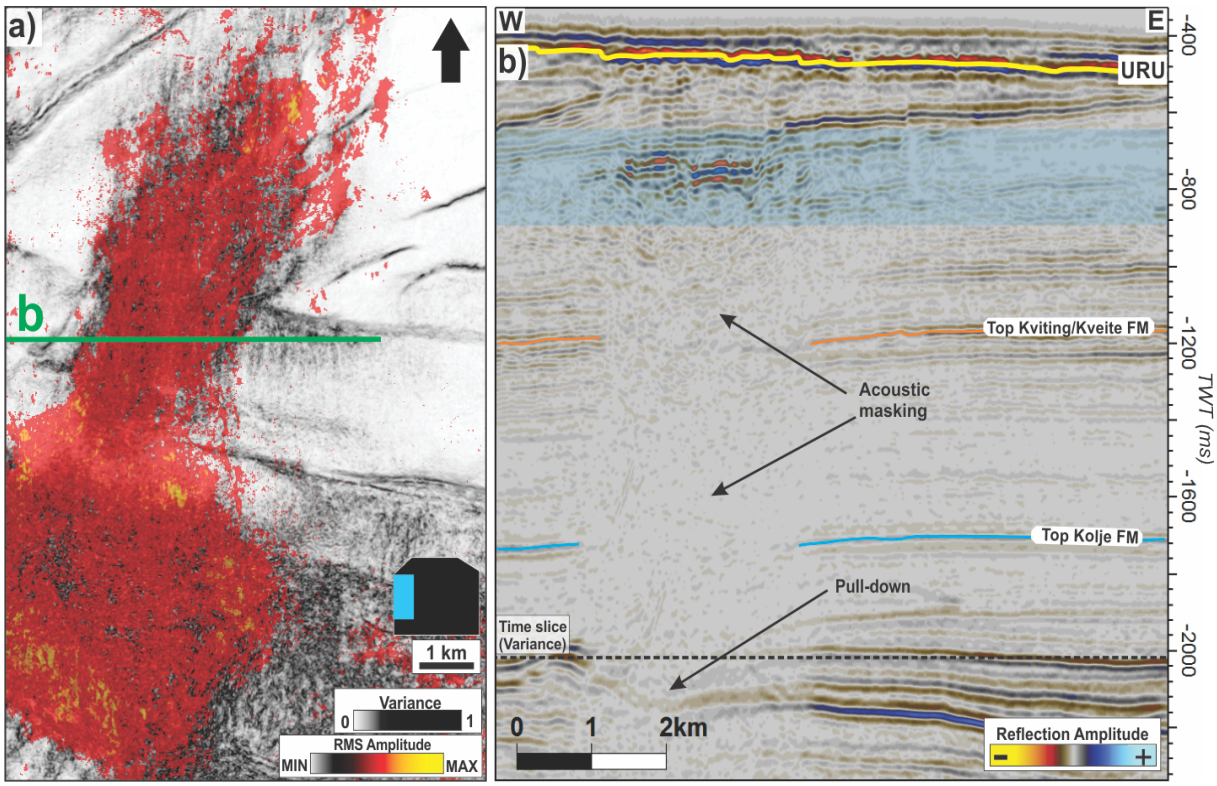

Fig. 4.21: ***a)*** *RMS amplitude map of amplitude anomaly A7 above variance time slice (2000 ms (TWT)).RMS amplitudes extracted from 200 ms (TWT) interval as indicated (blue shaded zone) in* ***b****. Position of map indicated in black polygon (survey ST0306) in lower left corner, whose position is indicated in Fig. 4.14.* ***b)*** *E – W oriented seismic section through A7 showing the extensive zone of acoustic masking below, and the pull-down. Position indicated in* ***a****.*

4.4.1.8 Seismic amplitude anomaly 8 (A8)

Seismic amplitude anomaly 8 is located in the northern part of survey ST0306 (Fig. 4.14 and Fig. 4.22). The anomaly is identified in the upper part of the Torsk Formation, between 650 and 730 ms (TWT), and have an elongated to oval shape with the longest axis striking NE – SW (Fig. 4.22ab). The anomaly covers an area of approximately 20.7 km^2, however it probably exceeds this as it extends out of the dataset towards northeast. The longest axis measure 8.8 km and the shortest 2 km. The seismic anomaly has reversed polarity compared to the seabed reflection, and appears to be following three clinoforms within the Torsk Formation, dipping incrementally toward the south-southwest (Fig. 4.22b). At the sides of the anomaly, the high amplitudes suddenly decrease and a narrow zone of acoustic masking occurs. The overlying URU reflection show anomalous high amplitudes directly above A8, having a slightly higher lateral extension than the A8 itself. Below the anomaly an extensive zone of acoustic masking occur, acoustic chimney C5, reducing the seismic image down to Jurassic level. A pull-down is observed in the underlying reflections (Fig. 4.22b). An E – W striking deep-seated F2 fault is identified below A8, extending from Jurassic level and terminating in the lower part of the Torsk Formation (Fig. 4.22ab). No enhanced seismic reflections are observed along the fault plane, although there is a high degree of acoustic masking in the proximity of the fault. The shape of A8 does not appear to be affected by the F2 faults.

4.4.1.9 Seismic anomaly 9 (A9)

Seismic amplitude anomaly 9 is located in the eastern part of survey ST0306 in the upper part of the Torsk Formation, 5 km southeast of seismic amplitude anomaly 8 (Fig. 4.14 and Fig. 4.22). A9 is characterized by a number of small high-amplitude reflections, each having a curvilinear shape. It is located between 700 and 750 ms (TWT), 180 ms (TWT) below the URU, and has reversed polarity compared to the seabed reflection. The URU reflection directly above A9 does not show anomalous high amplitudes (Fig. 4.22cd). In seismic sections the anomaly appears as a flat event, mimicking the seabed reflection, crosscutting the west – southwesterly dipping clinoforms of the Torsk Formation (Fig. 4.22cd). At the northern and southern side of A9, the surrounding reflections show low continuity and appear to have weaker amplitudes than the rest of the dataset, and a narrow zone of acoustic masking is observed. Acoustic masking is also identified directly beneath A9, and can be followed down to the underlying

Kviting/Kveite Formation, approximately 350 ms (TWT) below. The anomaly covers an area of approximately 36 km². Below A9, one E – W striking deep-seated F2 fault extends from Jurassic level, and terminates 80 – 90 ms (TWT) below the southern margin of the anomaly (Fig. 4.22ac). The F2 fault appears to influence the southern continuity of the anomaly, although it does not control the full extent of A9. No acoustic masking is observed along the fault plane.

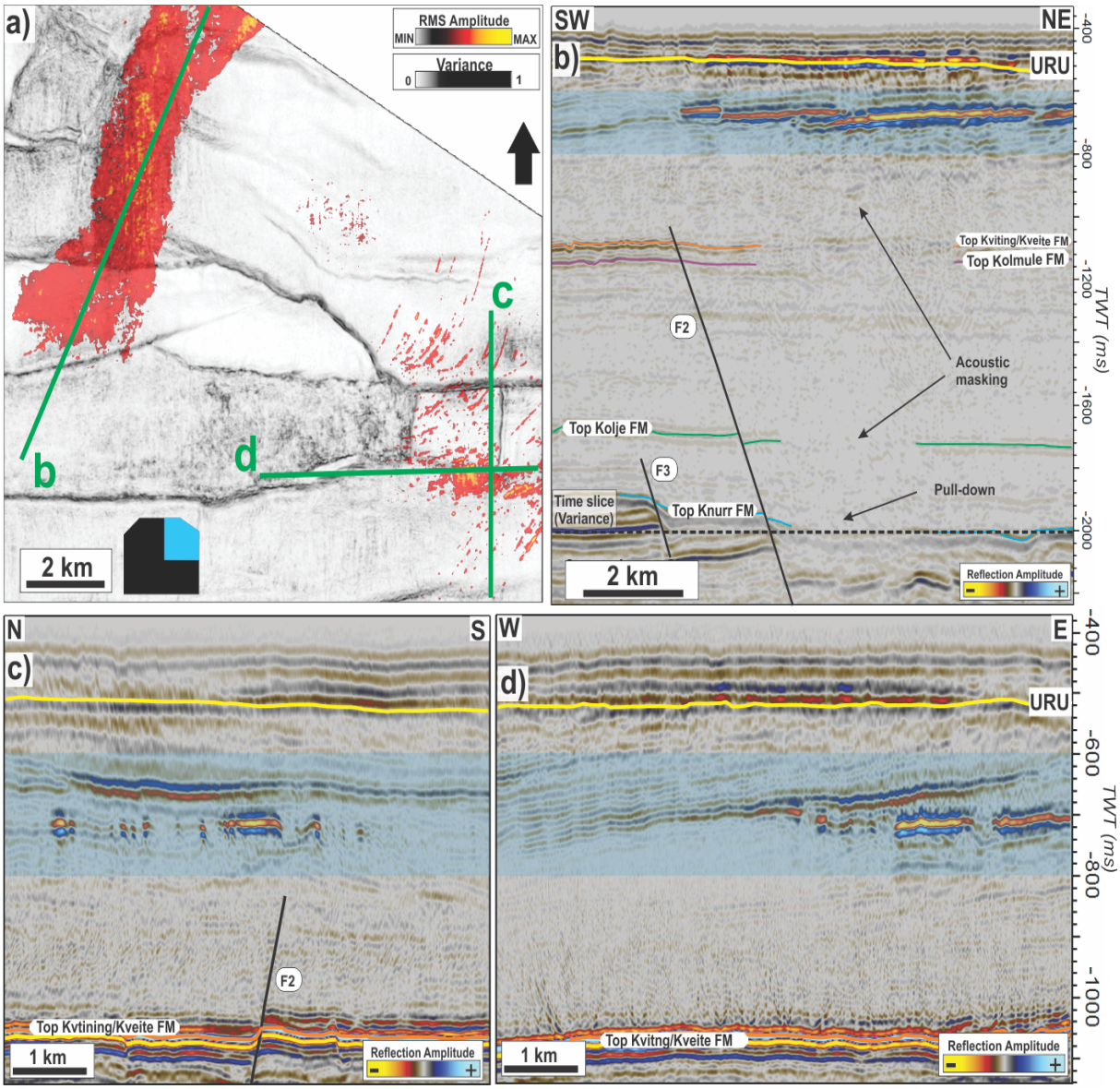

Fig. 4.22: ***a)*** *RMS amplitude map of amplitude anomaly A8 and A9 above variance time slice (2000 ms (TWT)). RMS amplitudes extracted from 200 ms (TWT) interval as indicated (blue shaded zone) in* ***b-d****. Position of map is indicated in black polygon (survey ST0306) in lower left corner, whose position is indicated in Fig. 4.14.* ***b)*** *N – S oriented seismic section through A8, showing E –W striking F2 fault. Extensive zone of acoustic masking indicated below A8, and an associated pull-down of the underlying reflections. Position of section indicated in* ***a****.* ***c)*** *N – S oriented seismic section through A9, showing an E – W striking F2 fault. Position indicated in* ***a****.* ***d)*** *E – W oriented seismic section through A9. The anomaly clearly cross-cut the south – southwesterly dipping clinoforms. Position indicated in* ***a****.*

4.4.1.10 Seismic amplitude anomaly 10 (A10)

Seismic amplitude anomaly 10 is located within the upper part of the Torsk Formation in the western part of survey ST05M09 (Fig. 4.14 and Fig. 4.23). The anomaly is of limited size compared to other amplitude anomalies in the Hammerfest Basin, as it covers only an area of 3.2 km². Its longest axis is oriented E – W and measures 850 m long. A small zone of acoustic masking is identified below the bright spot, reaching down to the Kviting/Kveite Formation, approximately 200 ms (TWT) below (Fig. 4.23b). An E – W striking deep-seated F2 fault extends from deeper levels and terminates in the upper part of the Torsk Formation. The fault plane is located only 0.6 km away from A10.

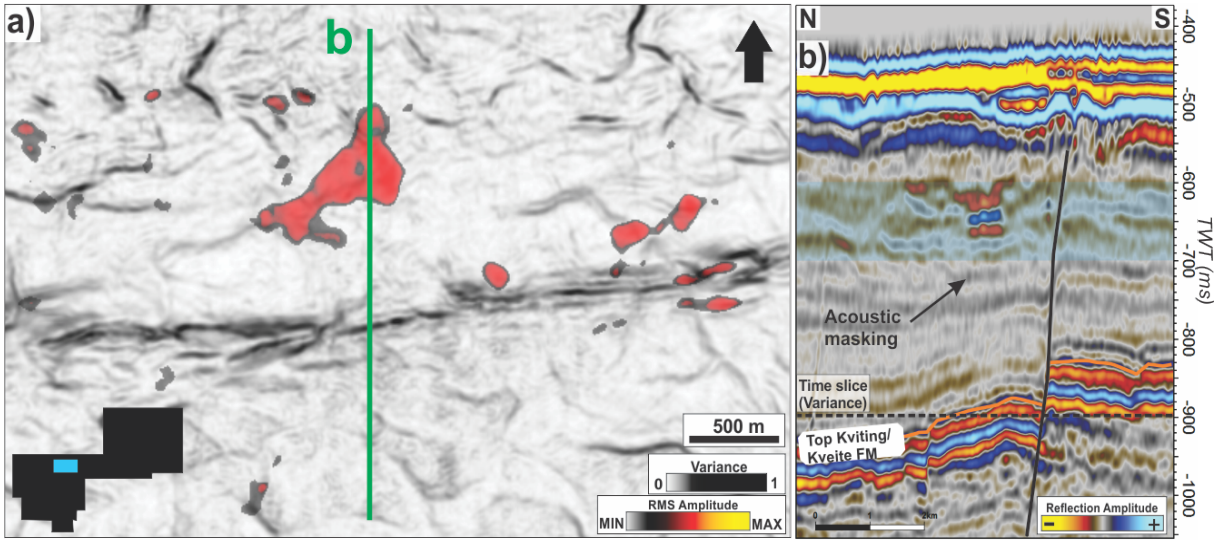

Fig. 4.23: ***a)*** *RMS amplitude map of amplitude anomaly A10 over variance time slice (900 ms (TWT)). RMS amplitudes extracted from 100 ms (TWT) interval as indicated (blue shaded zone) in* ***b****. Position of map indicated in black polygon (survey ST05M09) in lower left corner, whose location is indicated in Fig. 4.14.* ***b)*** *N –S oriented seismic section through A10, showing an E – W striking F2 fault terminating underneath URU and acoustic masking. Position indicated in* ***a****.*

Amp. Nr.	*Survey*	*Area (km²)*	*Formation*	*Top TWT (ms)*	*Base TWT (ms)*
1	LN09M01	28.6	Torsk	600	690
2	OMV0801	31.7	Kviting/Kveite	1060	1300
3	LN0901	17.5	Kviting/Kveite	1170	1250
4	LN0901	21.2	Torsk	630	740
5	LN0901	21.9	Torsk	820	960
6	ST8320R00	40.7	Torsk	600	730
7	ST0306	32.8	Torsk	680	870
8	ST0306	20.7	Torsk	650	730
9	ST0306	36	Torsk	700	750
10	ST05M09	3.2	Torsk	610	670

Table 4.4: Summary of the amplitude anomalies below the URU. Formation is the geologic the formation the amplitude anomalies are confined to. The top and base are defined as the uppermost and lowermost point of the anomalous high amplitudes.

4.4.2 Amplitudes anomalies along the URU

A total of 68 high amplitude anomalies along the URU reflection are observed within the study area (Fig. 4.24). The majority of the anomalies that have been identified along URU are smaller in size than the anomalies below URU, although, one of the largest anomalies that have been mapped occur along URU. The amplitude anomalies along the URU commonly occur in groups and occasionally they are located directly above deeper-lying anomalies (A1 – A10) within the Torsk and Kviting/Kveite formations (chapter 4.4.1), and where clinoforms of the underlying Torsk Formation have been truncated. In general the anomalies are characterized by having the same polarity as the seabed reflection but higher amplitudes than the surrounding URU reflection. High amplitudes that have been observed where the URU reflection coincides with the seabed reflection have been excluded from this study as these most likely represents the high contrast in acoustic impedance between the water and the consolidated pre-URU sediments. To document the character and distribution of amplitude anomalies, the study area is divided into four regions: *northwestern*, *northeastern*, *southwestern* and *southeastern*.

4.4.2.1 Northwestern region

Amplitude anomalies in the northwestern region (survey LN09M01, LN0901 and OMV0801) generally occur above deeper amplitude anomalies (Fig. 4.24). The 17 anomalies that are identified in this region have an average surface area of 7.3 km^2. All the anomalies are characterized by having the same polarity as the seabed reflection where the reflection itself has anomalously high amplitude (Fig. 4.25bd). The shape varies from elongated to oval (Fig. 4.25ac), often mimicking the underlying amplitude anomalies, where present. The longest axis measure 3 to 12 km and show a preferred orientation of NW – SE, although other orientations occur. The short axis varies from 0.5 to 5 km. Acoustic masking is occasionally observed beneath the anomalies, mainly in the areas where deep-seated faults emerge (Fig. 4.25b).

Within the northwestern region the highest concentration of amplitude anomalies occurs in proximity the E – W striking F1 fault separating the Hammerfest Basin from the Loppa High (Fig. 4.24). It is apparent that the anomalies occasionally follow the fault trace and that the high amplitudes occur directly above the upper termination of faults (Fig. 4.25b).

Within survey OMV0801 and the southern part of survey LN09M01, there appear to be a link between the anomalies and south-southwesterly dipping clinoforms of the Torsk Formation (Fig. 4.25bd). The clinoforms show high continuity, and the strong reflections commonly occur at their upper termination where they are truncated by the URU. The largest amplitude anomaly within the northern region, covering 63 km^2, is located above such clinoforms (Fig. 4.25cd).

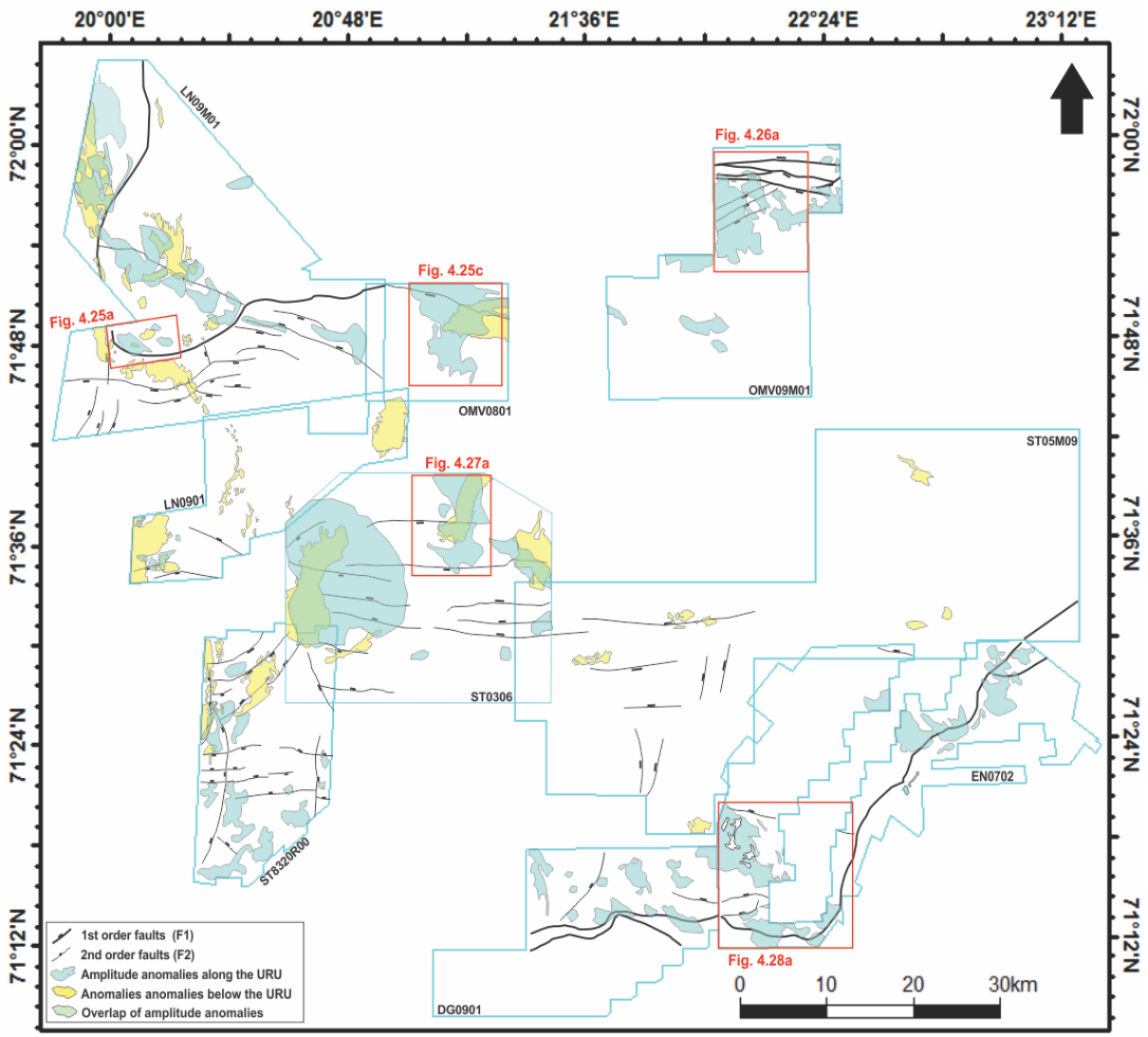

Fig. 4.24: Overview of amplitude anomalies within the study area. Amplitude anomalies below URU (yellow areas) (A1 – A10) and along the URU (blue areas) are mapped. Overlap of amplitude anomalies are shown in green. 1st order and 2nd order faults are included in the overview. Red rectangles show positions of other figures describing the area.

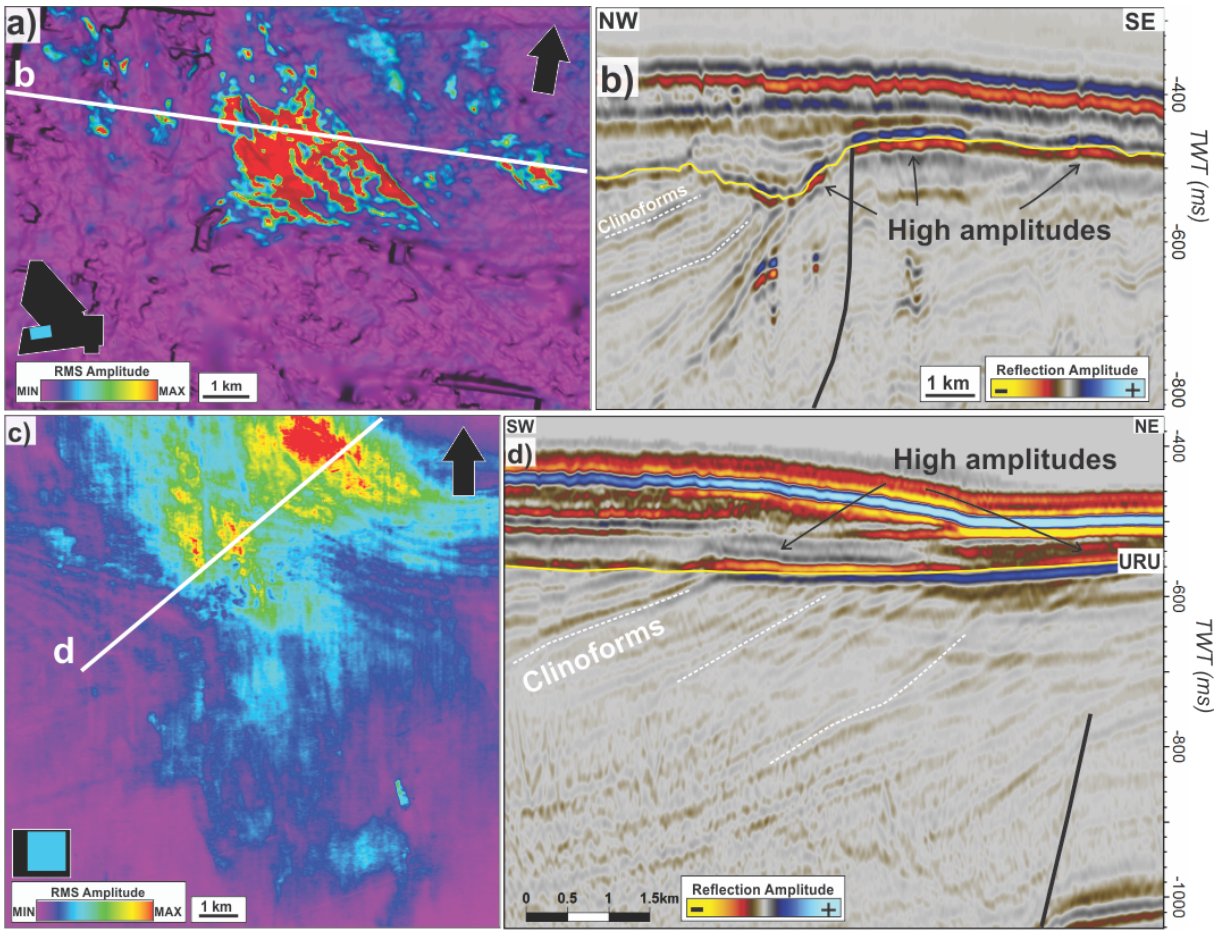

Fig. 4.25: ***a)*** *RMS amplitude map of amplitude anomaly along the URU. Amplitudes extracted from blue shaded interval in* ***b*** *(10 ms (TWT) above and below the URU reflection). Position of map indicated in black polygon (survey LN09M01) in lower left corner, whose position is indicated in Fig. 4.24.* ***b)*** *NW – SE oriented seismic section through amplitude anomaly, showing E – W striking F1 fault. Position indicated in* ***a****.* ***c)*** *RMS amplitude map of amplitude anomaly along the URU. Amplitudes extracted from blue shaded interval in* ***c*** *(10 ms (TWT) above and below the URU reflection) Position is indicated in black square in lower left corner (survey OMV0801), whose position is indicated in Fig. 4.24.* ***d)*** *NE – SW oriented seismic sections through amplitude anomaly at the URU, showing E – W striking F2 fault. Position indicated in* ***c****.*

4.4.2.2 Northeastern region

Within the northeastern region (survey OMV09M01) 10 amplitude anomalies are identified along the URU (Fig. 4.24). The anomalies are characterized by having anomalous strong reflections with the same polarity as the seabed. No acoustic masking is observed below the amplitudes and the anomalies do not appear to be affecting the already poor seismic signal. The majority of the amplitude anomalies in the northeastern region are located in the northern part of the dataset, above E – W and NE – SW striking F1 and F2 deep-seated faults, respectively. Four anomalies occur above the F1 faults, in the easternmost part of the survey. These are circular to sub-circular in shape and have the longest axis oriented NE – SW. The radius varies from 0.8 km to 2.5 km, and covers an area between 2 and 5 km^2.

Three anomalies are located above the NE – SW striking F2 faults and are identified in the northern part of the survey (Fig. 4.26). These have an oval shape with the longest axis striking NNW – SSE, nearly perpendicular to the underlying F2 faults. The long axis varies between 4.0 km to 9.7 km, and the short axis between 1.2 km and 3.4 km.

In the southern part of the survey, three anomalies are identified (Fig. 4.24). The anomalies have an elongated to oval shape, where the longest axis is striking NW – SE. The length of the longest axis varies between 2.1 km and 6 km, and the short axis between 0.8 and 3 km. Below the anomalies westerly dipping clinoforms exists. These show low continuity and amplitude, and do not appear to be linked to deeper amplitude anomalies. No deep-seated faults are identified below these anomalies.

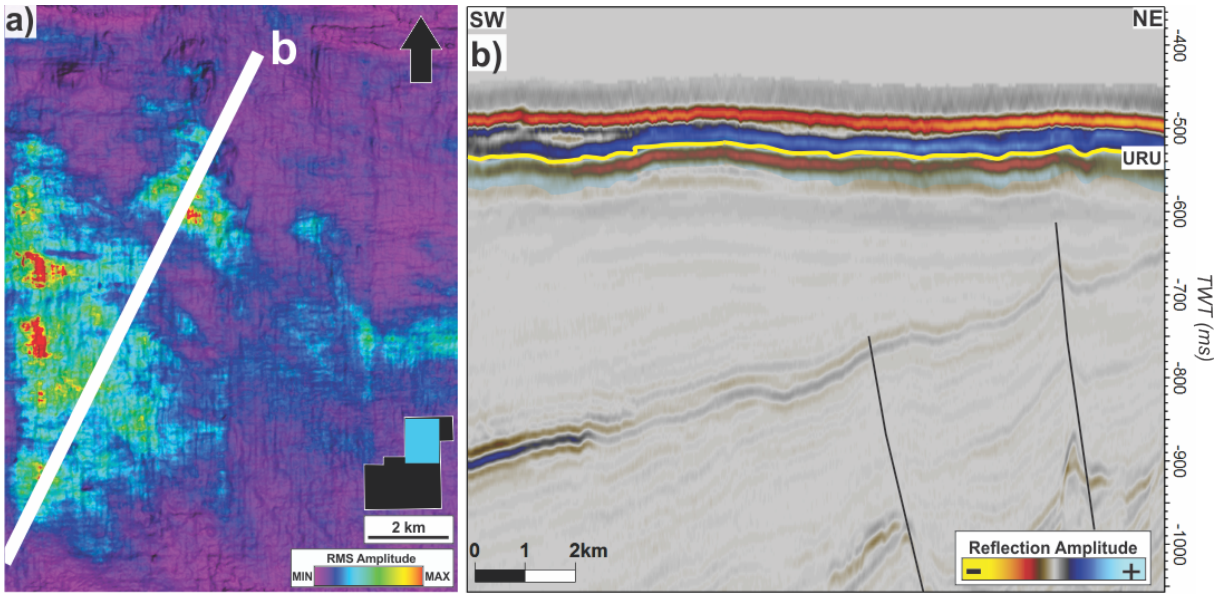

*Fig. 4.26: RMS amplitude map of amplitude anomalies along the URU. Amplitudes are extracted from a 10 ms (TWT) interval (blue shaded zone in **b**) below the URU reflection. Position of map indicated in polygon (survey OMV09M01) in the lower right corner, whose position is indicated in Fig. 4.24. **b)** NE – SW oriented seismic section through amplitude anomalies, showing NE – SW striking F2 faults. Position indicated in **a**.*

4.4.2.3 Southwestern region

In the southwestern region (survey ST8320R00 and ST0306) 18 amplitude anomalies have been identified (Fig. 4.24), the highest number in the Hammerfest Basin. The anomalies show high amplitudes, and the seismic reflector shows the same polarity as the seabed reflection. Acoustic masking and dimmed seismic reflections are observed below the anomalies, reaching up to 120 ms (TWT) below the URU. Laterally along the URU, away from the anomalies, the high amplitudes abruptly decrease and the continuity of the URU reflection is reduced. The seabed reflection does not show

anomalous high amplitudes above anomalies along the URU. In the southern part of survey ST8320R00, 7 anomalies are observed (Fig. 4.24). They have an elongated to oval shape are randomly oriented. The long and short axis measures 1-9 km and 0.5-3.9 km, respectively. They cover an area between 0.5 and 70 km^2. The deep-seated F2 faults identified in this area occur in proximity to the amplitude anomalies.

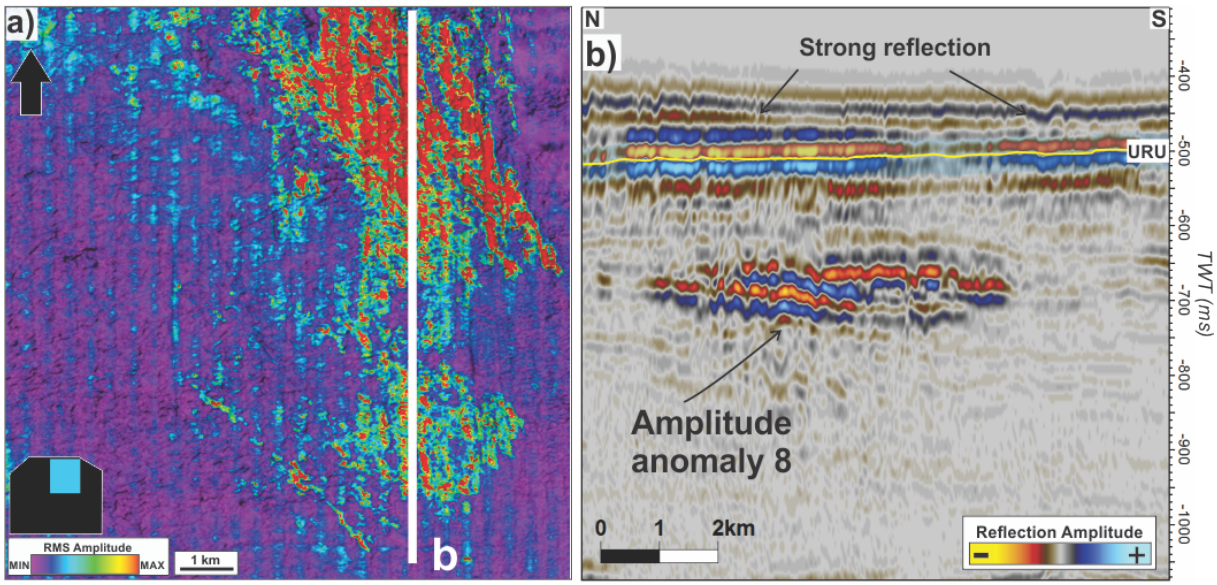

Fig. 4.27: ***a)*** *RMS amplitude map of amplitude anomaly located directly above amplitude anomaly A8. RMS amplitudes extracted from blue shaded zone (15 ms (TWT) above and below the URU reflection) in* ***b****. Position of map indicated in black polygon (survey ST0306) in lower left corner, whose location is indicated in Fig. 4.24.* ***b)*** *N-S striking seismic section showing amplitude anomalies both on and below the URU reflection. Position is indicated in* ***a****.*

In survey ST0306 and the northern part of survey ST8320R00, the majority (70 %) of the anomalies along the URU occur directly above deeper-lying anomalies (Fig. 4.24 and Fig. 4.27). In the northern part of survey ST8320R00, three anomalies are identified being directly above amplitude anomaly 6 (A6) within the Torsk Formation, all being smaller in size than A6. The anomalies have an elongated shape with the longest axis oriented NE – SW, the same direction as underlying F2 faults. The F2 faults appear to terminate in the lower to middle part of the Torsk Formation, hence not being linked to the anomalies along the URU. However, connections through shallow faults (not resolved in the seismic data) cannot be ruled out. Within survey ST0306, 3 anomalies occur directly above the deeper amplitude anomalies A7, A8 and A9 (Fig. 4.24 and Fig. 4.27). The anomalies in this area have an oval to sub-circular shape, where the longest axis is oriented NW – SE (Fig. 4.27a). In contrast to survey ST8320R00, the shallow anomalies within this survey all cover larger areas than the underlying anomalies. The largest amplitude anomaly that has been identified within the study area covers 60 km^2 and is located approximately 260 ms (TWT) directly above A7.

4.4.2.4 Southeastern region

Within the southeastern region (survey DG0901, EN0702 and ST05M09) 23 anomalies exists along the URU (Fig. 4.24). They generally have an elongated to oval shape where the longest axis is striking NW – SE. The long and short axis of the anomalies measures 0.8 – 4.0 km and 0.5 – 2.9 km, respectively. They occur in an area where E – W and NE – SE striking F1 faults separates the Hammerfest Basin from the Finnmark Platform. There does not appear to be any link between the faults and the anomalies. No deep-lying anomalies within the Torsk Formation are located directly below the zones of high amplitudes (Fig. 4.24). Clinoforms dipping towards the south-southwest are observed in survey DG0901 and the southwestern part of survey EN0702 (Fig. 4.28). Amplitude anomalies are observed in particular where URU truncates the upper part of the clinoforms. The seismic data shows no sign of acoustic masking above or below the anomalies.

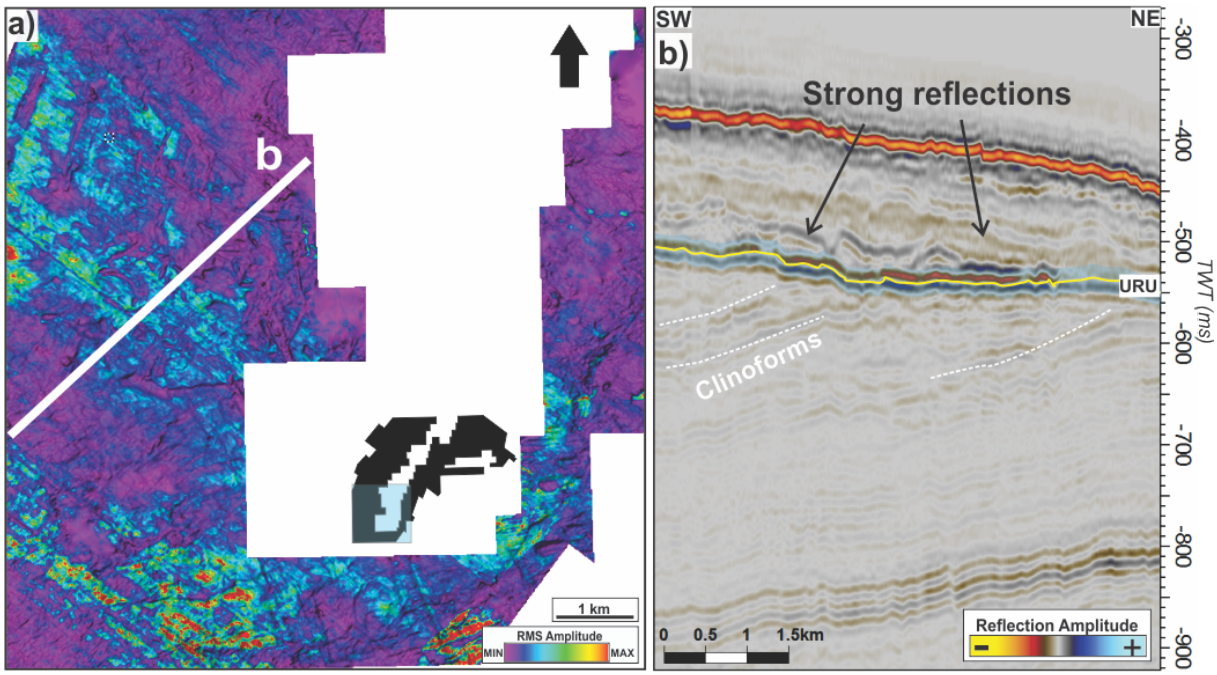

Fig. 4.28: ***a)*** *RMS amplitude map showing NW-SE trending amplitude anomalies. RMS amplitudes have been extracted from shaded blue zone (10 ms (TWT) above and below the URU reflection) in* ***b****. Position of map is indicated in black polygon (survey EN0702) in the centre of the picture, whose location is indicated in Fig. 4.24.* ***b)*** *NE-SW oriented seismic section showing an amplitude anomaly and south-southwesterly dipping clinoforms. Position of seismic section indicated in* ***a****.*

4.5 Morphological circular to sub-circular depressions

During this study several morphological circular to sub-circular depressions have been identified and mapped on the seabed and URU.

4.5.1 Depressions on the seabed

The interpreted seabed reflections provide insights into seabed geomorphology and thus interpretation of related processes (Fig. 4.29). The water depth within the study area varies from 325 – 565 ms (TWT), which correspond to 240 – 420 m (TVD) assuming a water velocity of 1500 m/s (Table 3.2). The shallowest water depth occurs in the western area, being part of the eastern flank of the Tromsøflaket, a shallow bank in the southwestern Barents Sea (Winsborrow et al., 2010). Eastwards the water depth gradually increases to 300 –350 m (TVD) coming into the NW – SE oriented Ingøydjupet, a major glacial trough (Andreassen et al., 2007b; Andreassen et al., 2008). Ingøydjupet is deepest in the southeast (420 m) and is getting shallower toward northwest (370 m).

Randomly oriented curvilinear furrows frequently occur in the study area (Fig. 4.30 and Fig. 4.32). These are typically U- or V-shaped, 5 – 17 m deep, and can be followed up to 25 km. The width varies from 20 to 400 m, and occasionally levees are observed at one or both sides. The furrows are interpreted to represent iceberg plough marks that was formed when the keels of icebergs, detached from a glacier terminus, scoured the seabed sediments when transported by wind and currents (e.g. Barnes et al., 1988; Andreassen et al., 2007b; Andreassen et al., 2008). In addition to furrows, large sub-parallel troughs are observed crossing the study area (Fig. 4.29) The majority of these are oriented NW – SE and can be followed up to 40 km. Furrows commonly occur within and overprint the troughs, indicating that the troughs predates the furrows. The width varies from 2 – 5 km and the depth from a few metres up to 15 m. The troughs have previously been described in the study area and are interpreted to represent mega-scale glacial lineations (MSGL), erosional features that results from erosion at the base of fast-flowing ice streams (Ottesen et al., 2005; Andreassen et al., 2007b; Andreassen et al., 2008).

Circular to sub-circular depressions are observed all over the seabed and occur in different sizes and shapes, within and outside glacial features. Below the depressions are divided into two groups: *small depressions* (up to 600 m wide) and *mega depressions* (above 600 m wide) (Table 4.5).

4.5.1.1 Small depressions: pockmarks

Detailed and thorough investigation of the seismic datasets reveals that the distribution and density of 425 small (less than 600 m in diameter) depressions is widely variable across the Hammerfest Basin (Fig. 4.29). The highest density of small depressions occurs in the central and southern part of the study area. Along the northern margin they are spaced significantly farther apart. Apparently, no link exists between water depth and seabed depressions.

The small depressions generally have a width of 65 – 230 m and a depth of 5 – 30 m. Occasionally they are identified within the iceberg plough marks and the MSGL, either alone or in chains of 3 – 5 depressions. Similar features have been described elsewhere on the Norwegian continental shelf, but also within the study area. They have successively been interpreted as pockmarks (e.g. Judd and Hovland, 2007; Chand et al., 2008; Chand et al., 2009; Chand et al., 2012; Ostanin et al., 2013; Vadakkepuliyambatta et al., 2013). Depressions also occur in junctions where the survey footprints (seismic artefacts) cross the plough marks. These are interpreted to be artificial and hence excluded from this study. The study area is divided into the same regions (*northwestern, northeastern, southwestern and southeastern*) as used in chapter 4.4.2 to describe and document the distribution of pockmarks.

In the *northwestern region* (survey LN09M01, LN0901 and OMV0801) a total of 35 pockmarks are identified (Fig. 4.29). They occur within iceberg plough marks, both alone and in groups (Fig. 4.30). The pockmarks have a sub-circular to elongated shape where the longest axis measures 65 – 170 m, and the depth between 4 – 23 m (Fig. 4.30de), assuming a water velocity of 1500 m/s (Table 3.2). In general the pockmarks have steep sidewalls and appear to be both U- and V- shaped. Acoustic masking and pipe structures are only occasionally observed below. Underlying deep-seated F1 and F2 faults commonly occur in proximity to seabed pockmarks in the northwestern region (Fig. 4.29). In survey LN09M01, amplitude anomalies along the URU are occasionally observed below the pockmarks (Fig. 4.30bc), however this is not the case for the rest of the region.

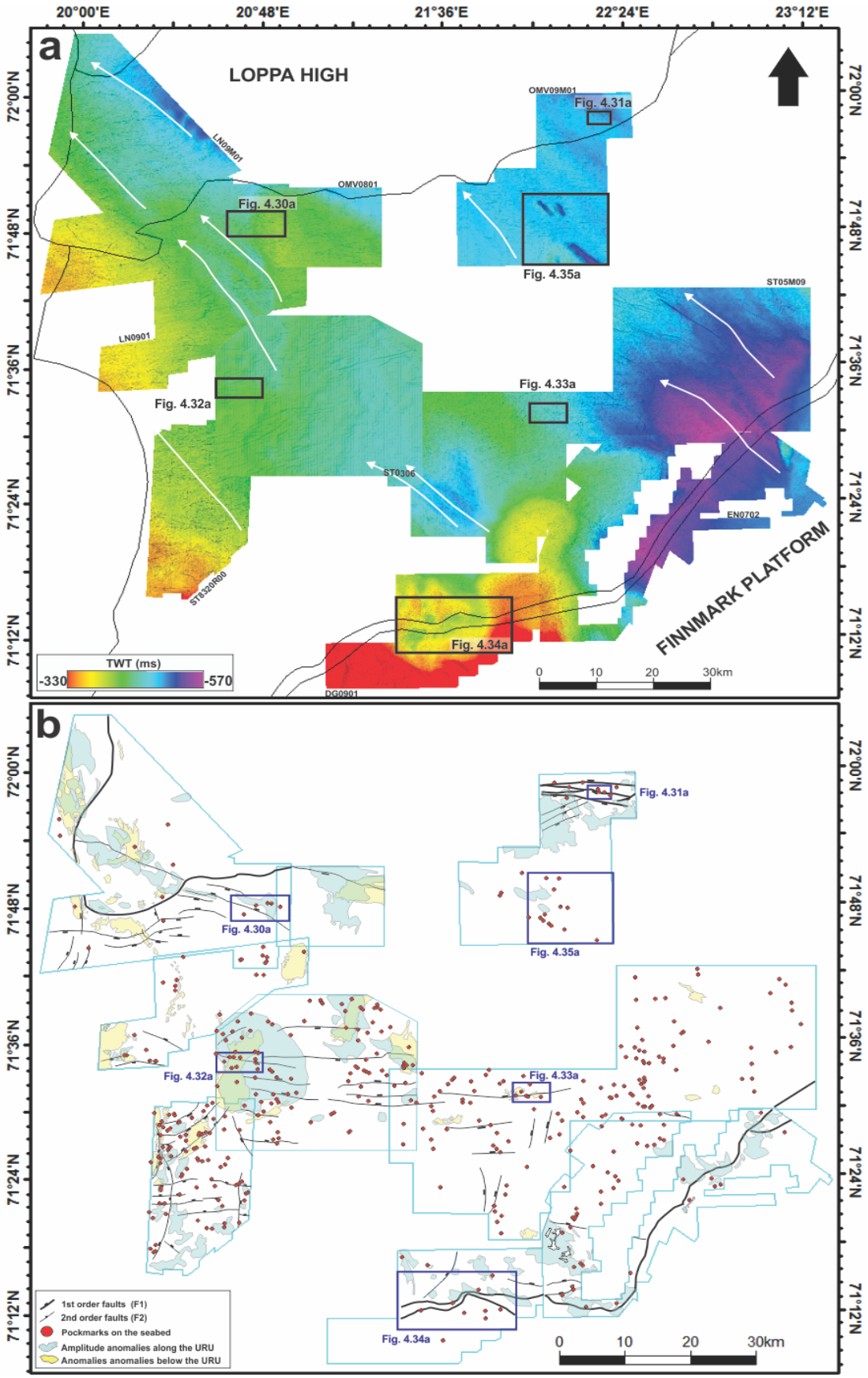

Fig. 4.29: ***a)*** *Overview of the interpreted seabed reflections. White arrows indicate the position and orientation of the MSGL. Black and blue rectangles show the position of other figures describing the area.* ***b)*** *Overview of the study area showing the position of the small seabed depressions. Amplitude anomalies below and along the URU is indicated in shaded yellow and blue zones, respectively. Deep-seated F1 and F2 faults are indicated by black lines.*

In the *northeastern region* (survey OMV09M01) 24 seabed pockmarks are identified (Fig. 4.29). They occur in the northern and southern part of the survey, respectively, and appear to have the same size and shape as the northwestern region, being sub-circular to elongate. The majority of the pockmarks do not occur within iceberg plough marks, although a few examples exists. Commonly they occur in groups of 3 – 7 pockmarks where the smaller ones surround one or two larger pockmarks (Fig. 4.31a). The depth varies between 6 and 18 m (V_P = 1500 m/s), being slightly shallower than the westernmost pockmarks. In the northeastern part of the survey the pockmarks are located directly beneath E – W striking deep-seated F1 faults (Fig. 4.31b). No acoustic masking or pipe structures are observed between the F1 faults and the pockmarks. The underlying URU reflection does not show anomalous high amplitudes. In the southern part of the survey (OMV09M01) no deep-seated faults are observed beneath the pockmark depressions. High amplitude anomalies along the URU reflection occur on occasion beneath the pockmarks, although the distribution does not appear to be controlled by the amplitude anomalies. The depth and size of the pockmarks in the northern and southern part of the survey are relatively similar.

In the *southwestern region* (survey ST8320R00 and ST0306) a very high number of 187 pockmarks are identified (Fig. 4.29). The majority occurs within iceberg plough marks, either alone or in groups of 3 – 8. Commonly the larger pockmarks are surrounded by several smaller ones (Fig. 4.32). The shape is sub-circular to elongate where the longest axis, which have a preferred orientation of E – W to NW – SE, measures 70 – 230 m. The depth is in the range of 5 – 28 m (V_P = 1500 m/s). Pockmark depressions can be both U- and V-shaped and appear to have pairs of two steep and two gentle dipping walls. Commonly the steep walls are those of the long axis (Fig. 4.32b). Acoustic masking and pipe structures are only occasionally identified below the pockmarks, and are, similar to the northwestern region, the exception rather than the rule. The pockmarks in this area frequently occur above underlying amplitude anomalies, both below and along the URU reflection (Fig. 4.29 and Fig. 4.32). N – S, NE – SW and E – W striking deep-seated F2 faults are located beneath the areas of highest pockmark density. None of the deep-seated faults reach the URU reflection.

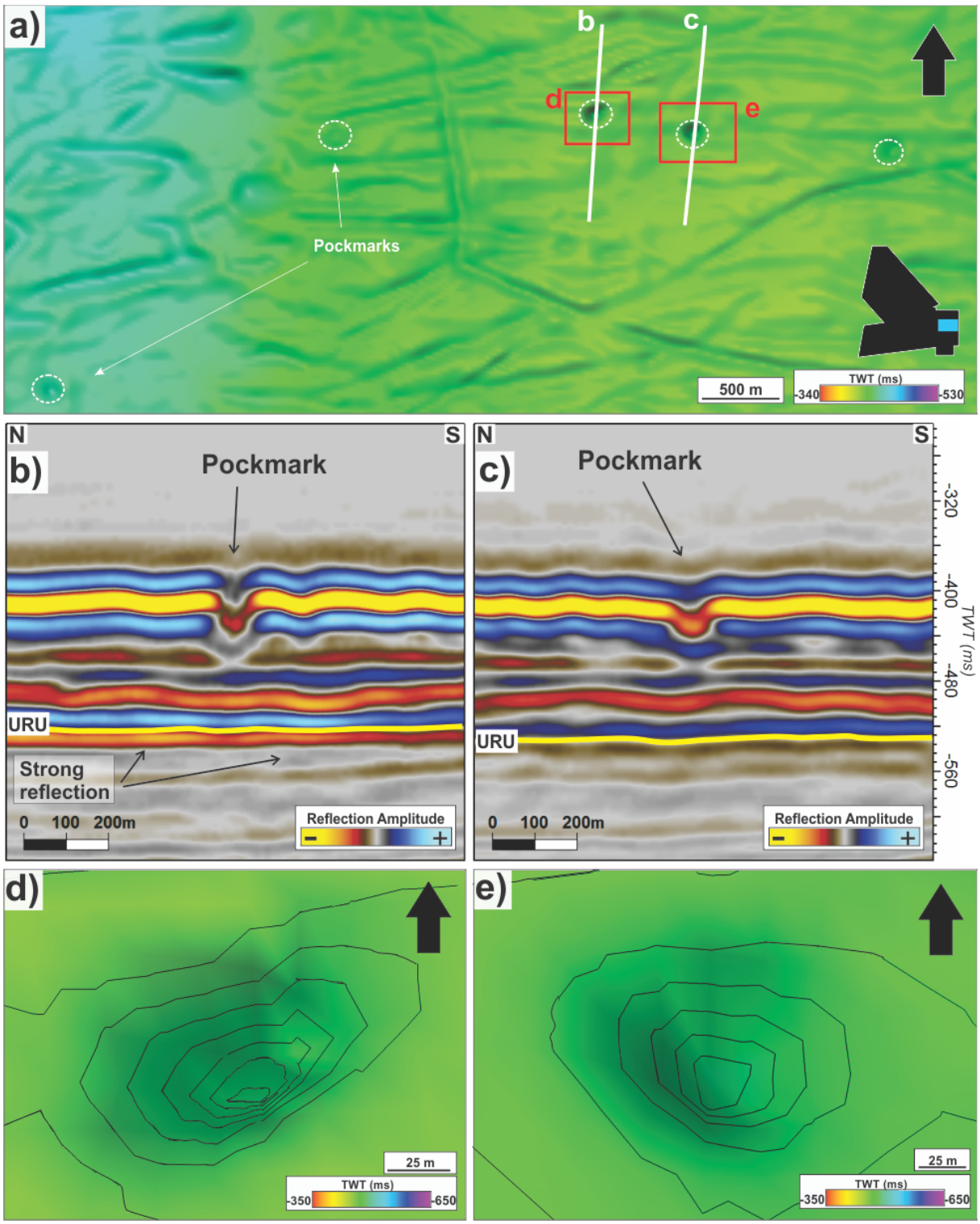

Fig. 4.30: ***a)*** *Map of seabed pockmarks and iceberg plough mark. Position of map indicated in black polygon (survey LN09M01) in the lower right corner, whose position is indicated in Fig. 4.29.* ***b & c)*** *N – S oriented seismic section showing pockmark depression within iceberg plough mark. Position indicated in* ***a. d & e)*** *Close-up picture of pockmark depression showing the sub-circular to elongated shape and steep sidewalls. Position indicated in a.*

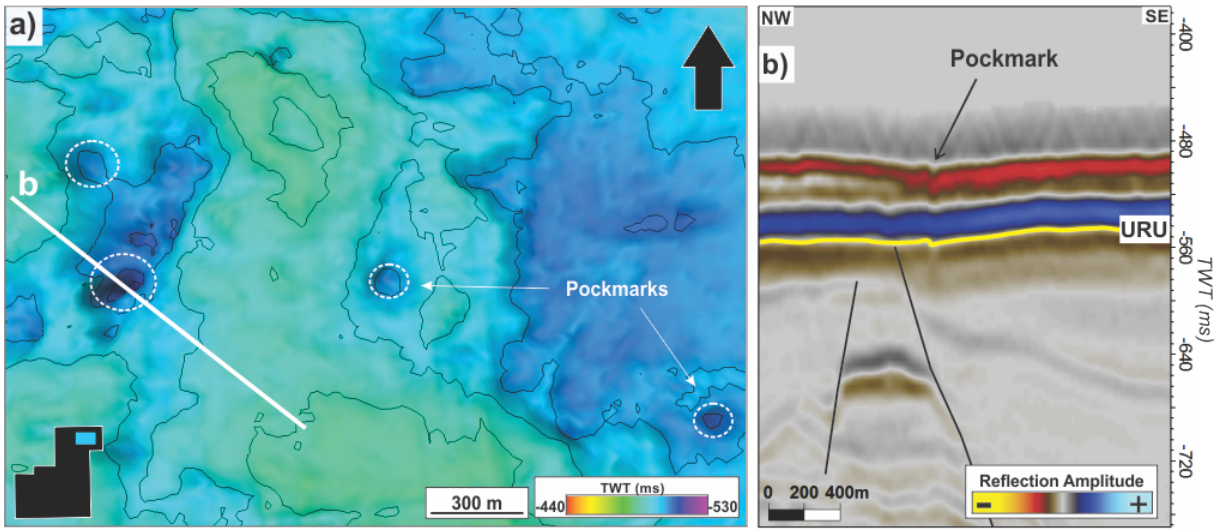

Fig. 4.31: ***a)*** *Overview map of pockmarks on the interpreted seabed reflection. One large pockmark depression surrounded by three smaller pockmarks. Position of map is indicated in black polygon (survey OMV09M01) in the lower left corner, whose position is indicated in Fig. 4.29.* ***b)*** *NW – SE oriented seismic section through large pockmark. Due to the low quality of the seismic data the pockmark depression does not stand out on the reflection. Position of indicated in* ***a****.*

In the *southeastern region* (survey ST05M09, DG0901 and LN0702) a high number of 179 pockmarks exists (Fig. 4.29). The majority of them occur outside iceberg plough marks, commonly in groups of 2 or 3 (Fig. 4.33). The pockmarks have a circular to elongated shape where the longest axis, 50 – 200 m long, are randomly oriented. They are both U- and V-shaped and have a depth of 7 – 23 m (V_P = 1500 m/s) (Fig. 4.33de). The highest concentration of pockmarks occur within survey ST05M09 and gradually decrease towards the Finnmark Platform in the south. Several N – S and E – W striking deep-seated F2 faults are observed below the pockmark depressions. Many seabed pockmarks occur along the NE – SW to E – W striking F1 fault at the southern limit of the Hammerfest Basin (Fig. 4.29). Amplitude anomalies along the URU reflection are also observed in proximity to the faults and pockmarks. Acoustic masking and pipe structures are not observed.

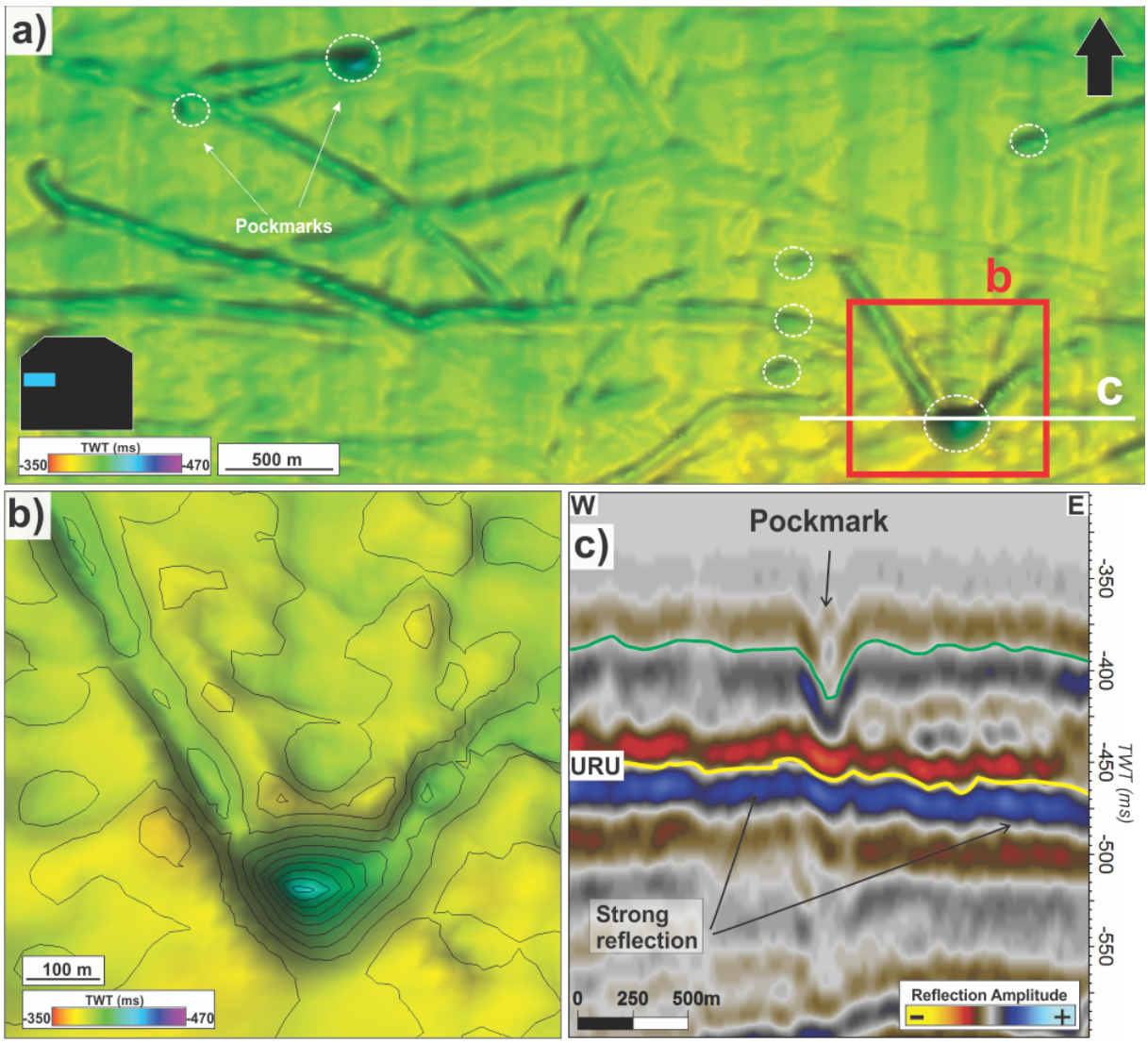

Fig. 4.32: ***a)*** *Overview map of pockmarks located both within and outside iceberg plough marks. Pockmarks occur both alone and in groups, and occasionally the smaller pockmarks is in proximity to a large pockmark. Position of map is indicated in black polygon (survey ST0306) in lower left corner, whose position in Fig. 4.29.* ***b)*** *Close-up picture of a large pockmark located within an iceberg plough mark. Position indicated in* ***a****.* ***c)*** *E – W oriented seismic section through a large pockmark, showing the high amplitudes of the underlying URU reflection. Position indicated in* ***a****.*

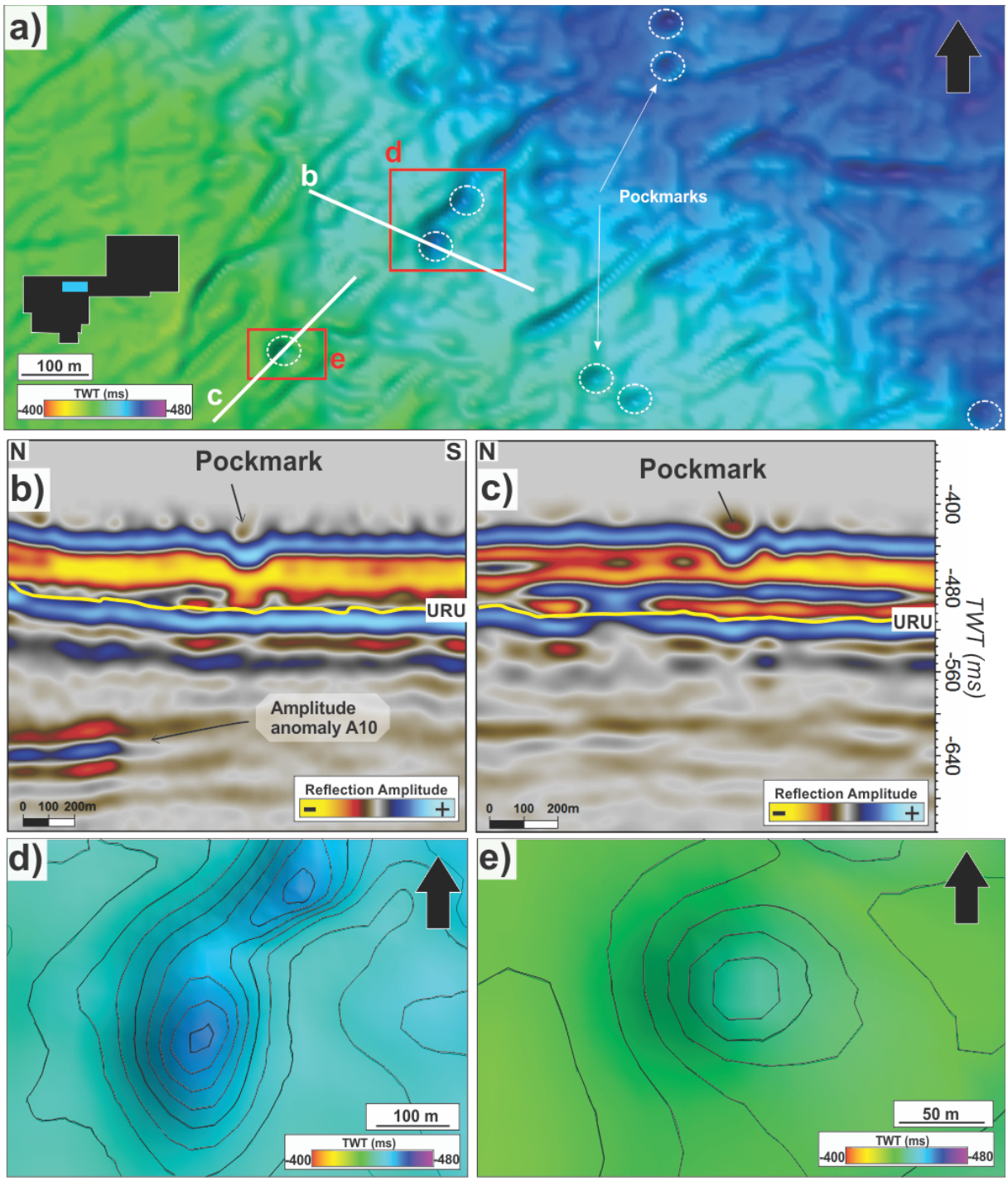

Fig. 4.33: ***a)*** *Overview map of pockmarks located within and outside iceberg plough marks. Position is indicated in black polygon (survey ST05M09) in lower left corner, whose position is indicated in Fig. 4.29.* ***b & c)*** *Seismic sections through pockmarks. Pockmark in* ***b*** *is located in proximity to amplitude anomaly A10 within the Torsk Formation. Position of seismic sections indicated in* ***a****.* ***d & e)*** *Close-up picture of pockmarks showing the circular to elongated shape. Position indicated in* ***a****.*

4.5.1.2 Mega depressions

The interpreted seabed reflection in the study area reveal several depressions that are significantly larger than the previously described features. The depressions are larger than 600 m in diameter and are classified as *mega depressions* (Table 4.5). The mega depressions are identified at two locations within the Hammerfest Basin, in the northeastern area and southeastern area, respectively. None of the mega depressions, which are termed D1 – D10, appear to be linked with underlying faults or structures, or amplitude anomalies. Smaller seabed depressions are only occasionally observed within the mega depressions. The southern and northern area will be described separately.

In the southern area, in the centre of survey DG0901, six (D1 – D6) mega depressions are identified (Fig. 4.34). Being located on the eastern flank of the Tromsøflaket, the water depth is in the range of 170 – 340 m (V_P = 1500 m/s, Table 3.2). The low quality of the dataset makes it challenging to ascertain the exact margin, and the rim of the depressions appears to be irregular in map view. Depressions D1, D4, D5 and D6 have an elongated shape with the longest axis striking NE – SW to E – W. Their longest axis measures 3.2 – 4.7 km while the shortest axis varies between 1.2 and 2.2 km. The depth is in the range of 15 – 20 m. Mega depressions D2 and D3 are significantly smaller than the others as their longest axis measure 1010 and 2190 m and the shortest axis 840 and 1270 m. D2 and D3 have a sub-circular shape where the longest axis is striking N – S to NW – SE, and have a depth of 10 m and 12 m (V_P = 1500 m/s), respectively. None of the mega depressions reach through the URU. Underlying N – S striking F2 fault and E – W striking F1 faults occur in proximity to the depressions. No amplitude anomalies along URU are observed below the mega depressions, and there are no indications of acoustic masking or pipe structures (Fig. 4.34b). Pockmark depressions have been identified at margins of depressions D1, D4 and D6 (Fig. 4.34a).

In the northern area, in the southern part of survey OMV09M01, four (D7 – D10) mega depressions are identified (Fig. 4.35). Being located within the Ingøydjupet, the mega depressions occur at a water depth of 330 – 390, slightly deeper than the mega depressions in the southern area (D1 – D6). In the northern area the mega depressions have an elongated shape where the longest axis is striking NW – SE. The longest axis of D7 and D8 measure approximately 3660 m and 2450 m, respectively, while the shortest

axis measure 790 m and 1010 m. The depth varies between 30 and 40 m (V_P = 1500 m/s) and changes along strike. A small pockmark depression is located between D7 and D8, and 11 pockmarks are separating D7 and D8 from D9 and D10 (Fig. 4.35). Mega depressions D9 and D10 are only partly covered by the seismic data and extend southwards out of the dataset, hence the exact measures are unattainable. D9 appears to be the largest one of the mega depressions as the long axis reach at least 6120 m and the short axis 1490 m. One small pockmark depression is identified inside D9. The depth of the mega depression is 30 – 40 m (V_P = 1500 m/s), similar to the other mega depressions. The seismic data only cover the northern part of D10, where the long axis measures at least 1260 m and the short axis 860 m. D10 stand out from the other depressions, both in the northern and southern area, as a prominent rim enclose the depression (Fig. 4.35a). The rim appears to be approximately 20 m (V_P = 1500 m/s) above the surrounding seabed and is 20 – 25 m wide. Three small depressions are observed on the northern part of the rim (Fig. 4.35).

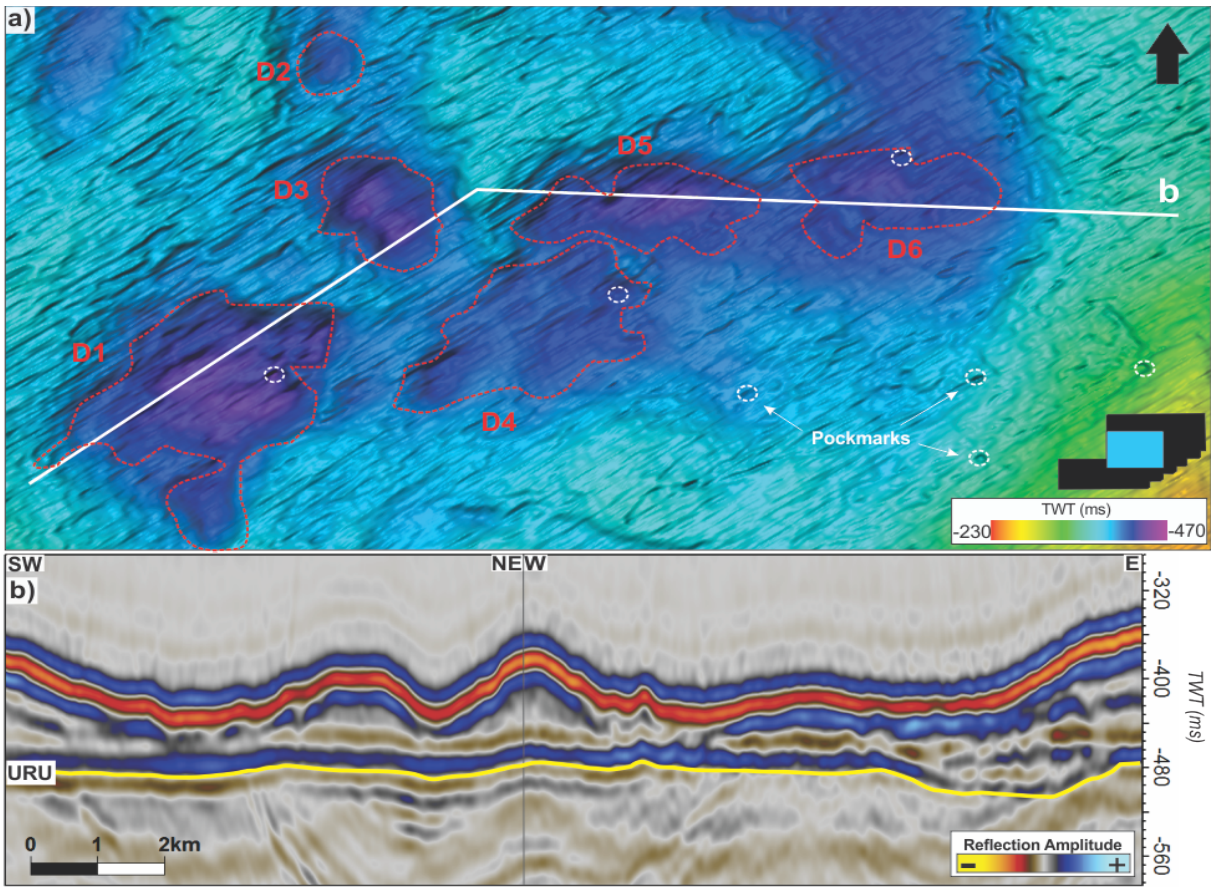

Fig. 4.34: ***a)*** *Overview of mega depressions (D1 – D6) and pockmarks. Position of map indicated in black polygon (survey DG0901) in lower right corner, whose position is indicated in Fig. 4.29.* ***b)*** *Seismic section through mega depressions showing that they are not linked to underlying faults or structures, or amplitude anomalies. Position indicated in* ***a****.*

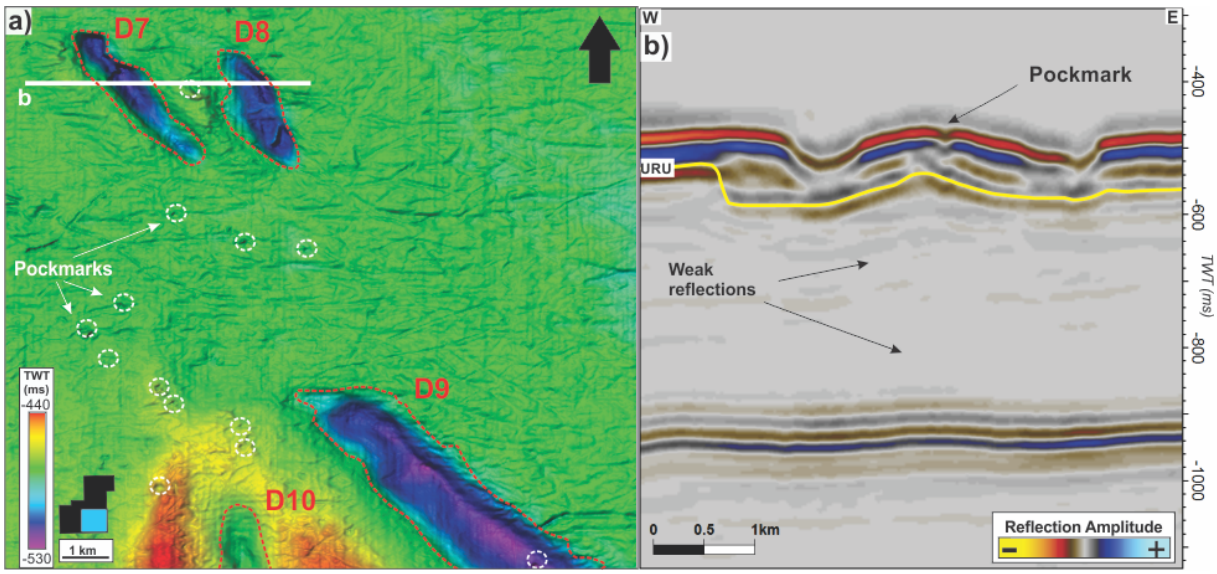

Fig. 4.35: ***a)*** *Overview of mega depressions (D7 – D10) and pockmarks on the seabed. Position of map is indicated in black polygon (survey OMV09M01) and in Fig. 4.29. D9 and D10 are only partly covered by the seismic data.* ***b)*** *E – W oriented seismic section through mega depressions D7 and D8, and small pockmark between them. Weak reflections beneath the mega depressions. Position is indicated in* ***a****.*

D7, D8 and D9 appear to have a V-shape where the easternmost sidewall is steeper than the western (Fig. 4.35b). D10 have nearly a U-shape where both the eastern sidewall appears to be only incrementally steeper than the western wall. All the mega depressions observed here extend through the upper regional unconformity, although the low seismic quality prevents from investigating the details below the URU (Fig. 4.35b), where no deep-seated faults are identified in the subsurface at this particular area.

Depression	***Long axis (m)***	***Short axis (m)***	***Short axis/ long axis***	***Area (km^2)***	***Depth (ms TWT)***	***Depth (m, V_P=1500m/s)***
D1	4730	2250	0.47	9.83	44	33
D2	1010	840	0.83	0.83	16.9	12.6
D3	2190	1270	0.58	2.65	26	19.5
D4	3710	1930	0.52	6.91	23	17.2
D5	3680	1380	0.37	4.74	20.8	15.6
D6	3200	1210	0.37	3.39	10.1	7.5
D7	3660	790	0.21	2.52	46	34.5
D8	2450	1010	0.41	2.28	39	36.7
D9	6120 ->	1490	-	-	41.6	31.2
D10	1260 ->	860	-	-	21.8	16.3

Table 4.5: Summarization of the mega depressions (D1 – D10) identified on the seabed.

4.5.2 Depressions on the URU: "Paleo pockmarks"

The interpreted URU (Fig. 4.3) reflection reveals a similar geomorphology as the seabed reflection. Randomly oriented iceberg plough marks are only occasionally identified within the study area (e.g. Fig. 4.37). They are commonly U- and V-shaped, and have a depth of 10 – 20 m, assuming a velocity of 1700 m/s in Nordland Group sediment (Table 3.2). The plough marks do not occur as frequently on the URU reflection as they do on the seabed. Mega-scale glacial lineations are observed on URU, having a NW – SE orientation, and are far more common than furrows. The mega-scale glacial lineations have similar shapes as the MSGLs on the seabed, although they occur less frequently, and can be traced up to 35 km.

Several circular to sub-circular depressions have been identified on the URU reflection, having similar shape and size as the pockmark depressions identified on the seabed. These are observed in all the seismic datasets and have been interpreted to represent paleo pockmarks (e.g. Judd and Hovland, 2007). Detailed mapping of paleo pockmarks reveal that the pockmark density is considerably higher in the western Hammerfest Basin than the eastern (Fig. 4.36). In total 482 paleo pockmarks have been identified, where 47 % occur within survey ST0306 and ST8320R00. They commonly occur in groups of 3 – 10, and on occasion they are observed in chains within iceberg plough marks (Fig. 4.37a). The depth of the paleo pockmarks appears to be relatively constant on the western Hammerfest Basin and varies between 5 and 23 m (V_P = 1700 m/s). Commonly the paleo pockmarks have an elongated shape where the longest axis measures 85 to 230 m, however, no preferred orientation of the long axis is observed. The majority of the paleo pockmarks have a V-shape where one sidewall is steeper than the others. The steep sidewall occurs on both the short and long walls.

The distribution of paleo pockmarks occur in proximity to the underlying faults and amplitude anomalies (Fig. 4.36). Close to the Loppa High and southwards in the western Hammerfest Basin, the majority of the paleo pockmarks occur directly above N – S and E – W striking deep-seated F1 and F2 faults. This is also observed in the eastern Hammerfest Basin within survey ST05M09.

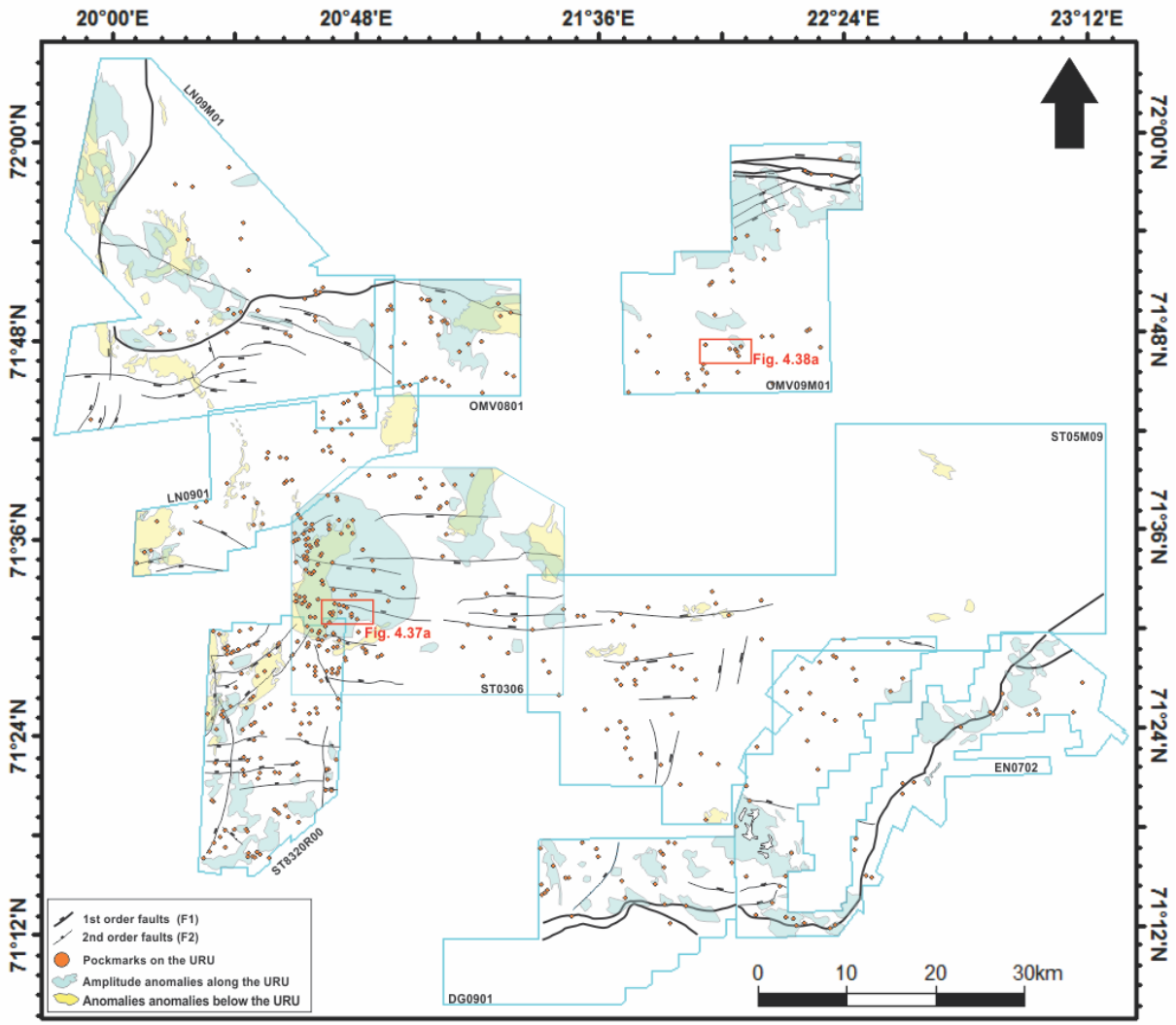

Fig. 4.36: Overview of paleo pockmarks (orange dots) identified on the interpreted URU reflection together with F1 and F2 faults and amplitude anomalies both along (blue) and below the URU (yellow).

A high number of paleo pockmarks are located directly above amplitude anomalies, both below and along the URU. Within survey ST0306 and ST8320R00, the areas where the highest concentration of paleo pockmarks occur (227), are located directly above amplitude anomaly A6 and A7. Acoustic masking and pipe structures are occasionally observed below the pockmarks. Interestingly the number of paleo pockmarks on the URU is significantly higher than the number of pockmarks on the seabed. Only occasionally seabed pockmarks locate directly above a paleo pockmark. Commonly a group of paleo pockmarks scatter beneath one single seabed pockmark.

In the northeastern Hammerfest Basin, in survey OMV09M01, the majority of the paleo pockmarks occur where no deep-seated faults are observed (Fig. 4.36). The paleo pockmarks in this area have an elongated to sub-circular shape and appear to have steep

sidewalls (Fig. 4.38). The longest axis, 130 – 270 m long, have a preferred orientation of NW – SE to E – W and the depth varies from 7 to 18 m (V_P = 1700 m/s). Similar to the western Hammerfest Basin, the number of paleo pockmarks is higher than seabed pockmarks above (Fig. 4.38c). The southeastern Hammerfest Basin, close to the Finnmark Platform, the paleo pockmarks appear to be randomly distributed as they both occur close to and distant to the underlying F1 and F2 faults. The pockmarks in this area share the characteristics of those in the western Hammerfest Basin, although they are not always located above underlying amplitude anomalies.

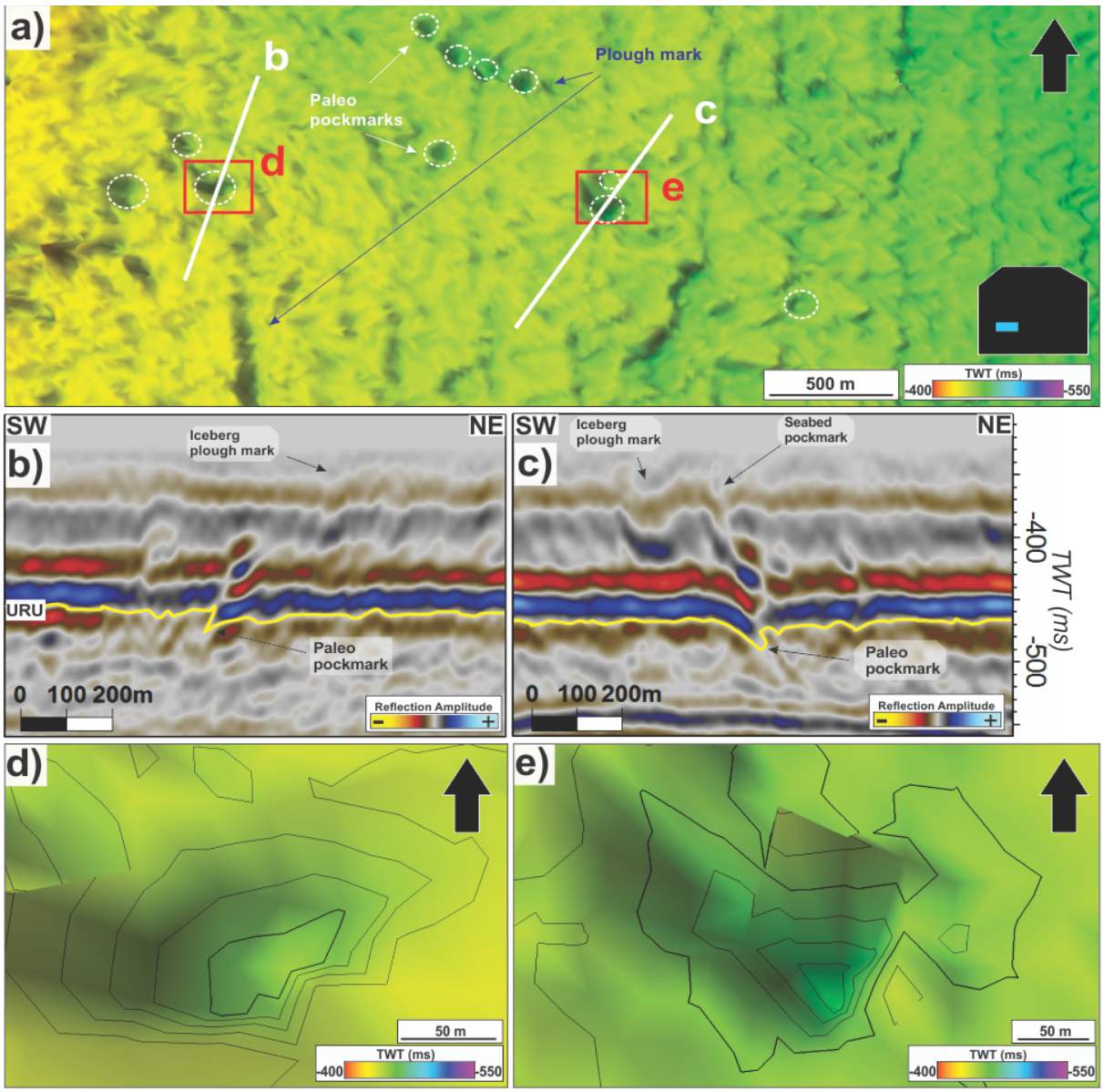

Fig. 4.37: ***a)*** *Overview of paleo pockmarks identified on the interpreted URU reflection. They occur both within and outside iceberg plough marks. Position is indicated in Fig. 4.36.* ***b & c)*** *Seismic section through paleo pockmarks, showing relationship to overlying seabed pockmarks. Position indicated in* ***a****.* ***d & e)*** *Close-up picture of paleo pockmarks, showing the V-shape and steep sidewalls. Position indicated in* ***a****.*

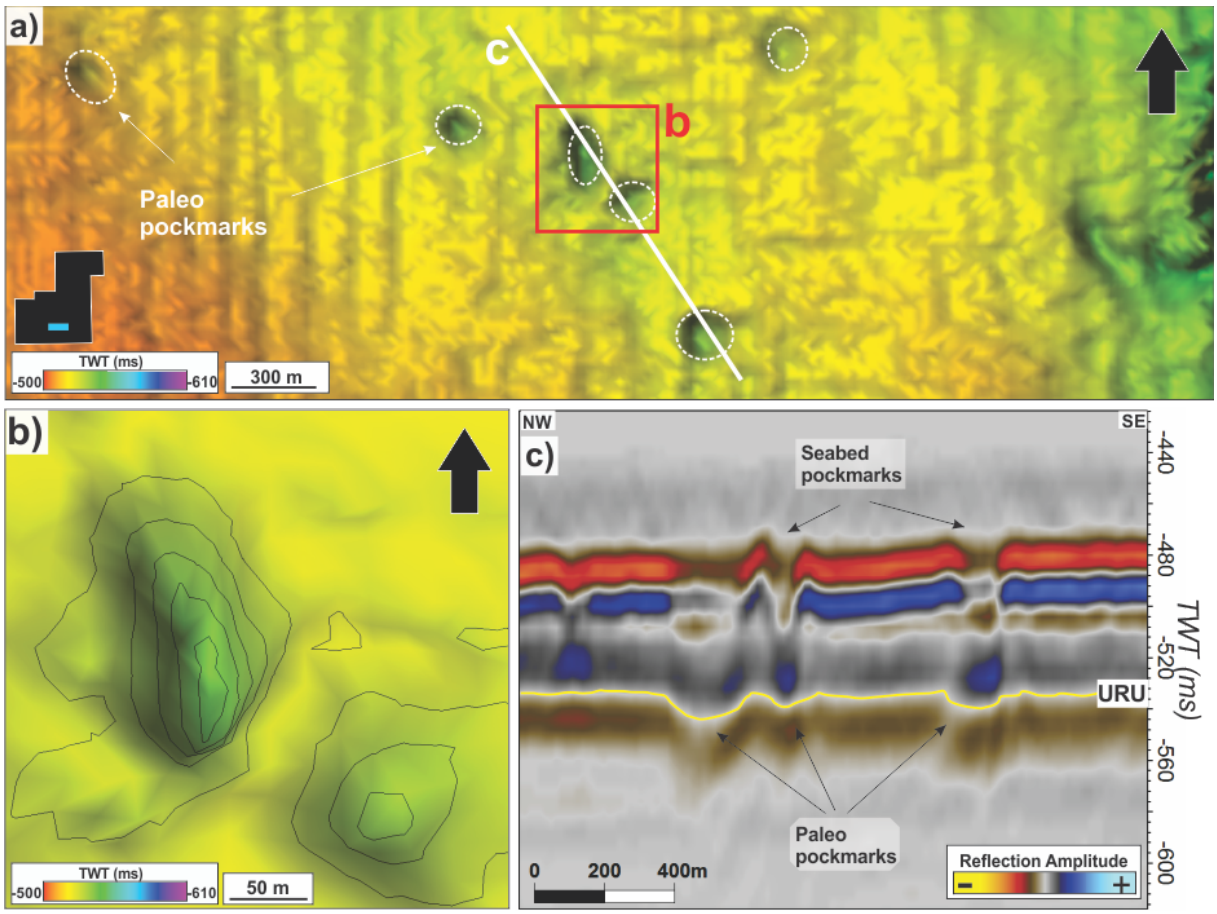

Fig. 4.38: ***a)*** *Overview of paleo pockmarks on the interpreted URU reflection. Position indicated in Fig. 4.36.* ***b)*** *Close-up picture of two paleo pockmarks, showing both the U- and V-shape. Position indicated in* ***a****.* ***c)*** *Seismic section through paleo pockmarks, showing the relationship to seabed pockmarks. Position of section indicated in* ***a****.*

5 Discussion

The results chapter presented the stratigraphy, fault distribution, amplitude anomalies and fluid flow features above the Base Cretaceous in the Hammerfest Basin. The focus of the discussions chapter is to integrate these observations aiming at a better understanding of the controlling mechanisms for the occurrence and development of large- and small-scale fault systems, and associated fluid migration, accumulation and release systems.

5.1 Faults

The southwestern Barents Sea has been affected by a series of tectonic phases dated all the way back to early Paleozoic times (Gabrielsen, 1984; Dorè, 1995; Larssen et al., 2005). Rifting and subsequent breakup in early Cenozoic has left a prominent imprint on the continental margin and created a comprehensive structural and stratigraphic framework (Rønnevik et al., 1982; Faleide et al., 1993; Faleide et al., 2008). The Hammerfest Basin, bounded by the Asterias Fault Complex and the Ringvassøy-Loppa Fault Complex to the north and west, respectively, and the Troms-Finnmark Fault Complex to the south, is an asymmetric basin that inherited its NE – SW striking axis from zones of weakness in the Caledonian basement (Faleide et al., 1984; Gabrielsen, 1984; Gabrielsen et al., 1990; Faleide et al., 1993).

In order to better understand the fluid leakage evolution, first the tectonic evolution, which is steering the fault developments, will be discussed here and integrated to existing tectonic knowledge of the Hammerfest Basin. The mapped faults presented in the results chapter were subdivided into deep-seated and shallow faults. The deep-seated were further divided into third (F3), second (F2) and first (F1) order faults based on the affected interval (Table 4.1). Based upon regional and tectonic significance, degree of basement involvement and reactivation, Gabrielsen (1984) introduced a classification of fault systems (Table 5.1) (Gabrielsen, 1984). The identified faults will be discussed in relation to this fault classification.

First class	Basement involved	Regional significance	Reactivated	Separate areas of different tectonic outline
Second class	Basement involved	Semi-regional	Reactivated/ not reactivated	Separate areas of different tectonic outline
Third class	Basement detached	Local significance	Not reactivated	Does not separate areas of different tectonic outline

Table 5.1: Classification of fault systems. The faults are divided into first, second and third class based on the degree of basement involvement and reactivation. Table from Gabrielsen (1984).

5.1.1 Activity of deep-seated faults

Several deep-seated faults are observed within the study area. The F1 faults observed at the northern and southern margin of the Hammerfest Basin are part of the Asterias Fault Complex and the Troms-Finnmark Fault Complex, respectively, and will not be discussed to the same extent as the F3 and F2 faults. The F1 fault that penetrates the URU in the northeastern Hammerfest Basin may indicate that the basin was tectonically active also after the onset of the glaciations in the Plio-Pleistocene (Knies et al., 2009).

The third order (F3) faults terminate below the top of the Kolmule Formation and occur primarily in the western and southern Hammerfest Basin. The F3 faults, having an E – W and NE – SW orientation, are not basement involved or linked to deeper structures. They are best defined in the Hekkingen and Knurr formations, while the limited fault throw and termination within the Lower Cretaceous strata indicate that little reactivation has occurred and that they are of little regional significance. They belong to the third class faults of Gabrielsen (1984). Initiation probably occurred in the Middle – Late Jurassic when the northward propagation of the Atlantic rifting led to a change in the extensional stress field, and the onset of the Kimmerian tectonic rift phase (Faleide et al., 1984; Faleide et al., 1993; Faleide et al., 2008). The F3 faults are linked to doming in the central Hammerfest Basin that occurred in response to movement along the Asterias and Troms-Finnmark Fault Complex to the north and south, respectively (Gabrielsen, 1984; Faleide et al., 1993; Ostanin et al., 2012). The high concentration of F3 fault along the southern basin margin follow the trend of the Troms-Finnmark Fault Complex, and may have been linked to this movement.

In the Early Cretaceous, between the Berriasian and the Barremian, rifting continued in the Hammerfest Basin (Faleide et al., 1993; Faleide et al., 2008; Ostanin et al., 2012). The majority of the F3 faults have displaced the Lower Cretaceous strata, where the displacement is constant for the Knurr and Kolje Formation, and lower than that of the Hekkingen Formation. This suggests that the faults were inactive during the deposition of these units and reactivated prior to the deposition of the Kolmule Formation, probably in the Barremian (Faleide et al., 1993). A small reactivation may have occurred in the early-phase deposition of the Kolmule Formation, in the Aptian or Albian, as evidenced by a small throw within the lower part of the formation.

The second order faults (F2) have three dominating orientation, N – S, NE – SW and E – W, and terminates at various levels within the Paleocene-Eocene Torsk Formation. The fact that they affect several stratigraphic intervals suggests that they have been active or reactivated multiple times since initiation, being classified as both first and second order faults of Gabrielsen (1984). The Cenozoic uplift and erosion of the Barents Sea complicates the process of determining the time of faulting within the Torsk Formation (Knutsen and Vorren, 1991; Reemst et al., 1994).

The N – S striking F2 faults, at the western margin of the Hammerfest Basin, are totally different than the faults oriented NE – SW and E – W, and are interpreted to be part of the Ringvassøy-Loppa Fault Complex that separates the Hammerfest Basin from the deeper Tromsø Basin in the west (Gabrielsen et al., 1990; Larssen et al., 2005; Indrevær et al., 2013). The faults appear to be basement involved and of regional significance, belonging to the first class faults of Gabrielsen (1984). The fact that the fault throw increase incrementally with depth, suggest that they have been active and reactivated multiple times, latest in the Paleocene-Eocene. The initiation of these faults probably occurred during the Kimmerian phase in the Middle – Late Jurassic when transtensional movement rifted along old zones of weakness in the Caledonian basement (Faleide et al., 1984; Faleide et al., 1993; Faleide et al., 2008). As evidenced by the high throw in the Knurr, Kolje, Kolmule and Kviting/Kveite Formations, this rifting continued into the Early and Late Cretaceous as the thermal subsidence in the Tromsø Basin were significantly higher than in the Hammerfest Basin (Faleide et al., 1993).

Renewed activity along the Ringvassøy-Loppa Fault Complex probably occurred in the Late Cretaceous – Paleocene when the opening of the Norwegian-Greenland Sea resulted in strike-slip movements along the De Geer Zone and deepening of the Tromsø Basin (Faleide et al., 1993; Faleide et al., 2008; Indrevær et al., 2013). The decreasing throw within the Paleocene-Eocene Torsk Formation, and the fact that none of the N – S striking faults reach the URU, indicates that the fault activity ceased toward the end of Eocene when the change from rifting to seabed spreading occurred (Linjordet and Grung-Olsen, 1992; Faleide et al., 1993; Faleide et al., 2008). This change developed the Barents Sea margin to a sheared margin, resulting in transtension across the Ringvassøy-Loppa Fault Complex, explaining the Eocene reactivation (Faleide et al., 1993; Faleide et al., 2008).

The E – W and NE – SW striking F2 faults have similar characteristics as the E – W striking F3 faults, as they are sub-parallel features with approximately the same strike length and dip direction toward the north and south. However, all the F2 faults have larger fault throw in the Hekkingen, Knurr and Kolje formations than the F3 faults, and reach younger stratigraphic levels, suggesting that reactivation occurred, hence classifying them as second class faults of Gabrielsen (1984). The rather constant throw in the Kolmule, Kviting/Kveite and the lower part of the Torsk Formation, for the F2 faults, indicates that the faults were inactive during the deposition of these units. Interestingly, the difference in displacement, in the Hekkingen, Knurr and Kolje formations between the F2 and F3 faults, is the same as the displacement in the Kolmule, Kviting/Kveite and Torsk formations of the F2 faults. This indicates that the F2 and F3 faults initiated at the same time, during the Kimmerian tectonic phase, and that the F2 fault were reactivated at a later stage in the Paleocene-Eocene, in the early-phase deposition of the Torsk Formation. A small reactivation in the Barremian and Aptian/Albian may have taken place together with the F3 faults. This phase of reactivation may have been linked to the tectonic readjustment related to the opening of the Norwegian – Greenland Sea in the Late Eocene (Knutsen and Vorren, 1991; Ostanin et al., 2012).

5.1.2 Shallow faults in relation to deep-seated faults

The shallow faults are confined to the Paleocene-Eocene Torsk Formation and do not affect the underlying Kviting/Kveite Formation. They are sealed below the URU, indicating that they occurred prior to the onset of the Plio-Pleistocene glaciations (Reemst et al., 1994; Faleide et al., 1996; Knies et al., 2009). Deep-seated faults can be linked to the formation of shallow faults (e.g. Hansen et al., 2004; Ostanin et al., 2012), and a comparison of the shallow faults with the deep-seated F2 faults is indicated in (Fig. 4.11 and Fig. 4.12). In the northwestern part of the Hammerfest Basin the shallow faults have the same curvilinear fault trace as the underlying F2 faults. However, the curvilinear shape continues southwards into survey LN0901, directly above a zone where no F2 faults are observed. In the centre of the Hammerfest Basin, the shallow faults are observed to have N – S, NE – SW and E – W orientations above N – S and E – W striking F2 faults. This suggests that a link between the shallow faults and the deep-seated faults exist, although the shallow faults are not completely controlled by the deep-seated faults. The development of the shallow faults probably occurred during the tectonic readjustments related to the opening of the Norwegian – Greenland Sea, at the same time as the E – W and NE – SW striking F2 faults were reactivated, in the Late Eocene (Knutsen and Vorren, 1991; Faleide et al., 1993; Faleide et al., 2008; Ostanin et al., 2012).

5.2 Fluid generation, migration and accumulation

Fluid migration within the southwestern Barents Sea has been documented by several authors (e.g. Martens, 2009; Chand et al., 2012; Ostanin et al., 2013; Rajan et al., 2013; Vadakkepuliyambatta et al., 2013). The results chapter presented features such as acoustic chimneys and amplitude anomalies that most likely are linked to fluid migration (gas chimney) and fluid accumulation (shallow gas in sediments). (Andreassen et al., 2007a; Rajan et al., 2013; Vadakkepuliyambatta et al., 2013). The mechanisms of generation, migration and accumulation of hydrocarbons within the study area will be discussed below.

5.2.1 Source of hydrocarbons

Based on the total organic content (TOC), hydrogen index (HI) and the hydrocarbon generative potential (S2), the source rock of best quality is the Upper Jurassic Hekkingen Formation (Fig. 2.4) (Dorè, 1995; Ohm et al., 2008). The Hekkingen Formation has good potential for both oil and gas and are present in the majority of the Hammerfest Basin (Linjordet and Grung-Olsen, 1992). Source rocks are also present in the Triassic, Permian and Carboniferous strata, although there lies a degree of uncertainty on the deeper formations (Dorè, 1995; Ohm et al., 2008). Fig. 5.1 illustrates that the Jurassic Hekkingen Formation and the Triassic Snadd, Kobbe, Klappmyss and Havert formations are currently in the oil window in the study area, however, the illustration is based on the maximum burial of the source rocks and does not necessarily represent the current state (Ohm et al., 2008). The Hekkingen Formation is overmature in the deep Tromsø Basin in the west, and progressively moves into the gas and oil window eastwards towards the Ringvassøy-Loppa Fault Complex and the Hammerfest Basin. The formation is eroded on the Loppa High and the Finnmark platform, and has not yet matured in the eastern part of the Hammerfest Basin (Ohm et al., 2008).

Since the Hekkingen Formation is currently generating oil in the Hammerfest Basin, one should think that the oil accumulations in this area originate from this formation (Ohm et al., 2008). However, the repeating phases of uplift and erosion has resulted in gas expansion, seal breaching and spilling of oil, leading to re-migration of oil into distal areas. The oil and gas generated in the deep Tromsø Basin may have migrated into the shallower Hammerfest Basin (Dorè, 1995; Dorè and Jensen, 1996; Ohm et al., 2008; Henriksen et al., 2011b). Wells in the Barents Sea have shown that the oil and gas in

single structures are not necessarily cogenetic, indicating that the existing gas has not been exsolved from the oil during pressure release (Linjordet and Grung-Olsen, 1992; Ohm et al., 2008). This suggests that the non-cogenetic gas has displaced, or diluted, the cogenetic gas at a later point when another source rock has been active (Ohm et al., 2008). Basin modelling and geochemical data has suggested that the main hydrocarbon accumulations in the Hammerfest Basin are generated by the Jurassic and Triassic source rocks. The modelling results in that the Askeladd, Albatross and Snøhvit fields in the western and central part of the basin, received oil and gas from relative close sources in the north and west, while a combination of long distance migration and local sources supplied the Goliat field in the southeast (Duran et al., 2013a). This suggests that the fluids that is observed in the eastern part of the study area are generated in distal areas.

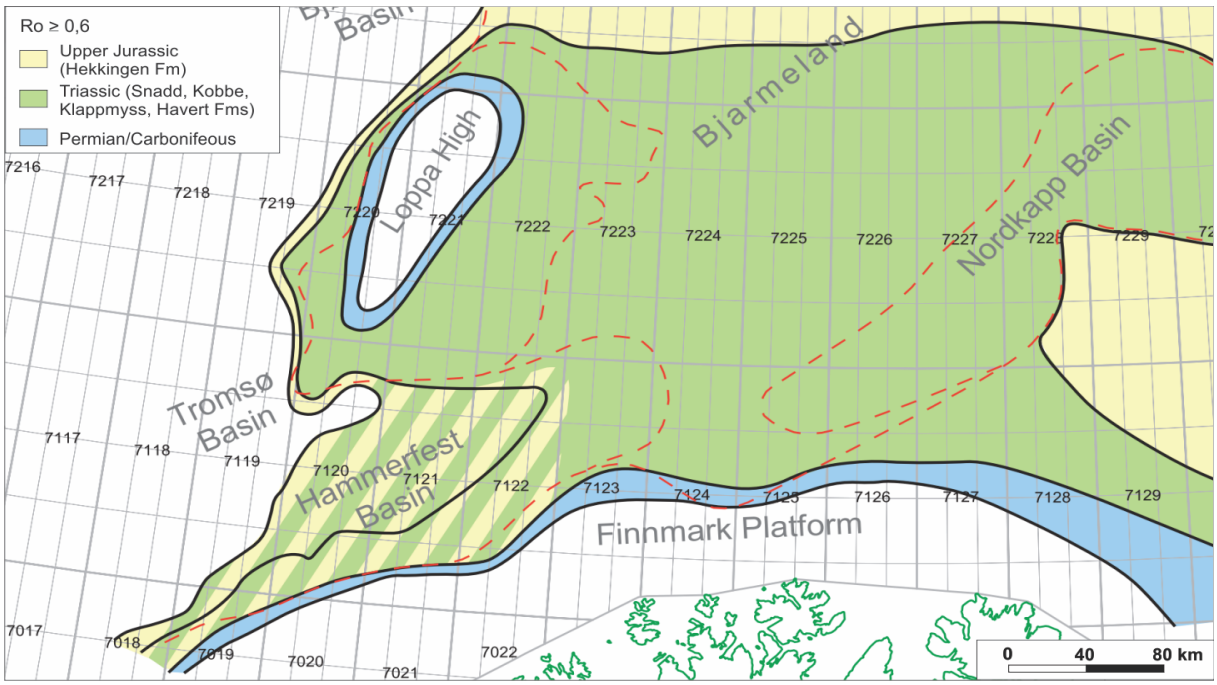

Fig. 5.1: Maturity map from the southwestern Barents Sea suggesting where the Permian, Triassic, and Jurassic source rocks are oil mature. Maturity map is based on maturity data from wells, depth maps and maturity trends. Figure is modified from Ohm et al. (2008).

It is likely that the shallow gas accumulations identified by seismic methods within the study area have migrated from both local and distal sources. The complex geologic history of the southwestern Barents Sea have probably led to migration and remigration of hydrocarbons, making it challenging to conclusively determine the source of the accumulations. For the accumulations in the study area, it is most likely that they consist of hydrocarbons originating from one or several sources within or along the margins of the Hammerfest Basin (Ohm et al., 2008; Henriksen et al., 2011b; Duran et al., 2013a).

5.2.2 Fluid migration and accumulation

The seismic data revealed several fluid flow indicators in the study area. The amplitude anomalies that were described in the results chapter commonly occur in proximity to faults, acoustic chimneys, pipe structures, zones of acoustic masking and where clinoforms are truncated by the URU (Løseth et al., 2009).

5.2.2.1 Vertical fluid migration along chimneys

Acoustic chimneys (C1 – C7) were identified within the northwestern and central part of the study area (Fig. 4.13). The deteriorated seismic signal suggests that the seismic chimneys reflect sediments with inhomogeneous gas saturation, representing leakage pathways for ascending free gas (gas chimneys) (Ligtenberg, 2005; Arntsen et al., 2007; Løseth et al., 2009). A shallow gas accumulation could attenuate the seismic signal and result in a vertical wipe-out zone below (e.g. Arntsen et al., 2007), however, the high vertical extent of the chimneys and the pull-down of seismic reflections within and beneath the chimney structures suggests that the chimneys in the study area represents leakage pathways. The low seismic velocity of gas-bearing sediment delays the arrival of the returning p-wave, hence producing a pull-down of the seismic reflections (Judd and Hovland, 1992). The pull-down increases with depth and may indicate that the sediment is gas charged over a long vertical extent, as the arrival is more and more delayed.

Gas chimneys C1 – C4 occur in the northwestern part of the study area, on the southwestern edge of the Loppa High, where the lower termination of the acoustic masking is located between 1800 and 2300 ms (TWT) in the Triassic and Permian strata (Table 4.3). The lower termination of the distorted seismic signal is vital to understand their source and origin, however the gas charged sediments attenuates the seismic energy so that the zone of acoustic masking may extend underneath that of the gas, indicating a deeper source (Judd and Hovland, 1992; Løseth et al., 2009; Rajan et al., 2013). As discussed above in Source of hydrocarbons (chapter 5.2.1), the Jurassic Hekkingen Formation is not present on the Loppa High while the Permian sources are commonly overmature and only producing gas in a narrow zone northward of the study area (Ohm et al., 2008). This suggests that the hydrocarbons in this area have a source of Triassic age, probably the Kobbe Formation (Ohm et al., 2008; Rajan et al., 2013). The gas is most likely generated in proximity to the chimneys, however vertical and lateral remigration from a deeper reservoir trough permeable faults and carrier beds is

possible. Gas chimneys commonly occur in areas of high strain, which the Loppa High and Hammerfest Basin is, resulting in seal failure or spilling (Ligtenberg and Connolly, 2003; Rajan et al., 2013).

Gas chimneys C5 – C7 occur in the central part of the Hammerfest Basin where the lower termination of the zone of acoustic masking occur between 2000 and 2100 ms (TWT) (Fig. 4.13) (Table 4.3), coinciding with the Jurassic Hekkingen Formation. As previously discussed the Hekkingen Formation is currently generating oil within the Hammerfest Basin, suggesting that the gas in C5, C6 and C7 have a pre-Jurassic origin, similar to C1 – C4. Jurassic gas is currently being generated westwards into the Ringvassøy-Loppa Fault Complex and Tromsø Basin, however, as this margin is highly faulted, vertical migration of gas is thought to take place along faults, not reaching the central Hammerfest Basin.

The upper termination of the chimneys occurs within middle to upper part of the Torsk Formation where high amplitude anomalies are located directly above the chimney structures (Fig. 4.13). The presence of bright spots above the chimneys indicates that there is a change in fluids, from brine to hydrocarbons, and that gas is allowed to accumulate below a barrier of low vertical permeability (Ligtenberg, 2005). The impervious barrier, prevents the hydrocarbons from reaching shallower levels and may lead the migration shift from vertical to lateral (Judd and Hovland, 1992; Løseth et al., 2009). This is supported by the fact that the horizontal extent of the amplitude anomalies are higher than the underlying chimney (Fig. 4.13), indicating that once the gas has reached the barrier, it is displaced laterally due to the constant supply of gas from below.

The occurrence of the acoustic chimneys appear to be controlled by the underlying faults. Along the Loppa High they occur directly above the E – W striking F1 faults, and in the Hammerfest Basin above the deep-seated F2 faults and where these intersects with the NE – SW striking F3 faults (Fig. 4.13). Fault intersections are known to act as potential leakage zones (e.g. Gartrell et al., 2004), and are proposed to control the gas-water contacts in drilled structures in the Hammerfest Basin (Hermanrud et al., 2014). The NE – SW striking F3 faults and prominent fault intersections in general are not identified within the southern and eastern part of the basin (Fig. 4.4), while the number of E – W striking F2 faults is low, and may explain the lack of gas chimneys in these

areas. As the amplitude anomalies are confined to the Torsk Formation, it is likely that the gas chimneys formed after the Paleocene – Eocene. If the fluids are leaking or remigrating from a deeper reservoir, as already mentioned, the onset of the Plio-Pleistocene glaciations appear as the most likely time of initiation. The uplift and tilting of the continental margin may have resulted in reactivation of deep-seated faults that have worked as conduits for leakage. The western part of the Hammerfest Basin is more faulted than the eastern, and may explain why the gas chimneys are confined to this region (Rajan et al., 2013; Vadakkepuliyambatta et al., 2013).

5.2.2.2 Vertical fluid migration along faults

Vertical migration of fluids is known to occur along faults and fault zones as they can represent fluid conduits across a sealing sequence (Fig. 5.2) (Wiprut and Zoback, 2000; Cartwright et al., 2007). If a fault is sealing or leaking is a critical point in the oil and gas industry as it may determine whether a structure is dry or filled by hydrocarbons (Ligtenberg, 2005; Hermanrud et al., 2014). Deep-seated and shallow faults were presented in the results chapter (chapter 4.2) and occur frequently within the study area, where the highest concentration is in the western part of the basin. Leakage along faults is a complicated process as it is affected by several factors. Ligtenberg (2005) argued that migration along individual faults occurred along zones of weakness within the fault zone, and not along the entire fault plane. Weaknesses such as irregularities on the fault plane, intersections with other faults and small-scale features associated with the faults, would allow the migrating fluid to have subtle columnar flow patterns (Hindle, 1997; Knipe et al., 1998; Ligtenberg, 2005). Sealing faults filled with impermeable clay and/or cement could start leaking if the fluid pressures reach a certain value (Roberts and Nunn, 1995; Løseth et al., 2009).

Fluid flow along faults appears to be relatively common within the Hammerfest Basin, as acoustic masking is observed along the majority of the deep-seated F1 and F2 faults (e.g. Fig. 4.18 and Fig. 4.19). Enhanced seismic reflections are observed in the strata adjacent to the fault plane, indicating that migration of gas is taking place, or used to, along the faults, where the migrating gas has encountered permeable beds at the sides of the fault (Fig. 5.2) (Løseth et al., 2009). Amplitude anomalies are observed at several stratigraphic levels directly above, or in proximity, to the upper termination of the F1

and F2 faults, suggesting that these faults has been acting as conduits for migrating gas. One anomaly (A3) (Fig. 4.17) is located above NE – SW striking F3 faults (Fig. 4.14), suggesting that also these faults have, to some degree, been acting as migration paths from deeper levels.

In the central and northern part of the Hammerfest Basin the amplitude anomalies (below the URU) are generally located above the E – W trending faults (Fig. 4.14), suggesting that this fault trend is more prone to leakage than the N – S and NE – SW trending. This is supported by the fact that the lower zone of the distorted seismic signal of the gas chimneys, as already discussed, often coincide with the E – W striking F2 faults (Fig. 4.13a). Anomaly A6 and A7 (Fig. 4.20 and Fig. 4.21) at the western margin of the basin, are located above N – S and NE – SW trending faults, however these occur in an area where many of the deep-seated faults intersect, and the migration may have taken place along those intersections rather than the faults itself (Ligtenberg, 2005; Eichhubl et al., 2009).

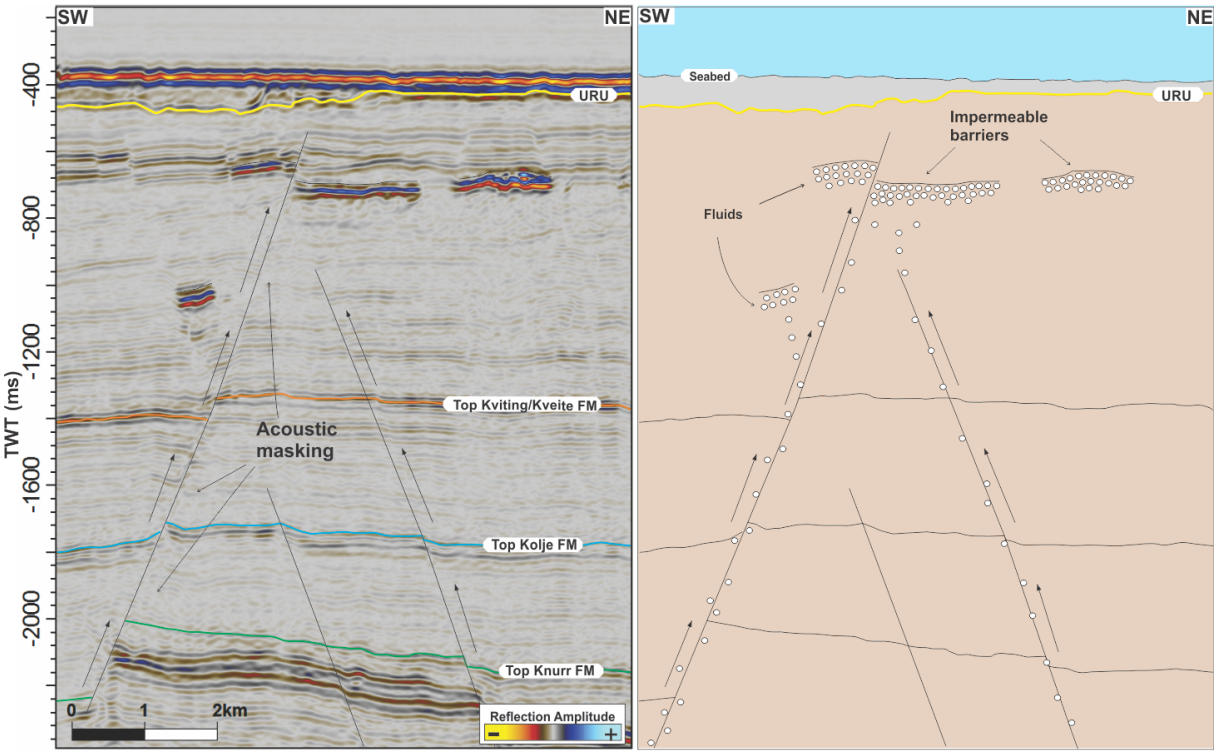

Fig. 5.2: Model of vertical fluid migration along faults ending in accumulation (Amplitude anomaly A4) within the Torsk Formation. Fluids migrate along the faults planes where zones of acoustic masking is observed in proximity to the faults.

The amplitude anomalies that were identified along the URU, occur more frequently than the amplitude anomalies below. Some of the URU anomalies are probably caused by lateral migration within the Torsk Formation (discussed next), however, as many of

the URU anomalies are located directly above deeper anomalies, it is likely that the shallow faults link the two. The shallow faults may act as conduits that allow the gas to remigrate from accumulations in the Torsk Formation up to the URU. The URU anomalies have a higher lateral extent than those below, suggesting that the URU, on occasion, represent an impermeable barrier (Martens, 2009; Rajan et al., 2013), so that the fluid migration shift from vertical to horizontal once it reach the surface. Enhanced amplitudes and acoustic masking is not observed in association with the shallow faults, although this is probably down to the resolution of the seismic data rather than the absence of gas.

Ostanin et al. (2012) argued that the N – S trending faults were leaking and the E – W trending sealing above the Snøhvit gas field during the Albian in the Lower Cretaceous, as the axis of maximum horizontal stress were oriented N – S in the Hammerfest Basin. A change in orientation of the stress axis in the Paleocene-Eocene, probably related to the opening of the Norwegian – Greenland Sea, sealed the N – S trending faults and opened the E – W trending (Ostanin et al., 2012). This can explain why the majority of the amplitude anomalies and chimneys within the study area are located above these fault and confined to the Paleocene-Eocene Torsk Formation (Fig. 4.14). The opening of the Norwegian – Greenland Sea resulted in uplift and erosion of the shelf, where fault reactivation and tilting of deep reservoirs led to fluid migration primarily along the E – W striking F2 faults (Dorè and Jensen, 1996; Ostanin et al., 2012; Hermanrud et al., 2014). The shallow faults, initiated in this period, were probably helping the deep-seated faults to transmit fluids to shallower levels, possible up to the paleo seabed. All the F1 and F2 faults extend down to the Triassic and Permian strata, suggesting that the fluids that have been migrating along the faults have had a pre-Jurassic origin (Linjordet and Grung-Olsen, 1992; Ostanin et al., 2012).

5.2.2.3 Lateral fluid migration along clinoforms

Amplitude anomalies in the study area are observed to occur along clinoforms of the Torsk Formation. The clinoform reflection configurations probably represent the south – southwesterly progradation of sediments into a standing body of water during a transgression in the Eocene – Miocene (Vorren et al., 1991; Veeken, 2007). The sediments were eroded from the Loppa High and the Finnmark Platform and shed into

the Hammerfest Basin (Knutsen and Vorren, 1991). Fluid migration along such clinoforms has previously been proposed by Kristensen (2010) and Martens (2009) and is likely to represent a common mechanism of migration in the southwestern Barents Sea.

The Cenozoic succession comprises horizons of silt- and claystones and occasionally sandstone (Vorren et al., 1991), suggesting that the permeable and porous sandstone may act as migration pathways for the migrating gas. The siltstone and claystone may represent impermeable barriers that prevent the gas from leaking vertical directly to the seabed. The clinoforms within the western and central part of the Hammerfest Basin occasionally have anomalous strong amplitudes that can be traced down to the lower part of the Torsk Formation. The upper termination of these high amplitude reflections occurs in proximity to amplitude anomalies A1, A4, A8 and A9, in addition to a selection of anomalies along the URU (Fig. 4.25 and Fig. 4.28). The shape of A1 (Fig. 4.15) and A4 (Fig. 4.18) mimic that of the clinoforms, suggesting that they contain gas charged from the dipping layers in addition to deep-seated faults. In the northeastern and southern part of the Hammerfest Basin there is not observed high amplitudes within the clinoforms, although amplitude anomalies are observed along the URU. As no deep-seated or shallow faults can justify the presence of anomalies, migration is likely to occur along these clinoforms.

The steepness of the clinoforms may affect the distance the fluid can migrate. If the clinoforms have a gentle dip the fluids is likely to migrate over longer distances, while steep dips suggests shorter distances. The steepness in the western part of the Hammerfest Basin is distinctly higher than the eastern, suggesting that the Torsk Formation in the west is charged from relatively proximal sources. As the western margin is highly faulted, the deep-seated F1 and F2 faults may act as excellent migration pathways for gas into the clinoforms in this area. The gentle dip of the clinoforms in the eastern part of the Hammerfest Basin may explain the occurrence of amplitude anomalies in this area when the number of deep-seated faults is so low, as the gas most likely have migrated from the more faulted area in the west.

5.2.3 Fluid accumulation mechanism

The amplitude anomalies and the termination of the gas chimneys occur within the Kviting/Kveite Formation, Torsk Formation and along the URU, and suggest that impermeable barriers exists at several stratigraphic levels within the study area, preventing fluids from reaching shallower levels.

The majority of the amplitude anomalies in the Torsk Formation crosscut the south – southwesterly dipping clinoforms and appears to be relatively parallel to the seabed reflection. Similar anomalies, commonly called bottom-simulated reflectors (BSR), have previously been described in the southwestern Barents Sea and the Hammerfest Basin (e.g. Chand et al., 2008; Kristensen, 2010; Chand et al., 2012; Ostanin et al., 2013; Rajan et al., 2013; Arvo, 2014), and most likely represent the transition between gas hydrates and the underlying free gas, and mark the lower boundary of the gas hydrate stability zone (GHSZ) (Shipley et al., 1979; Bünz and Mienert, 2004). Gas hydrates are stable given the correct temperatures and pressures, and are affected by the geothermal gradient, water bottom temperatures, water depth, water salinity and the composition and charge of the hydrocarbon gases (Clennell et al., 1999). Accumulation of gas below the hydrate layer is common, given the correct conditions, as the hydrates represents an impermeable barrier (Grauls, 2001). Pipe structures and acoustic masking occur below the BSRs in the study area, which suggests that free gas is present.

The presence of gas hydrates and their stability field depth has been documented and calculated in the Barents Sea by several authors (e.g. Chand et al., 2008; Martens, 2009; Ostanin et al., 2013; Arvo, 2014), and are believed to have been influenced by the glacial – interglacial cycles in the Cenozoic. Pressure changes due to glacial loading and unloading and erosion, in addition to fluctuations in sea level and water bottom temperatures, have all affected the stability conditions of the gas hydrates (Mienert et al., 2000; Mienert et al., 2005). The Cenozoic gas expansion and reservoir tilting due to the onset of the glaciations probably allowed gas to migrate along faults, chimneys and permeable carrier beds up to the base of the GHSZ and develop gas hydrates (Laberg and Andreassen, 1996). The effect of the glacial erosion and seabed subsidence resulted in an increase in the GHSZ and caused the gas hydrate layer to grow and thicken in the study area during the Last Glacial Maximum (LGM) (Laberg et al., 1998).

The temperature and pressure conditions in the Barents Sea have changed since the LGM and has allowed hydrates to decompose, releasing significant amounts of free gas (Ostanin et al., 2013). Chand et al. (2008) argued that gas hydrates of structure II (Sloan, 1998) could be present and stable within the Barents Sea, having a stability thickness of 50 – 900 m depending on the composition of the hydrocarbon gases. The amplitude anomalies in the Torsk Formation occur approximately 25 – 290 m below seabed at water depths of 240 – 430 m, and coincide with the GHSZ calculated by Chand et al. (2008), suggesting that these represent free gas accumulations below gas hydrates.

The local variations in depth and shape of the amplitude anomalies (Table 4.4) and the tilted nature of anomaly A1 (Fig. 4.15) suggest that the hydrates in the study area are affected by local changes in geothermal gradient and gas composition. Rajan et al. (2013) identified a tilted BSR, similar to A1, on the western margin of the Loppa High and argued that migration of warmer fluids occurred in localized zones that resulted in variations in the geothermal gradient, hence a tilting of the GHSZ. A similar model could explain the occurrence of A1 and the other anomalies where warm fluids ascend from deep-seated F2 faults, resulting in a lateral change in the temperature gradient.

Amplitude anomalies A2 and A3 (Fig. 4.16 and Fig. 4.17) that were identified within the Kviting/Kveite Formation are not related to gas hydrates as they are buried below the GHSZ, and indicates that an impermeable barrier exist in the transition between the Kviting/Kveite Formation and overlying Torsk Formation. Lithology changes could explain the occurrence of anomalies at this depth, however, as the anomalies have negative reflection coefficients and is associated with deep-seated faults, accumulation of gas is the most likely scenario.

The URU occur above the base of the GHSZ, suggesting that the shallow gas accumulations that locates along this surface are trapped by a lithological barrier rather than impermeable gas hydrates, however, tuning of the seismic amplitudes due to the thinning beds of the Torsk Formation should not be overlooked (e.g. Brown, 2004). Free gas located below the gas hydrates may have migrated along faults and fractures through the gas hydrates before eventually being trapped below the URU. This explains why many amplitude anomalies along the URU occur directly above deeper anomalies

(Fig. 4.24). Fig. 4.24 clearly indicates that the number of amplitude anomalies along the URU is higher in the western area than in the eastern. As already stated, the lack of deep-seated F2 faults in this area are partly to blame, however, the thickness of the Nordland Group sediments thins toward the eastern Hammerfest Basin (chapter 4.1.1) and could potentially reduce the sealing capacity of the URU, resulting in fewer shallow gas accumulations in this area (Fig. 5.3). The ascending gas could, in areas where the thickness of the glacigenic sediments is scarce, be released directly into the water column (Fig. 5.3).

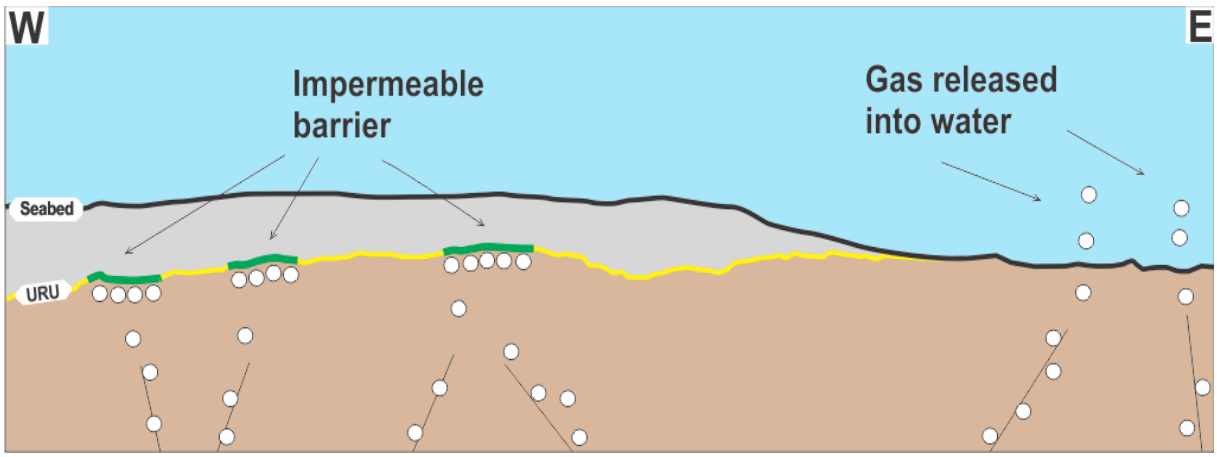

Fig. 5.3: Model for accumulation along the upper regional unconformity (URU) across the Hammerfest Basin. The impermeable Nordland Group sediments allows the gas to accumulate below the unconformity, while the absence of these sediments in the eastern part of the basin could potentially release the gas into the water column.

5.3 Seabed and URU depressions

Several depressions were identified on the seabed and URU. In the following chapter pockmarks and mega depressions will be discussed and linked to fluid flow and glacigenic processes.

5.3.1 Pockmarks

The pockmark depressions occur frequently on both the seabed and the URU, and have been identified in all the seismic datasets used in this study. The circular to sub-circular depressions appear to be common features within the Hammerfest Basin.

5.3.1.1 Origin

A variety of mechanisms can have created the pockmarks within the study area. The southwestern Barents Sea has undergone several phases of uplift and erosion since the onset of the glaciations in the Plio-Pleistocene (Andreassen et al., 2004; Knies et al., 2009). The appearance of elongate U- and V-shaped iceberg plough marks and mega-scale glacial lineations, shows that the glaciers and detached icebergs had the ability to alter the seabed and produce both small- and large-scale features. The circular to sub-circular depressions in the study area, that were interpreted to represent pockmarks, are similar to the iceberg plough marks in terms of depth and width, not in length. Icebergs that are transported by winds and currents could create sub-circular depressions when their keels occasionally hit the seabed (Woodworth-Lynas et al., 1985; Barnes et al., 1988), however, such an impact would likely result in a positive berm around the depression (Woodworth-Lynas et al., 1991) which is not observed within the study area, excluding a glacigenic origin. Several authors have suggested that pockmarks is a result of focused fluid flow (Berndt, 2005; Judd and Hovland, 2007), and this is the most likely explanation of their occurrence within the Hammerfest Basin. The depressions on the URU, that were interpreted to represent paleo pockmarks, are likely to have a similar origin where the venting of fluids have ceased (e.g. Long, 1992; Judd and Hovland, 2007). However, as the depressions on the URU are not as apparent in the seismic as those on the seabed, there is an uncertainty to their origin. It is not possible to rule out a glacigenic origin for some of the paleo pockmarks.

Although the pockmarks probably are a product of focused fluid flow, the mechanism of formation could be many. Escape of pore water was suggested for the formation of

pockmarks by Harrington (1985). He discovered that no pockmarks occurred in areas where mass movement had occurred, and proposed that the formation of pockmarks was an opportunity for releasing pore fluids when the slope was too gentle for mass movement to occur (Harrington, 1985). This mechanism does not explain the appearance of acoustic masking and pipe structures below the pockmarks within the study area. Paull et al. (1999) proposed a mechanism involving freshwater ice rafting on high latitude shelves, when seeping freshwater freezes at the sediment-water interface when the bottom waters are below 0°C. The frozen water would still be buoyant containing small amounts of sediments, and over time this would apparently excavating a depression (Paull et al., 1999). Freshwater could exist in offshore areas, as in Eckernförde Bay in Germany where water trapped within glacigenic sediments episodically are discharged (Whiticar, 2002). However, this is not a likely scenario in the Hammerfest Basin where the glacigenic sediments is of limited thickness and pockmarks occur on areas where the glacigenic sediments are absent. Freshwater flow along permeable carrier beds from land has been observed in the Baltic Sea (Whiticar and Werner, 1981), but also this is unlikely due to the long distance from land.

The most likely explanation for the occurrence of pockmarks in the study area is the expulsion of gas that has been generated during thermogenic and biogenic breakdown of organic material in the subsurface (Hovland, 1981; Hovland, 1982; Judd et al., 2002). The leaking of gas through the seabed may occur as a constant flow or as sudden violent release, where the seabed sediments is transported by the ascending fluids and distributed in the surrounding water column or seabed (Hovland et al., 2005; Judd and Hovland, 2007). Pockmarks most commonly develop in areas where the type of seabed sediment is fine-grained, while the thickness of the sediment control the distribution, size and depth of the depressions (Chand et al., 2009). Solheim and Elverhøi (1985) argued that biogenic decay of organic matter in the sediments above the bedrock produced insufficient amounts of gas to create pockmarks. The low carbon content (1 – 2 %) in addition to the scarce thickness of the glacigenic sediments suggested a thermogenic origin of the gas. Sources generating hydrocarbons within the study area have already been discussed (chapter 5.2.1) and the presence of gas within the Hammerfest Basin and southwestern Barents Sea suggests that expulsion of thermogenic gas is the most likely mechanism of development.

5.3.1.2 Pockmark appearance and distribution

The occurrence of pockmarks on both the URU and the seabed suggests that focused fluid flow has occurred at least from the onset of the glaciations to the present day. The shape and appearance of the pockmarks vary across the study area, being circular to elongate in plan view, with one sidewall steeper than the others. The elongate shape of the depressions is not a product of underlying structures, and most likely indicate that they have been influenced by strong bottom currents (Hovland et al., 2002), which is not unlikely in the southwestern Barents Sea (Bellec et al., 2008). Slumping confined to one side is probably the cause of the asymmetric appearance (Judd and Hovland, 2007).

Primarily in the western and central part of the study area the number of URU pockmarks exceeds the number of seabed pockmarks (Fig. 4.29 and Fig. 4.36), and represent at least two separate phases of fluid escape (Ostanin et al., 2013). Some places the seabed pockmarks occur directly above the URU pockmarks, suggesting that fluid leakage during the second phase occurred at the same location and possibly used the same conduits. Burial of the URU pockmarks indicates that the fluid flow ceased before the deposition of the Quaternary sediments (Ostanin et al., 2013). The pipe structures, pull-downs and acoustic masking that were occasionally observed beneath some of the seabed pockmarks may evidence that leakage has occurred in recent times or is currently ongoing (Heggland, 1997; Løseth et al., 2009).

It is challenging to differentiate between pockmarks that is formed by leakage along faults and those who are not. Faults, gas chimneys and clinoforms all represent potentially leakage pathways for the thermogenically derived gas, and they are well-represented in the study area (Hovland et al., 1993). Pockmarks occurring in chains and strings has been suggested to be a result of fault leakage (Hovland et al., 2002), and are observed on a few occasions along the western margin (Fig. 4.32 and Fig. 4.37). A high number of seabed and URU pockmarks appear to coincide with underlying F1 and F2 faults (Fig. 4.29b and Fig. 4.36), where the majority of the pockmarks occur above the E – W and NE – SW striking faults. Pockmarks are observed above the N – S striking faults on occasions, however, the faults oriented E – W and NE – SW appear to be favoured for fluid migration.

The high number of amplitude anomalies in the Torsk Formation, most likely representing free gas accumulated below gas hydrates (chapter 5.2.3), in addition to the anomalies located along URU, appear to be linked to the distribution of pockmarks on both the seabed and the URU (Fig. 4.29 and Fig. 4.36). As the gas hydrates represent impermeable barriers, pockmarks should normally not be caused by fluid flow from such features. However, it is likely that the shallow faults that are observed to penetrate the hydrate layers, act as migration pathways for the free gas below the GHSZ (Fig. 5.4). This mechanism potentially explain how migration from hydrate layers occur today. Once the gas has leaked through the gas hydrates it is free to ascend to the seabed. It is remarkable that not all the pockmarks occur directly above the amplitude anomalies as they are spread out on a larger area enclosing the anomalies. This suggests that also other mechanisms is allowing gas to flow from the hydrate layer. The clinoforms in the Torsk Formation probably act as migration pathways, allowing gas to flow laterally, and explain why pockmark occur several kilometres away from amplitude anomalies (Fig. 5.4).

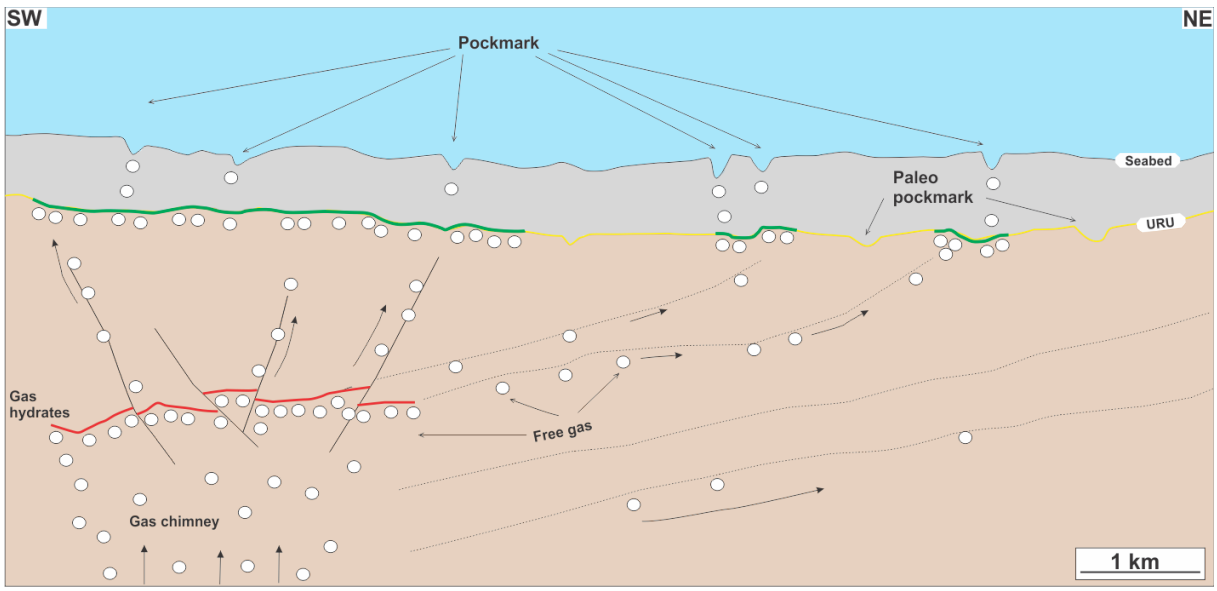

Fig. 5.4: Schematic model of pockmark formation on both the seabed and the URU. Free gas is allowed to accumulate below gas hydrates (in this case amplitude anomaly A8). Remigration occur laterally along clinoforms in the Torsk Formation and vertically along shallow faults that penetrate the hydrate layer.

The formation of pockmarks on both the seabed and the URU could potentially be linked to the decomposition of gas hydrates, which has been influenced by the pressure and temperature fluctuations during glacial-interglacial cycles (Solheim and Elverhøi, 1993; Cavanagh et al., 2006). Ostanin et al. (2013) proposed that the formation of seabed

pockmarks in the central Hammerfest Basin were related to the loading by a marine ice sheet during the LGM, which allowed gas hydrates to form due to the increased pressure and reduced temperature. During the deglaciation when the ice sheet retreated, the increase in temperature and reducing pressure may have resulted in an upward shift of the GHSZ and destabilization of the gas hydrates, resulting in more gas to accumulate below the thinning hydrate layer. When the thickness of the seal and the gas pressure below reached a critical value, the free gas were allowed to migrate upwards and created the pockmarks (Solheim and Elverhøi, 1993; Ostanin et al., 2013). The deep-seated faults in the study area were probably acting as migration pathways for thermogenic gas, which in turn allowed gas hydrates to form in response to the pressure and temperature conditions given by the ice sheet, suggesting that this mechanism of pockmark formation has been dominant within the entire Hammerfest Basin.

It is challenging to determine the occurrence of pockmarks in the eastern Hammerfest Basin due to the limited data coverage and the low quality of the datasets. The low number of faults and amplitude anomalies in the subsurface is in contrast with the high number of pockmarks on both the URU and the seabed (Fig. 4.29 and Fig. 4.36). The low number of faults suggest that the gas have migrated laterally along the clinoforms from the western margin. However, deep-seated faults may terminate directly beneath the coverage of the dataset and shallow faults are probably present even if not visible in the data, making it possible for hydrocarbons to migrate from deeper sources and accumulations directly below the pockmark area. The lack of amplitude anomalies suggests that gas is not present in this area, however, Chand et al. (2008) argued that gas hydrates could still be present even without a BSR, as the high amplitudes is caused by the free gas below the hydrates rather than the hydrates itself (Holbrook et al., 2001). The high number of pockmarks could have formed when free gas, previously trapped below the hydrate layer, migrated to the seabed through faults and fractures in the gas hydrates. If the gas hydrates are present in this area, and they are currently decomposing, the gas that is released could potentially indicate that formation of pockmarks is ongoing. Chand et al. (2009) reported a similar situation above the Goliat Field, and could be the case for the pockmarks in the eastern part of the Hammerfest Basin.

5.3.2 Origin of mega depressions on seabed

The mega depressions that were identified on the seabed do not appear to be linked to underlying structures or fluid flow features. They are located at a water depth of 170 – 390 m, and as the eustatic sealevel changes during the LGM ranged from 120 – 135 m (Clark and Mix, 2002), it is likely that they resulted from glacial processes rather than subaerial mechanisms. The mega depressions are far too large to be classified as pockmarks and iceberg scour marks, and appear to be too local to represent MSGLs. The mega depressions at the northern and southern margin of the study area are probably not formed by the same mechanism as they have different shape and appearance.

Seabed morphology has previously been described in the Barents Sea (e.g. Andreassen et al., 2004; Andreassen et al., 2008; Knies et al., 2009) and mega depressions have been reported elsewhere on the continental shelf (e.g. Ottesen et al., 2005; Andreassen et al., 2008). Depressions D1 – D6 (Fig. 4.34) does not appear to be erosive features, as they show no signs of material being shoved or displaced to the surroundings, and there are no coherence with the NW – SE oriented MSGLs. Kettle holes are known to represent circular to sub-circular depressions, similar to those observed in the study area, and are formed when ice blocks or bodies buried beneath glacial till, starts melting (Lagerbäck and Robertsson, 1988; Benn and Evans, 2010), and is the most likely explanation for these depressions. Mega depressions D7 – D10 (Fig. 4.35) does, in contrast to D1 – D6, appear to be formed by erosional processes, hence excluding kettle hole formation. Material has clearly been removed from the seabed through the URU, suggesting highly erosive processes to have occurred, and based on the NW – SE orientation of the mega depressions it is most likely erosion by ice streams. Hill – hole pairs have been described both within the study area and elsewhere on the continental shelf on both the URU and the seabed (e.g. Ottesen et al., 2005; Ostanin et al., 2013), and are glacitectonic landforms consisting of depressions (holes) and corresponding hills that share the characteristics in terms of shape and volume (Sættem, 1990). The hill – hole pairs are most likely formed by flowing ice (Ottesen et al., 2005), where the depressions represent the source of the material that make up the hill (Aber and Ber, 2007). This could explain the presence of the depressions, however, no hills have been observed. The fact that paleo ice streams have flowed NW – SE (Andreassen et al., 2008) in this area, could indicate that the hills have been subject to long distance transport by the grounded ice (Ostanin et al., 2013). This mechanism is the most likely cause for depressions D7 – D10.

6 Summary and conclusion

Interpretation of the 3D seismic data allowed detailed mapping of faults, fluid flow pathways, accumulations and identification of morphologic expressions of URU and seabed pockmarks. The area of this investigation lies in the hydrocarbon-prone Hammerfest Basin above the Base Cretaceous, southwestern part of the Barents Sea. It can be shown that there exist some link between deep structures, fluid flow pathways, shallower fluid accumulations and seabed morphologies indicating the release of fluids.

- Deep-seated faults are divided into three groups, F1, F2 and F3, based on the formation they terminate in. Initiation of these faults most likely occurred during the Kimmerian tectonic phase in the Middle – Late Jurassic when the Atlantic rifting propagated northwards and changed the stress field. The F3 and the E – W and NE – SW oriented F2 faults possibly experienced a small reactivation in the Barremian and Aptian/Albian. Thermal subsidence of the Tromsø Basin resulted in multiple reactivations of the N – S striking F2 faults during the Cretaceous period.
- Tectonic readjustments related to the opening of the Norwegian-Greenland Sea in the Late Cretaceous – Paleocene resulted in reactivation of the F2 faults and initiation the shallow faults. Activity along the F2 and the shallow faults ceased in the Late Eocene.
- Tectonic adjustments along the basin margins is likely to have occurred after the onset of the glaciations in the Plio-Pleistocene.
- Gas chimneys (C1 – C7) are confined to the western margin of the Hammerfest Basin. The high number of faults in this area represents excellent migration pathways for gas from deeper levels. The eastern region of the study area are less faulted, preventing and/or restraining vertical migration of gas. Gas chimneys probably developed after the onset of the Plio-Pleistocene glaciation when uplift and tilting of deeper reservoirs led to spilling of hydrocarbons.
- Seismic amplitude anomalies observed within the Paleocene-Eocene Torsk Formation most likely represent accumulations of free gas below a sealing layer of gas hydrates. Thermogenic gas has potentially migrated along faults and gas chimneys into the Torsk Formation where lateral flow along clinoforms has

allowed gas and liquids to migrate away from the upper termination of the faults. Gas hydrates are probably present in the eastern Hammerfest Basin. Amplitude anomalies at the URU represent free gas accumulations, where the glacigenic sediments act as an impermeable barrier on occasions. Lack of glacigenic sediments prevents fluids to accumulate along the URU in the eastern part of the study area.

- Accumulations of hydrocarbons can be charged from various sources, both Jurassic and pre-Jurassic. Gas in the eastern part of the Hammerfest Basin have most likely migrated laterally from a western source of pre-Jurassic origin.
- Mapping of faults, amplitude anomalies and pockmarks suggests that E – W and NE – SW striking faults are most prone to fluid migration. The N – S striking faults do not appear to be good migration pathways as the seabed and URU pockmarks only occasionally are observed above them. Leakage along shallow faults and clinoforms has allowed fluids to reach the seabed.
- Pockmarks identified on the seabed and the URU indicate at least two major events of fluid flow release. Variations in stability conditions of the GHSZ, caused by the pressure changes on the seabed during glacial-interglacial cycles, may have allowed the thickness of the GHSZ to increase or decrease. One can expect that occasionally the thickness of the seal and the pressure below has reached as critical overpressure values, allowing free gas to burst upwards and create pockmarks. This can be the main mechanism of pockmark formation in the study area.
- The majority of the pockmarks in the eastern part of the Hammerfest Basin were formed when free gas, previously trapped below the gas hydrates, leaked to the seabed. Pockmark formation could be an ongoing process if the hydrate layer is currently decomposing.
- Focused fluid flow is not likely to have caused mega (600m <) seabed depressions within the Hammerfest Basin. Mega depressions in the southern and northern part of the study area may represent kettle holes (D1 – D6) hill-hole pairs (D7 – D10). Kettle holes are formed when ice blocks, buried below till, starts melting. The hole, in hill – hole pairs, represents the source of the materials making up the hill.

7 References

Aber, J. S. & Ber, A. 2007. Glaciotectonism. Amsterdam, Boston, Heidelberg, London: Elsevier.

Abrams, M. A., Apanel, A. M., Timochenko, O. M. & Kosenkova, N. N. 1999. Oil families and their potential sources in the northeastern Timian Pechora Basin, Russia. *American Association of Petroleum Geologists Bulletin,* 83**,** 553-577.

Andreassen, K., Laberg, J. S. & Vorren, T. O. 2008. Seafloor geomorphology of the SW Barents Sea and its glaci-dynamic implications. *Geomorphology,* 97**,** 157-177.

Andreassen, K., Nilssen, E. G. & Odegaard, C. M. 2007a. Analysis of shallow gas and fluid migration within the Plio-Pleistocene sedimentary succession of the SW Barents Sea continental margin using 3D seismic data. *Geo-Marine Letters,* 27**,** 155-171.

Andreassen, K., Nilssen, L. C., Rafaelsen, B. & Kuilman, L. 2004. Three-dimensional seismic data from the Barents Sea margin reveal evidence of past ice streams and their dynamics. *Geology,* 32**,** 729-732.

Andreassen, K., Ødegaard, C. M. & Rafaelsen, B. 2007b. Imprints of former ice streams, imaged and interpreted using industry three-dimensional seismic data from the south-western Barents Sea. *Geological Society, London, Special Publications,* 277**,** 151-169.

Arntsen, B., Wensaas, L., Loseth, H. & Hermanrud, C. 2007. Seismic modeling of gas chimneys. *Geophysics,* 72**,** SM251-SM259.

Arvo, J. 2014. *Relationship between fluid leakage and faulting along the western and northern margin of the Hammerfest Basin.* Master thesis, UIT The Arctic University of Norway.

Aydin, A. & Berryman, J. G. 2010. Analysis of the growth of strike-slip faults using effective medium theory. *Journal of Structural Geology,* 32**,** 1629-1642.

Badley, M. E. 1985. *Practical seismic interpretation*, International Human Resources Development Corporation.

Barnes, P., Lein, R. & Barnes, P. 1988. Icebergs rework shelf sediments to 500 m off Antarctica. *Geology,* 16**,** 1130-1133.

Bellec, V., Wilson, M., Bøe, R., Rise, L., Thorsnes, T., Buhl-Mortensen, L. & Buhl-Mortensen, P. 2008. Bottom currents interpreted from iceberg ploughmarks revealed by multibeam data at Tromsøflaket, Barents Sea. *Marine Geology,* 249**,** 257-270.

Benn, D. I. & Evans, D. J. A. 2010. *Glaciers and Glaciation*, Hodder Education.

Bergh, S. G., Eig, K., Kløvjan, O. S., Henningsen, T., Olesen, O. & Hansen, J. A. 2007. The Lofoten-Vesterålen continental margin: A multiphase Mesozoic-Palaeogene rifted shelf as shown by offshore-onshore brittle fault-fracture analysis. *Norwegian Journal of Geology,* 87**,** 29-58.

Berndt, C. 2005. Focused fluid flow in passive continental margins. *Philos. Trans. R. Soc. A-Math. Phys. Eng. Sci.,* 363**,** 2855-2871.

Berndt, C., Bünz, S. & Mienert, J. 2003. Polygonal fault systems on the mid-Norwegian margin: A long-term source for fluid flow. *Geological Society Special Publication,* 216**,** 283-290.

Bjørlykke, K. 1993. Fluid flow in sedimentary basins. *Sedimentary Geology,* 86**,** 137-158.

Bonham, L. C. 1980. Migration of Hydrocarbons in Compacting Basins. *American Association of Petroleum Geologists Bulletin,* 64**,** 549-567.

Brown, A. R. 2004. *Interpretation of Three-dimensional Seismic Data*, American Association of Petroleum Geologists and the Society of Exploration Geophysicists.

Bulat, J. 2005. Some considerations on the interpretation of seabed images based on commercial 3D seismic in the Faroe-Shetland Channel. *Basin Research,* 17**,** 21-42.

Bünz, S. & Mienert, J. 2004. Acoustic imaging of gas hydrate and free gas at the Storegga Slide. *Journal of Geophysical Research: Solid Earth,* 109.

Cartwright, J., Huuse, M. & Aplin, A. 2007. Seal bypass systems. *American Association of Petroleum Geologists Bulletin,* 91**,** 1141-1166.

Cathles, L. M., Su, Z. & Chen, D. 2010. The physics of gas chimney and pockmark formation, with implications for assessment of seafloor hazards and gas sequestration. *Marine and Petroleum Geology,* 27**,** 82-91.

Cavanagh, A. J., Di Primio, R., Scheck-Wenderoth, M. & Horsfield, B. 2006. Severity and timing of Cenozoic exhumation in the southwestern Barents Sea. *Journal of the Geological Society,* 163**,** 761-774.

Chand, S., Knies, J., Mienert, K., Andreassen, J., Plassen, L. & Fotland, B. 2008. Gas hydrate stability zone modelling in areas of salt tectonics and pockmarks of the Barents Sea suggests an active hydrocarbon venting system. *Marine and Petroleum Geology,* 25**,** 625-636.

Chand, S., Rise, L., Ottesen, D., Dolan, M., Bellec, V. & Boe, R. 2009. Pockmark-like depressions near the Goliat hydrocarbon field, Barents Sea: Morphology and genesis. *Marine and Petroleum Geology,* 26**,** 1035-1042.

Chand, S., Thorsnes, T., Rise, L., Bøe, H., Brunstad, D., Stoddart, R., Lågstad, P. & Svolsbru, T. 2012. Multiple episodes of fluid flow in the SW Barents Sea (Loppa High) evidenced by gas flares, pockmarks and gas hydrate accumulation. *Earth and Planetary Science Letters,* 331-332**,** 305-314.

Chaouch, A. & Mari, J. L. 2006. 3-D land seismic surveys: Definition of geophysical parameters. *Oil Gas Science and Technology,* 61**,** 611-630.

Chopra, S. & Larsen, G. 2000. Acquisition footprint - its detection and removal. *CSEG Recorder,* 25**,** 16-20.

Chopra, S. & Marfurt, K. J. 2005. Seismic attributes - A historical perspective. *Geophysics,* 70**,** 3SO-28SO.

Clark, P. U. & Mix, A. C. 2002. Ice sheets and sea level of the Last Glacial Maximum. *Quaternary Science Reviews,* 21**,** 1-7.

Clennell, M. B., Hovland, M., Booth, J. S., Henry, P. & Winters, W. J. 1999. Formation of natural gas hydrates in marine sediments: 1. Conceptual model of gas hydrate growth conditioned by host sediment properties. *Journal of Geophysical Research: Solid Earth,* 104**,** 22985-23003.

Davis, G. H., Reynolds, S. J. & Kluth, C. F. 2011. *Structural geology of rocks and regions,* New York, Wiley.

DiPietro, J. A. 2013. *Landscape Evolution in the United States: An Introduction to the Geography, Geology, and Natural History,* Burlington, Burlington : Elsevier Science.

Dorè, A. G. 1995. Barents Sea geology, petroleum resources and commercial potential. *Arctic,* 48**,** 207-221.

Dorè, A. G. & Jensen, L. N. 1996. The impact of late Cenozoic uplift and erosion on hydrocarbon exploration: Offshore Norway and some other uplifted basins. *Global and Planetary Change,* 12**,** 415-436.

Dorè, A. G., Scotchman, I. C. & Corcoran, D. 2000. Cenozoic exhumation and prediction of the hydrocarbon system on the NW European margin. *Journal of Geochemical Exploration,* 69-70**,** 615-618.

Duran, E., Di Primio, R., Anka, Z., Stoddart, D. & Horsfield, B. 2013b. 3D-basin modelling of the Hammerfest Basin (southwestern Barents Sea): A quantitative assessment of petroleum generation, migration and leakage. *Marine and Petroleum geology,* 45**,** 281-303.

Duran, E. R., di Primio, R., Anka, Z., Stoddart, D. & Horsfield, B. 2013a. Petroleum system analysis of the Hammerfest Basin (southwestern Barents Sea): Comparison of basin modelling and geochemical data. *Organic Geochemistry,* 63**,** 105-121.

Eichhubl, P., Davatzes, N. C. & Becker, S. P. 2009. Structural and diagenetic control of fluid migration and cementation along the Moab fault, Utah. *American Association of Petroleum Geologists Bulletin,* 93**,** 653-681.

England, W. A., Mackenzie, A. S., Mann, D. M. & Quigley, T. M. 1987. The movement and entrapment of petroleum fluids in the subsurface. *Journal of the Geological Society,* 144**,** 327-347.

Faleide, J. I., Gudlaugsson, S. T. & Jacquart, G. 1984. Evolution of the western Barents Sea. *Marine and Petroleum Geology,* 1**,** 123-IN1.

Faleide, J. I., Solheim, A., Fiedler, A., Hjelstuen, B. O., Andersen, E. S. & Vanneste, K. 1996. Late Cenozoic evolution of the western Barents Sea-Svalbard continental margin. *Global and Planetary Change,* 12**,** 53-74.

Faleide, J. I., Tsikalas, F., Breivik, A. J., Mjelde, R., Ritzmann, O., Engen, O., Wilson, J. & Eldholm, O. 2008. Structure and evolution of the continental margin off Norway and Barents Sea. *Episodes,* 31**,** 82-91.

Faleide, J. I., Vågnes, E. & Gudlaugsson, S. T. 1993. Late Mesozoic-Cenozoic evolution of the south-western Barents Sea in a regional rift-shear tectonic setting. *Marine and Petroleum Geology,* 10**,** 186-214.

Fisher, Q. J., Casey, M., Harris, S. D. & Knipe, R. J. 2003. Fluid-flow properties of faults in sandstone: The importance of temperature history. *Geology,* 31**,** 965-968.

Fossen, H. & Gabrielsen, R. H. 2005. *Strukturgeologi*, Fagbokforlaget Vigmostad & Bjørke AS.

Gabrielsen, R. H. 1984. Long-lived fault zones and their influence on the tectonic development of the southwestern Barents Sea. *Journal of the Geological Society,* 141**,** 651-662.

Gabrielsen, R. H., Faerseth, R. B., Jensen, L. N., Kalheim, J. E. & F., R. 1990. Structural Elements of the Norwegian Continental Shelf. Pt. 1. The Barents Sea Region. 6**,** 1-33.

Gartrell, A., Lisk, M., Dewhurst, D. & Zhang, Y. 2004. Fault intersections as critical hydrocarbon leakage zones: Integrated field study and numerical modelling of an example from the Timor Sea, Australia. *Marine and Petroleum Geology,* 21**,** 1165-1179.

Grauls, D. 2001. Gas hydrates: importance and applications in petroleum exploration. *Marine and Petroleum Geology,* 18**,** 519-523.

Gudlaugsson, S. T., Faleide, J. I., Johansen, S. E. & Breivik, A. J. 1998. Late Palaeozoic structural developments of the south-western Barents Sea. *Marine and Petroleum Geology,* 15**,** 73-102.

Guzzetta, G. & Cinquegrana, R. E. 1987. "Fluid tectonics": a little appreciated facet of buoyancy tectonics. *Tectonophysics,* 139**,** 321-324.

Hansen, D. M., Shimeld, J. W., Williamson, M. A. & Lykke-Andersen, H. 2004. Development of a major polygonal fault system in Upper Cretaceous chalk and Cenozoic mudrocks of the Sable Subbasin, Canadian Atlantic margin. *Marine and Petroleum Geology,* 21**,** 1205-1219.

Harrington, P. K. 1985. Formation of pockmarks by pore-water escape. *Geo-Marine Letters,* 5**,** 193-197.

Heggland, R. 1997. Detection of gas migration from a deep source by the use of exploration 3D seismic data. *Marine Geology,* 137**,** 41-47.

Henriksen, E., Bjørnseth, H. M., Hals, T. K., Heide, T., Kirjukhina, T., Kløvjan, O. S., Larssen, G. B., Ryseth, A. E., Rønning, K., Sollid, K. & Stoupakova, A. V. 2011b. Uplift and erosion of the greater Barents Sea: Impact on prospectivity and petroleum systems. *Geological Society, London, Memoirs,* 35**,** 163-195.

Henriksen, E., Ryseth, A. E., Larssen, G. B., Heide, T., Rønning, K., Sollid, K. & Stoupakova, A. V. 2011a. Tectonostratigraphy of the greater Barents Sea: implications for petroleum systems. *Geological Society, London, Memoirs,* 35**,** 163-195.

Hermanrud, C., Halkjelsvik, M. E., Kristiansen, K., Bernal, A. & Stromback, A. 2014. Petroleum column-height controls in the western Hammerfest Basin, Barents Sea. *Petroleum Geoscience,* 20**,** 227-240.

Hindle, A. D. 1997. Petroleum migration pathways and charge concentration: A three-dimensional model. *American Association of Petroleum Geologists Bulletin,* 81**,** 1451-1481.

Holbrook, W. S., Paull, C. K. & Dillon, W. P. 2001. Seismic studies of the Blake Ridge; implications for hydrate distribution, methane expulsion, and free gas dynamics. *in* Natrual Gas Hydrates, Occurrence, Distribution, and Detection, C. K. Paull and W. P. Dillon. *American Geophysical Union,* 124**,** 235-256.

Hovland, M. 1981. Characteristics of pockmarks in the Norwegian Trench. *Marine Geology,* 39**,** 103-117.

Hovland, M. 1982. A coast-parallel depression, possibly caused by gas migration, off western Norway. *Marine Geology,* 50**,** M11-M20.

Hovland, M., Gardner, J. V. & Judd, A. G. 2002. The significance of pockmarks to understanding fluid flow processes and geohazards. *Geofluids,* 2**,** 127-136.

Hovland, M., Judd, A. G. & Burke Jr, R. A. 1993. The global flux of methane from shallow submarine sediments. 26**,** 559-578.

Hovland, M., Svensen, H., Forsberg, C. F., Johansen, H., Fichler, C., Rueslåtten, H., Jonsson, R. & Fosså, J. H. 2005. Complex pockmarks with carbonate-ridges off mid-Norway: Products of sediment degassing. *Marine Geology,* 218**,** 191-206.

Hustoft, S., Mienert, J., Bünz, S. & Nouzé, H. 2007. High-resolution 3D-seismic data indicate focussed fluid migration pathways above polygonal fault systems of the mid-Norwegian margin. *Marine Geology,* 245**,** 89-106.

Indrevær, K., Bergh, S. G., Koehl, J. B., Hansen, J. A., Schermer, E. R. & Ingebrigtsen, A. 2013. Post-Caledonian brittle fault zones on the hyperextended SW Barents Sea margin: New insights into onshore and offshore margin architecture. *Norwegian Journal of Geology,* 93**,** 167-188.

Jakobsson, M., Mayer, L., Coakley, B., Dowdeswell, J., Forbes, S., Fridman, B., Hodnesdal, H., Noormets, R., Pedersen, R., Rebesco, M., Schenke, H., Zarayskaya, Y., Accettella, D., Armstrong, A., Anderson, R. M., Bienhoff, P., Camerlenghi, A., Church, I., Edwards, M., Gardner, J., Hall, J., Hell, B., Hestvik, O., Kristoffersen, Y., Marcussen, C., Mohammad, R., Mosher, D., Nghiem, S. V., Pedrosa, M., Travaglini, P. G. & Weatherall, P. 2012. The International Bathymetric Chart of the Arctic Ocean (IBCAO) Version 3.0. *Geophysical Research Letters,* 39.

Judd, A. & Hovland, M. 2007. *Seabed Fluid Flow: The Impact on Geology, Biology and the Marine Environment,* Cambridge, Cambridge University Press.

Judd, A. G. & Hovland, M. 1992. The Evidence Of Shallow Gas In Marine-Sediments. *Continental Shelf Research,* 12**,** 1081-1095.

Judd, A. G., Jukes, M., Hovland, L. I., Dimitrov, S., García Gil, V. & Judd, V. 2002. The geological methane budget at continental margins and its influence on climate change. *Geofluids,* 2**,** 109-126.

Kearey, P., Klepeis, K. A. & Vine, F. J. 2009. *Global Tectonics,* Chichester, Wiley-Blackwell.

Knies, J., Matthiessen, J., Vogt, C., Laberg, J. S., Hjelstuen, B. O., Smelror, M., Larsen, E., Andreassen, K., Eidvin, T. & Vorren, T. O. 2009. The Plio-Pleistocene glaciation of the Barents Sea-Svalbard region: a new model based on revised chronostratigraphy. *Quaternary Science Reviews,* 28**,** 812-829.

Knipe, R. J., Jones, G. & Fisher, Q. J. 1998. Faulting, fault sealing and fluid flow in hydrocarbon reservoirs; an introduction. *Geological Society, London, Special Publications,* 147**,** vii-xxi.

Knutsen, S.-M. & Vorren, T. O. 1991. Early Cenozoic sedimentation in the Hammerfest Basin. *Marine Geology,* 101**,** 31-48.

Kristensen, L. F. 2010. *Fluid migration and shallow gas accumulation on the south-western flank of Loppa High, SW Barents Sea.* Master thesis, University of Tromsø.

Laberg, J. S. & Andreassen, K. 1996. Gas hydrate and free gas indications within the Cenozoic succession of the Bjørnøya Basin, western Barents Sea. *Marine and Petroleum Geology,* 13**,** 921-940.

Laberg, J. S., Andreassen, K. & Knutsen, S. M. 1998. Inferred gas hydrate on the Barents Sea shelf - A model for its formation and a volume estimate. *Geo-Marine Letters,* 18**,** 26-33.

Lagerbäck, R. & Robertsson, A. 1988. Kettle holes - stratigraphical archives for Weichselian geology and palaeoenvironment in northernmost Sweden. *Boreas,* 17**,** 439-468.

Larssen, G. B., Elvebakk, G., Henriksen, L. B., Kristensen, S. E., Nilsson, I., Samuelsberg, T. J., Svånå, T. A., Stemmerik, L. & Worsley, D. 2005. Upper Palaeozoic lithostratigraphy of the Southern part of the Norwegian Barents Sea. *Norges Geologiske Undersøkelse Bulletin 444,* 9**,** 3-43.

Leith, T. L., Weiss, H. M., Mørk, A., Århus, N., Elvebakk, G., Embry, A. F., Brooks, P. W., Stewart, T. M., Pchelina, T. M., Bro, E. G., Verba, M. L., Danyushevskaya, A. & Borisov, A. V. 1992. Mesozoic hydrocarbon source-rocks of the Arctic region. *In*: Vorren, T.O., Bergsager, E., Dahl-Stamnes, Ø.A., Holter, E., Johansen, B., Lie, E. & Lund, T.B. (eds) *Arctic Geology and Petroleum Potential. Norwegian Petroleum Society Special Publications, 2, Elsevier, Amsterdam, 1-25*.

Ligtenberg, H. & Connolly, D. 2003. Chimney detection and interpretation, revealing sealing quality of faults, geohazards, charge of and leakage from reservoirs. *Journal of Geochemical Exploration,* 78-79**,** 385-387.

Ligtenberg, J. H. 2005. Detection of fluid migration pathways in seismic data: implications for fault seal analysis. *Basin Research,* 17**,** 141-153.

Linjordet, A. & Grung-Olsen, R. 1992. The Jurassic Snøhvit Gas Field. Hammerfest Basin, Offshore Northern Norway. *In*: Halbouty, M.T (ed.). *Giant Gas and Oil Fields of the Decade 1978-1988: American Association of Petroleum Geologists Memoir, 54, 349-370*.

Long, D. 1992. Devensian late-glacial gas escape in the central North Sea. *Continental Shelf Research,* 12**,** 1097-1110.

Løseth, H., Gading, M. & Wensaas, L. 2009. Hydrocarbon leakage interpreted on seismic data. *Marine and Petroleum Geology,* 26**,** 1304-1319.

Løseth, H., Wensaas, L., Arntsen, B., Hanken, N. M., Basire, C. & Graue, K. 2011. 1000 m long gas blow-out pipes. *Marine and petroleum geology,* 28**,** 1047-1061.

Macdonald, I. R., Bohrmann, G., Escobar, E., Abegg, F., Blanchon, P., Blinova, V., Bruckmann, W., Drews, M., Eisenhauer, A., Han, X., Heeschen, K., Meier, F., Mortera, C., Naehr, T., Orcutt, B., Bernard, B., Brooks, J. & de Farago, M. 2004. Asphalt volcanism and chemosynthetic life in the Campeche Knolls, Gulf of Mexico. *Science,* 304**,** 999-1002.

Martens, I. 2009. *Fluidmigrasjon i Snøhvitområdet - drivmekanismer og strømningsprosesser.* Master thesis, Universitetet i Tromsø.

Meldahl, P., Heggland, R., Bril, B. & De Groot, P. 2001. Identifying faults and gas chimneys using multiattributes and neural networks. *Leading Edge (Tulsa, OK),* 20**,** 474-482.

Mienert, J., Andreassen, K., Posewang, J. & Lukas, D. 2000. Changes of the Hydrate Stability Zone of the Norwegian Margin from Glacial to Interglacial Times. *Annals of the New York Academy of Sciences,* 912**,** 200-210.

Mienert, J., Vanneste, M., Bünz, S., Andreassen, K., Haflidason, H. & Sejrup, H. P. 2005. Ocean warming and gas hydrate stability on the mid-Norwegian margin at the Storegga Slide. *Marine and Petroleum Geology,* 22**,** 233-244.

NPD. 2015. *Norwegian Petroleum Directorate Factpages* [Online]. Available: http://factpages.npd.no/factpages/Default.aspx?culture=en [Accessed April 2015.

Ohm, S. E., Karlsen, D. A. & Austin, T. J. F. 2008. Geochemically driven exploration models in uplifted areas: Example from the Norwegian Barents Sea. *American Association of Petroleum Geologists Bulletin,* 92**,** 1191-1223.

Osborne, M. J. & Swarbrick, R. E. 1997. Mechanisms for generating overpressure in sedimentary basins: A reevaluation. *American Association of Petroleum Geologists Bulletin,* 81**,** 1023-1041.

Ostanin, I., Anka, Z., di Primio, R. & Bernal, A. 2012. Identification of a large Upper Cretaceous polygonal fault network in the Hammerfest basin: Implications on the reactivation of regional faulting and gas leakage dynamics, SW Barents Sea. *Marine Geology,* 332-334**,** 109-125.

Ostanin, I., Anka, Z., Di Primio, R. & Bernal, A. 2013. Hydrocarbon plumbing systems above the Snohvit gas field: Structural control and implications for thermogenic methane leakage in the Hammerfest Basin, SW Barents Sea.(Report). *Marine and Petroleum Geology,* 43**,** 127.

Ottesen, D., Rise, D. & Dowdeswell, D. 2005. Submarine landforms and the reconstruction of fast-flowing ice streams within a large Quaternary ice sheet: The 2500-km-long Norwegian-Svalbard margin (57°-80°N). *Bulletin of the Geological Society of America,* 117**,** 1033-1050.

Paull, C. K., Ussler, W., III, Borowski, W. S., Gardner, J. M. & Vogt, P. R. 1999. Freshwater ice rafting; an additional mechanism for the formation of some high-latitude submarine pockmarks. *Geo-Marine Letters,* 19**,** 164-168.

Plaza-Faverola, A., Pecher, I., Crutchley, G., Barnes, P., Bunz, S., Golding, T., Klaeschen, D., Papenberg, C. & Bialas, J. 2014. Submarine gas seepage in a mixed contractional and shear deformation regime: Cases from the Hikurangi oblique-subduction margin. *Geochemistry Geophysics Geosystems,* 15**,** 416-433.

Rajan, A., Bunz, S., Mienert, J. & Smith, A. J. 2013. Gas hydrate systems in petroleum provinces of the SW-Barents Sea. *Marine and Petroleum Geology,* 46**,** 92.

Reemst, P., Cloetingh, S. & Fanavoll, S. 1994. Tectonostratigraphic modelling of Cenozoic uplift and erosion in the south-western Barents Sea. *Marine and Petroleum Geology,* 11**,** 478-490.

Roberts, S. J. & Nunn, J. A. 1995. Episodic fluid expulsion from geopressured sediments. *Marine and Petroleum Geology,* 12**,** 195-IN3.

Rønnevik, H., Beskow, B. & Jacobsen, H. P. 1982. Structural and stratigraphic evolution of the Barents Sea. *Canadian Society of Petroleum Geologists Memoir,* 8**,** 431-440.

Schlumberger 2010. *Interpreter´s Guide to Seismic Attributes*, Schlumberger, Huston.

Selley, R. C. 1997. *Elements of Petroleum Geology*, Elsevier Science.

Sheriff, R. E. 1985. Aspects of Seismic Resolution. *Seismic Stratigraphy II: American Association of Petroleum Geologists, Memoir,* 39**,** 1-10.

Sheriff, R. E. 2006. Encyclopedic dictionary of exploration geophysics, 4th edition. *Society of Exploration Geophysicists, Tulsa*.

Shipley, T. H., Houston, M. H., Buffler, R. T., Shaub, F. J., McMillen, K. J., Ladd, J. W. & Worzel, J. L. 1979. Seismic evidence for widespread possible gas hydrate horizons on continental slopes and rises. *American Association of Petroleum Geologists Bulletin,* 63**,** 2204-2213.

Sloan, E. 1998. Gas hydrates: Review of physical/chemical properties. *Energy Fuels,* 12**,** 191-196.

Smelror, M., Petrov, O., Larssen, G. B. & Werner, S. 2009. *Geological History of the Barents Sea,* Trondheim, Geological Survey of Norway.

Smith, A. J., Mienert, J., Bunz, S. & Greinert, J. 2014. Thermogenic methane injection via bubble transport into the upper Arctic Ocean from the hydrate-charged Vestnesa Ridge, Svalbard. *Geochemistry Geophysics Geosystems,* 15**,** 1945-1959.

Solheim, A. & Elverhøi, A. 1985. A pockmark field in the Central Barents Sea; gas from a petrogenic source? *Polar Research,* 3**,** 11-19.

Solheim, A. & Elverhøi, A. 1993. Gas-related sea floor craters in the Barents Sea. *Geo-Marine Letters,* 13**,** 235-243.

Solheim, A. & Kristoffersen, Y. 1984. *Sediments above the upper regional unconformity : thickness, seismic stratigraphy and outline of the glacial history,* Oslo.

Storvoll, V., Bjørlykke, K. & Mondol, N. H. 2005. Velocity-depth trends in Mesozoic and Cenozoic sediments from the Norwegian Shelf. *American Association of Petroleum Geologists Bulletin,* 89**,** 359-381.

Swarbrick, R. E., Osborne, M. J. & Yardley, G. S. 2002. Comparison of Overpressure Magnitude Resulting from the Main Generating Mechanisms, *In:* A. R. Huffman and G. L. Bowers, (eds.). *Pressure regimes in sedimentary basins and their prediction: American Association of Petroleum Geologists Memoir,* 76**,** 1-12.

Sættem, J. 1990. Glaciotectonic forms and structures on the Norwegian continental shelf: observations, processes and implications. *Norsk Geologisk Tidsskrift,* 70**,** 81-94.

Thrasher, J., Fleet, A. J., Hay, S. J., Hovland, M. & Düppenbecker, S. 1996. Understanding geology as the key to using seepage in exploration: the spectrum of seepage styles. In D. Schumacher and M. A Abrams, (eds.). *Hydrocarbon migration and its near-surface expression: American Association of Petroleum Geologists Memoir,* 66**,** 223-241.

Twiss, R. J. & Moores, E. M. 2007. *Structural Geology,* New York, W.H. Freeman Co.

Vadakkepuliyambatta, S., Bunz, S., Mienert, J. & Chand, S. 2013. Distribution of subsurface fluid-flow systems in the SW Barents Sea.(Report). *Marine and Petroleum Geology,* 43**,** 208-221.

Veeken, P. C. H. 2007. *Seismic Stratigraphy, Basin Analysis and Reservoir Characterisation. Handbook of Geophysical Exploration*, Elsevier Science.

Veeken, P. C. H. & Moerkerken, B. v. 2013. *Seismic Stratigraphy and Depositional Facies Models,* Houten, EAGE.

Vorren, T. O., Richardsen, G., Knutsen, S. M. & Henriksen, E. 1991. Cenozoic erosion and sedimentation in the western Barents Sea. *Marine and Petroleum Geology,* 8**,** 317-340.

Whiticar, M. J. 2002. Diagenetic relationships of methanogenesis, nutrients, acoustic turbidity, pockmarks and freshwater seepages in Eckernförde Bay. *Marine Geology,* 182**,** 29-53.

Whiticar, M. J. & Werner, F. 1981. Pockmarks: Submarine vents of natural gas or freshwater seeps? *Geo-Marine Letters,* 1**,** 193-199.

Winsborrow, M. C. M., Andreassen, K., Corner, G. D. & Laberg, J. S. 2010. Deglaciation of a marine-based ice sheet: Late Weichselian palaeo-ice dynamics and retreat in the southern Barents Sea reconstructed from onshore and offshore glacial geomorphology. *Quaternary Science Reviews,* 29**,** 424-442.

Wiprut, D. & Zoback, M. D. 2000. Fault reactivation and fluid flow along a previously dormant normal fault in the Northern North Sea. *Geology,* 28**,** 595-598.

Woodworth-Lynas, C. M. T., Josenhans, H. W., Lewis, J. V., Parrott, C. F. M. & Barrie, D. R. 1991. The physical processes of seabed disturbance during iceberg grounding and scouring. *Continental Shelf Research,* 11**,** 939-961.

Woodworth-Lynas, C. M. T., Simms, A. & Rendell, C. M. 1985. Iceberg grounding and scouring on the Labrador Continental Shelf. *Cold Regions Science and Technology,* 10**,** 163-186.

Worsley, D. 2008. The post-Caledonian development of Svalbard and the western Barents Sea. *Polar Research,* 27**,** 298-317.

Worsley, D., Johansen, R. & Kristensen, S. 1988. The Mesozoic and Cenozoic succession of Tromsøflaket *In*: Dalland, A., Worsley, D. and Ofstad, K. (Eds.). *A lithostratigraphic scheme for the Mesozoic and Cenozoic succession offshore mid-and northern Norway. Norwegian Petroleum Directorate Bulletin,* 4**,** 42-65.

-